RESEARCH AND DEVELOPMENT OF LIQUID BASED STRETCHABLE SENSORS WITH WIRELESS CAPABILITY

LOW JEN HAHN

DOCTOR OF PHILOSOPHY (ENGINEERING)

LEE KONG CHIAN FACULTY OF ENGINEERING AND SCIENCE
UNIVERSITI TUNKU ABDUL RAHMAN
NOVEMBER 2021

RESEARCH AND DEVELOPMENT OF LIQUID BASED STRETCHABLE SENSORS WITH WIRELESS CAPABILITY

By

LOW JEN HAHN

A thesis submitted to the Department of Electrical and Electronic Engineering,
Lee Kong Chian Faculty of Engineering and Science,
Universiti Tunku Abdul Rahman,
in partial fulfillment of the requirements for the degree of
Doctor of Philosophy (Engineering)
November 2021

ABSTRACT

Research and Development of Liquid Based Stretchable Sensors with Wireless Capability

LOW JEN HAHN

Sensors are important devices to detect physical parameters and convert them into electrical signals for computers to analyze. However, most of the conventional sensors are non-flexible and do not have wireless capability. The non-flexible of conventional sensors makes it difficult to be attached on non-planar surfaces. Also, an additional antenna is required to transmit the sensor's data wirelessly, which increases the overall design footprint. To solve the aforementioned constraints, this thesis has proposed the use of elastomers and liquids for the construction of the soft sensors with wireless capabilities. The sequence of developing the soft sensors with wireless capabilities is presented in 4 parts.

In the first part, a stretchable microfluidic sensor is proposed for placing on non-planar surfaces such as human skin. The deformation (stretching and compressing) of the stretchable sensor can cause its resistance to change. The use of highly stretchable elastomer and liquid in the sensor gives good mechanical durability under 100 continuous cycles, and low hysteresis of 5.01% and 4.24% for normal pressure and axial strain mechanical loading, respectively. Due to its high stretchability and good compliance to human skin, it was placed on the shoe insole to detect foot pressure during walking and running.

Experimental data shows that this resistive sensor can detect the pressure from human foot by capturing accurately the weightages of the stance and swing phases for a complete gait cycle. Since the sensor does not have wireless capability, an external antenna (Bluetooth) had to be connected to transfer data wirelessly.

To integrate wireless functionality into the sensor, in the second and third parts, new types of sensor designs were proposed by modifying the patch antenna and dielectric resonator antenna (DRA), respectively. They were designed by using elastomer and liquid for improving their stretchability. Also, an air cavity is incorporated into the design for air pressure sensing. Numerical simulations were first performed to optimize the antenna designs, then followed by experiments to validate the simulation results. The results are in good agreement with each other. Then, air pressure tests were conducted for these antennas in high and low ambient pressure conditions to study their sensing performance, and the shift in resonant frequencies was observed. It has been observed that the resonant frequency changes linearly with the air pressure. The liquid patch antenna and liquid dielectric resonator antenna (LDRA) show a sensitivity of 176 MHz/bar and 270 MHz/bar, respectively. This proves that the proposed multi-functional antennas can work well as both microwave radiator and air pressure sensor. Here, the design concepts and working principles of the proposed wireless sensors have been successfully proven, and the next step is to implement them as wearable sensors with some useful wireless functionality.

One of the most challenging issues of designing such wearable devices is that the radiated electromagnetic (EM) waves from the antenna may be harmful to human body. To alleviate this problem, a periodic-patterned ground

plane, called electromagnetic bandgap (EBG), is studied for isolating the effects of a wearable antenna. Here, the fourth part, liquid metal is infused into the elastomer platform for designing the proposed liquid EBG (LEBG). A new design, which is the slot antenna, is proposed to be integrated with the LEBG. Experiments show that, after adding the LEBG beneath the slot antenna, the antenna can produce a stable impedance bandwidth when being placed on human body. Higher radiation gain (5.80 dBi) is also seen in the boresight direction, and better specific absorption rate (SAR) performance is achieved with a reduction of about 80% after adding the LEBG. As both the LEBG and antenna are stretchable, they can be stretched up to 30% strain, and the resonant frequency shows linear shifting (3.71 MHz/strain(%)). Finally, a wearable sensor with wireless capability has been successfully demonstrated in the final part of this thesis. The aim of the thesis is achieved where the development of multiple multifunctional antennas that can function as both the radiating element and the sensor are realized. This is different from the commercial electronic components which have only a single function. It can reduce the total footprint of the design. For future works, the antennas can be incorporated with Radio-frequency Identification (RFID) so that the resonant frequencies can be obtained using a mobile RFID reader. Furthermore, the thickness of the sensors can be reduced by using new fabrication techniques.

ACKNOWLEDGEMENTS

I would like to thank everyone who had contributed to the successful completion of this project. I would like to express my gratitude to my research supervisors, Dr Chee Pei Song and Prof Lim Eng Hock for their invaluable advice, guidance, and their enormous patience throughout the development of the research.

In addition, I would also like to express my gratitude to my loving parents and friends who had helped and given me encouragement to complete my thesis when I was facing many obstacles. Additionally, I would like to specially thank Dr Ng Wai Hau and Dr Lee Shin Rou, former postgraduate students of Prof Lim Eng Hock, for guiding me in the experiments, which helped in this project.

APPROVAL SHEET

This thesis entitled "**RESEARCH AND DEVELOPMENT OF LIQUID BASED STRETCHABLE SENSORS WITH WIRELESS CAPABILITY**" was prepared by LOW JEN HAHN and submitted as partial fulfilment of the requirements for the degree of Doctor of Philosophy (Engineering) at Universiti Tunku Abdul Rahman.

Approved by:

_____

(Dr. CHEE PEI SONG)
Date: 3 November 2021
Professor/Supervisor
Department of Mechatronics & Biomedical Engineering
Lee Kong Chian Faculty of Engineering & Science
Universiti Tunku Abdul Rahman

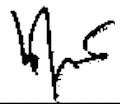

_____

(Prof. Dr. LIM ENG HOCK)
Date: 3 November 2021
Professor/Co-supervisor
Department of Electrical & Electronic Engineering
Lee Kong Chian Faculty of Engineering & Science
Universiti Tunku Abdul Rahman

LEE KONG CHIAN FACULTY OF ENGINEERING AND SCIENCE
UNIVERSITI TUNKU ABDUL RAHMAN

Date: 3 November 2021

SUBMISSION OF THESIS

It is hereby certified that **LOW JEN HAHN** (ID No: **18UED06088**) has completed this thesis entitled "**RESEARCH AND DEVELOPMENT OF LIQUID BASED STRETCHABLE SENSORS WITH WIRELESS CAPABILITY**" under the supervision of Dr. Chee Pei Song (Supervisor) from the Department of Mechatronics & Biomedical Engineering, Lee Kong Chian Faculty of Engineering and Science (FES), and Prof. Dr. Lim Eng Hock (Co-Supervisor) from the Department of Electrical and Electronic Engineering, Lee Kong Chian Faculty of Engineering and Science (FES).

I understand that University will upload softcopy of my thesis in pdf format into UTAR Institutional Repository, which may be made accessible to UTAR community and public.

Yours truly,

(LOW JEN HAHN)

DECLARATION

I hereby declare that the thesis is based on my original work except for quotations and citations which have been duly acknowledged. I also declare that it has not been previously or concurrently submitted for any other degree at UTAR or other institutions.

Name _LOW JEN HAHN_____

Date _3 NOVEMBER 2021_____

TABLE OF CONTENTS

LIST OF TABLES

LIST OF FIGURES

LIST OF ABBREVIATIONS

L	Length
f	Frequency
P	Pressure
h	Height/altitude
R	Resistance
A	Cross-sectional area
E_{PDMS}	Young's modulus of PDMS
$E_{Ecoflex}$	Young's modulus of Ecoflex
E_{skin}	Young's modulus of Human Skin
T_g	Glass-transition temperature
E_z	Electric field in *z*-component
ε_o	Dielectric constant of vacuum
ε_r	Relative permittivity of dielectric media
ρ	Electrical resistivity
υ	Poisson's ratio
λ	Wavelength
IoT	Internet of things
PDMS	Polydimethylsiloxane
EGaIn	Eutectic Gallium Indium
DRA	Dielectric resonator antenna
LDRA	Liquid dielectric resonator antenna
EM	Electromagnetic
EBG	Electromagnetic bandgap
LEBG	Liquid electromagnetic bandgap
UC-EBG	Uniplanar electromagnetic bandgap
SAR	Specific Absorption Rate
UHF	Ultra-High Frequency
PI	Polyimide
TPU	Thermoplastic polyurethane

PU	Polyurethane
CNT	Carbon nanotubes
Ag	Silver
Cu	Copper
RF	Radio-frequency
FBG	Fiber Bragg grating
AgNW	Silver nanowire
SWCNT	Single-walled carbon nanotube
MIC	Microwave integrated circuits
MMIC	Monolithic microwave circuits
$BaTi_4O_9$	Barium tetratitanate
$(Zr\text{-}Sn)TiO_4$	Zirconium tin titanate
PVC	Polyvinyl chloride
PEC	Perfect electrical conductor
PMC	Perfect magnetic conductor
ABS	Acrylonitrile butadiene styrene
LED	Light-emitting diode
ADC	Analog-to-digital converter
ISM	Industrial, Scientific and Medical
VNA	Vector Network Analyzer
SMA	SubMiniature A
L	Inductor
C	Capacitor
5G	Fifth generation technology
FR-4	Flame retardant 4

CHAPTER 1

INTRODUCTION

1.1 Background

The development of stretchable sensors has been gaining interest due to their ability to attach to complex and soft surfaces for achieving high mechanical compliance with human skin. The stretchable sensors could be conformally placed onto the body for measuring strain such as bending motions of limbs. To transmit the sensor data wirelessly, antennas are usually used as the wireless technology (Yan et al., 2018). These antennas are normally constructed with flexible materials such as thin copper sheets or conductive textiles to conform with the stretchable sensors to a non-planar human skin surface (Samal et al., 2013, Xiaomu et al., 2017, Sallam et al., 2017). However, these flexible materials do not have the same elasticity as the human skin which could cause discomfort to the user and prone to plastic deformation.

Studies have shown that the mechanical compliance of an antenna with the human skin can be improved by making it stretchable with the application of the elastomer (Ecoflex) as the substrate with meandering copper structures (Arriola et al., 2011, Zhu et al., 2021, Kim et al., 2019). This is because elastomers such as polydimethylsiloxane (PDMS) (E_{PDMS} = 0.750 MPa) and Ecoflex ($E_{Ecoflex}$ = 0.125 MPa) have Young's modulus which is close to the

human skin (E_{skin} = 0.42-0.85 MPa) (Pailler-Mattei et al., 2008, Agache et al., 1980, Fuard et al., 2008, Amjadi et al., 2015). However, the stretchability is limited by the copper. Then, replacing the solid metal parts in the conventional antenna with liquid metal (Eutectic Gallium Indium) further improves the mechanical deformation, while maintaining its excellent conductivity (Kubo et al., 2010, Huang et al., 2014). This is because the liquid metal has negligible stiffness, and the overall elasticity of the antenna is now governed only by the mechanical properties of the elastomer. Moreover, it is worth noting that the performance of such stretchable antenna with liquid metal is comparable with that of the conventional dipole antenna that uses solid metallic elements (So et al., 2009).

An interesting feature was discovered when a stretchable antenna is deformed (stretched, bent, flexed, or rolled), it can introduce fluctuation in the resonant frequency. The liquid metal in the stretchable antenna flows in response to the elongation of the elastomer and changes the electrical properties of the antenna (Wang et al., 2015, Cheng and Wu, 2010). This feature in the stretchable antenna makes it act as a strain sensor, where a change in strain induces a change in resonant frequency (So et al., 2009, Cheng and Wu, 2011). Therefore, there is a potential in using stretchable antennas to monitor human motion and transmit data wirelessly at the same time. However, the stretchable antenna is not suitable to be directly used on human body because the human body absorbs the antenna's radiated power which detunes the antenna characteristics.

To overcome this, the electromagnetic bandgap (EBG) structure, which consists of periodically repeating patterns, can be placed underneath a wearable antenna to alleviate the antenna-human interaction. At a certain frequency band, the EBG surface can be designed to limit the propagation of surface waves and decreases the unwanted radiation towards the human body (Ashyap et al., 2018, Ashyap et al., 2017). Fabrics were used as conducting and non-conducting materials for fabricating EBG (Ashyap et al., 2017, Gao et al., 2018). However, fabrics are not stretchable. It also absorbs moisture and alters the electrical properties of the EBG. To overcome this problem, the use of elastomer and conductive liquid may be a promising solution for designing a stretchable EBG so that it can be integrated with the stretchable antenna for wearable purposes.

1.2 Problem Statements

Conventional sensors and antennas are made of rigid components which are non-flexible. These rigid components possess a risk of being damaged when accidentally stretched beyond their strain limits. Also, the sensors are hindered by the usage of a wired interface, the need for a power supply, and the requirement of an external antenna to transmit data in a long range. Conventional antennas are also required to be connected to external sensors in order to perform wireless data transmission. One method to solve this is to integrate both functions into a single multifunctional device. Although stretchable antennas have been shown to be able to perform as a wireless strain sensor to solve the aforementioned issues, however, current research is only limited to additional strain sensing capability. Other types of physical sensing, such as pressure sensing, may be required for other applications.

Stretchable antennas can mount on stretchable surfaces, such as human body, due to good mechanical compliance. This makes such a device a good candidate for wearable devices. However, without proper isolation from the human body, the antenna may emit harmful radiation into the human body. To mitigate this problem, a large ground plane was initially proposed to reduce the backward radiation, but its large footprint could make the design uncomfortable to the user (Ashyap et al., 2020). It would also form an image current that is out-of-phase with the antenna, causing the radiation performance to deteriorate. Thus, the EBG, which has an in-phase reflection, can be placed underneath the antenna to effectively isolate the human body from the antenna and improve the radiation performance. However, most of the reported EBGs are not stretchable and they are not mechanically compliant with the human skin. Hence, there is a need to address these challenges to improve the wearable performance and expand the functionalities of stretchable antennas.

1.3 Aim and Objectives

This thesis aims to utilize the combination of elastomer and liquid to develop soft sensors with wireless capabilities that can be used on the human body. The aim can be achieved through these objectives:

(1) To develop soft and stretchable sensors using microfluidic approach.

(2) To integrate the soft sensors with wireless sensing capability using antenna technology.

(3) To apply the developed sensor-antenna on the human body using the liquid electromagnetic bandgap.

1.4 Contribution of the Study

This section describes the contributions of my research works. Theoretical analysis and experimental investigations of the soft sensors from without wireless capability to the sensors with wireless capability are presented in this thesis. The major outcomes of this thesis can be summarized as follows:

(1) A soft and stretchable sensor was fabricated using microfluidic approach for applying on human body. The sensor was made of elastomer and liquid metal which can conform well on human foot and ankle for gait monitoring. Due to the good mechanical compliance to human body, the sensor was able to extract the stance and swing phases accurately for both walking and running gaits. The sensor is able to detect the pressure exerted from the human foot.

(2) To add wireless functionality to a sensor, a liquid patch antenna was modified into an air pressure sensor by using stretchable materials and incorporated an air cavity into the antenna structure. The antenna was able to respond to different ambient pressures by expanding or contracting its shape. The altering of the antenna's shape causes the resonant frequency to fluctuate. The change in its resonant frequency when subjected to different ambient pressure makes this antenna works as a wireless air pressure sensor.

(3) Liquid dielectric resonator antennas (LDRAs) were commonly used to overcome the disadvantages of solid dielectrics. However, it is difficult to

obtain a liquid dielectric that has both high dielectric constant and low loss tangent. To the best of the author's knowledge, no report was found on the usage of acetonitrile as the liquid dielectric of a dielectric resonator antenna. The high dielectric constant and low loss tangent of the acetonitrile allow the proposed liquid dielectric resonator antenna to be smaller and more efficient. Air cavity has also been tactfully included to make the proposed antenna work well as both the antenna and air pressure sensor.

(4) The EBG has been widely used for designing various wearable antennas for isolating the effect of human body. However, there has been no reported EBG that is stretchable and high mechanical compliant with human skin. Here, a fully stretchable liquid EBG (LEBG) is proposed for integrating with a slot antenna to form a wearable device. Tensile test has also been done to verify its functionality as a strain sensor, where the resonant frequency shifts when subjected to strain.

1.5 Thesis Outline

In this thesis, 7 chapters are reported. Chapter 1 introduces the background of the wearable devices and the materials required to improve the stretchability of wearable antennas. The need for stretchable electromagnetic bandgap for wearable antenna is also reviewed.

A review of the stretchable sensor development associated with the present study is given in Chapter 2, including the basic components of the microfluidic sensor, the air cavity, and the liquid dielectric.

Then, in Chapter 3, the stretchable sensor is designed, fabricated, and characterized. Characterization such as mechanical responses (stretching and pressing) and performance under prolonged cycles are shown in this section.

In Chapter 4, a multifunctional patch antenna is developed by integrating the antenna design with an air cavity. This is to demonstrate that the addition of the air cavity increases the sensitivity of the antenna towards different ambient pressure conditions. The description of the design, working principle, and fabrication procedure will be presented in detail. Analysis of the antenna will be discussed with simulated and measured results.

In Chapter 5, a dual-functional liquid dielectric resonator antenna (LDRA) that has a high dielectric constant and low loss tangent is proposed for sensing air pressure. Organic acetonitrile is proposed for designing a compact LDRA that can work efficiently in the Ultra-High Frequency (UHF) band. The design configuration, selection of dielectrics, working principle, and fabrication procedures will be presented in detail. The LDRA will be discussed with simulated and measured results. The inclusion of air cavity in the LDRA is also shown to improve the sensitivity of the antenna towards changes in ambient pressure.

In Chapter 6, a liquid electromagnetic bandgap (LEBG) which is designed using a soft elastomer and liquid metal is proposed for integrating with a liquid slot antenna. The LEBG can mitigate the effect of human body on the antenna's performance. Description of the design, working principle, and fabrication procedures of the wearable antenna will be presented in detail. Analysis of the bending and stretching of the wearable antenna will be discussed with measured results. The wearable performance of the antenna will also be studied.

In Chapter 7, the research works are summarized and followed by a few proposed future works that can improve the wearable antenna's performances.

CHAPTER 2

LITERATURE REVIEW

2.1 Introduction of Stretchable Electronics

In the future, a wide variety of electronic devices might become wearable and would be applied near our skin. These devices should preferably be stretchable to withstand different deformations caused by human motions, such as bending and elongation. Such stretchable electronics can be benefited from the rapid development of personalized healthcare monitoring, human motion detection, multifunctional electronic skin, and human-machine interfaces. To create stretchable electronics, both the insulators and conductors must be stretchable.

2.2 Types of Stretchable Insulators

Insulators are commonly used as dielectrics, substrates, or encapsulation materials in electronics. Traditional insulators like FR-4 (Flame Retardant 4) have no flexibility and stretchability and are not suitable for the next-generation wearable applications, which demand high mechanical compliance. Hence, several common stretchable insulators that are used in stretchable electronic devices are briefly introduced here.

2.2.1 Polyimide

Polyimides (PIs) are high-quality polymers that exist both as thermosets and thermoplastics, which are known by the repeating imide structure as a linear or heterocyclic unit in the main chain of the polymer backbone, as shown in Figure 2.1.

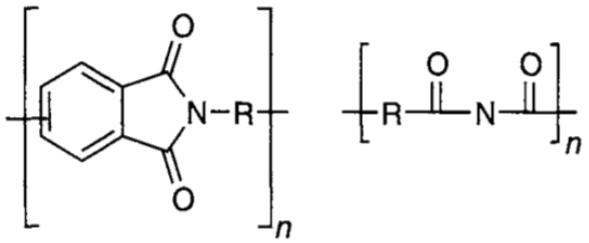

Figure 2.1: General chemical structure of polyimide (Fahim et al., 2001).

Polyimides can be translucent or opaque depending on the monomers, chemical structure, and the method of polymerization (Preston and Black, 1967, St Clair et al., 1987). They possess excellent tribological, thermal, and electrical properties. They also exhibit high flexural modulus and good impact strength below their glass-transition temperature (T_g). Although it can be bent and stretched, it is not widely used for stretchable electronics due to its high Young's modulus (~3 GPa), low tensile elongation (20-100%) (Wallach, 1968), and flexural modulus (Sun et al., 2009).

2.2.2 Polyurethane

Polyurethanes (PUs) are a diverse family of polymers with just one aspect in common – the presence of the urethane group (−NHCO−O−). Polyurethane-based materials have been used in different forms, such as

thermoplastic polyurethane (TPU), polyurethane sponge, and PU yarn (Wang et al., 2016b, Fan et al., 2012, Huang et al., 2017, Wang et al., 2011).

Polyurethanes have highly flexible chains and crosslinks. The crosslinks may be chemically or physically. Cross-linking is able to achieve physically by hard domain function and hydrogen bonding. For chemical crosslinking, it is introduced through multi- or trifunctional constituents. Physically crosslinks are block copolymers, which consist of alternating flexible and rigid blocks. Due to the two blocks having distinct polarities and chemical natures, they can be classified into two phases: "soft" and "hard", as shown in Figure 2.2. It can elongate more if the soft segment concentration is larger (Petrović and Budinski-Simendić, 1985). Wearable electronics that are fabricated by polyurethanes have an improved stretchability, which is highly desirable in pressure or strain sensors (Zhu et al., 2019, Huang et al., 2018).

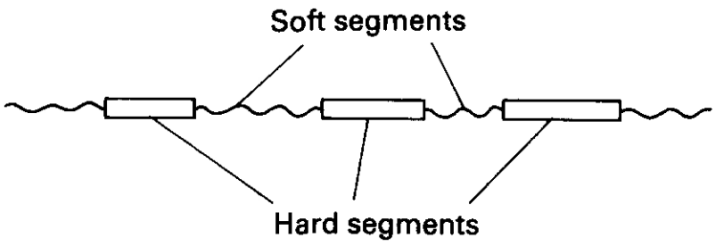

Figure 2.2: Schematic representation of the structure of the segmented polyurethanes.

2.2.3 Polydimethylsiloxane (PDMS)

PDMS has a chemical formula of $CH_3[Si(CH_3)_2O]_nSi(CH_3)_3$, where *n* is the number of repeated backbone units. Due to the siloxane linkages, its backbone $[SiO(CH_3)_2]$ is quite flexible, which might be similar to the ether

linkages used in polyurethanes (Kuo, 1999). The flexibility (bendable and stretchable) of PDMS offers a unique advantage over the traditional rigid substrates (glass, silicon) and makes it suitable for soft electronics. It can also be used as a good electrical insulation for fabricating soft electronic devices. The elastic modulus ranges from 1.32-2.97 MPa, depending on the ratio between the monomer and the curing agent as well as the curing temperature. The two methods that can be employed for fabricating the PDMS elastomer are - condensation and addition reactions. Addition reaction is usually performed in the laboratory environment due to its convenient processing, and it does not require costly instruments, as shown in Figure 2.3. Furthermore, PDMS is transparent, inert, non-toxic, and non-flammable.

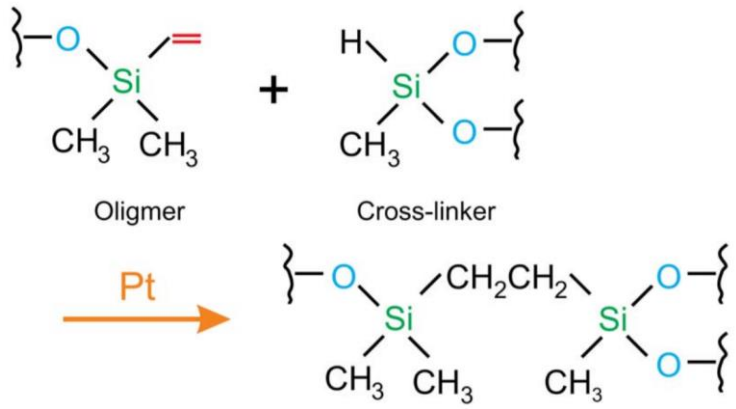

Figure 2.3: Polymerization scheme of the two-component PDMS (Wu et al., 2015).

2.2.4 Ecoflex

Ecoflex elastomers are platinum-catalysed silicones (Smooth-On, 2021) that have a very low Young's modulus ($E_{ecoflex}$ = 125 kPa), which is quite close to human skin (E_{skin} = 420-850 kPa) (Lu et al., 2012, Park et al., 2010). Its good biocompatibility makes it easy to be used as a skin-mountable device without

any skin irritation, restriction, or discomfort. The Ecoflex is suitable for long-term sensing applications due to its environmentally stable polymer characteristics (water-resistant) that is, as opposed to the aging effect that exists in the PDMS. Also, the Ecoflex can be added with carbon nanotubes (CNT) to form high-performance strain sensors due to the strong interfacial bonding between the Ecoflex and the CNTs matrix. This also leads to lower hysteresis in the CNT-Ecoflex nanocomposite-based strain sensors.

2.3 Types of Stretchable Conductors

Materials that allow electrical currents to flow in one or more directions are known as conductors. Stretchable conductors are necessary to be included within the elastomeric substrates to construct a stretchable circuit, without obstructing its excellent mechanical flexibility. The techniques for producing stretchable conductors are shown in Figure 2.4.

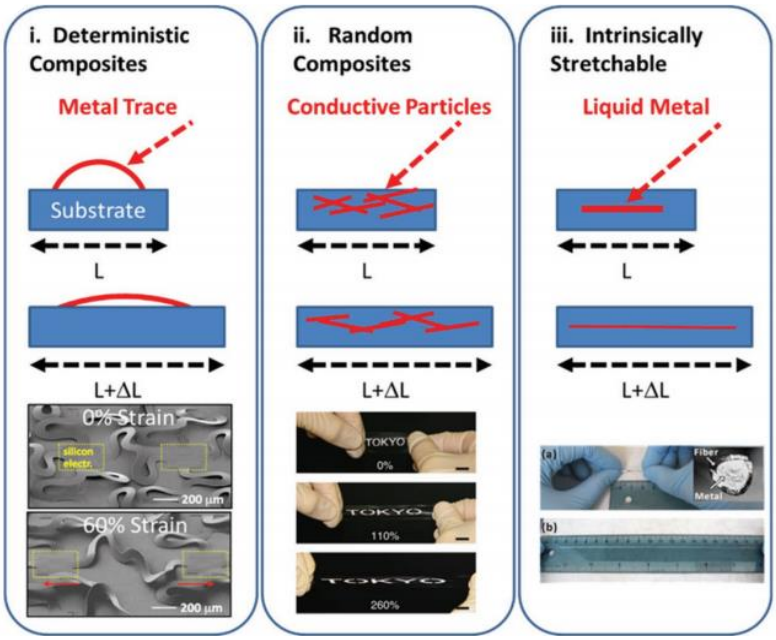

Figure 2.4: Strategies for stretchable and soft conductors (Dickey, 2017).

2.3.1 Thin Film Metal

Stretchable thin films can be realized by depositing a thin layer of solid metal (aluminium, gold, and nickel) on the PDMS substrate to form wavy structures, either through non-linear buckling or wrinkling (Wang et al., 2016a, Bowden et al., 1998, Lin and Yang, 2007). Gold is usually used as it is one of the most ductile metals with high electrical conductivity. The stretchability of the thin films is defined by the material and geometric properties of the thin films and the substrates (Song et al., 2009). The direct deposition of the thin solid metal on the elastic substrate can limit its stretchability due to the intrinsic mechanical and chemical mismatch. As a result, thin films usually have a low electrical reliability when it is stretched. To overcome this problem, pre-stretching the substrate layer before depositing the thin metal can significantly increase its stretchability (Lacour et al., 2003, Lacour et al., 2005). However, the use of thin films for manufacturing high-quality radio-frequency (RF) circuity and antennas for modern wireless communication is not suitable as a thin and long conductor is highly resistive.

2.3.2 Conductive Particles

Another way to make stretchable conductors is to disperse conductive particles in elastomer (Sekitani et al., 2008, Wang et al., 2018a). The conductive particles can be metallic (silver, Ag (Matsuhisa et al., 2017) or copper, Cu (Ding et al., 2016)) or carbonaceous (CNTs (Li et al., 2017), graphene (Lin et al., 2016), or carbon fibers (Liu et al., 2015)). Conductive nanomaterials are

embedded or dispersed into an elastomer for a better stretchability by combining the mechanical deformability of the elastomer polymer with the electric performance of the nanomaterial fillers. Unlike the bulk metals, conductive particles have interstitial spaces between the structures, and they allow light to pass through, making them translucent. However, since such composite contains non-conductive materials, the electrical conductivity of percolated structures is lower than the bulk materials. Moreover, the elastomer can compromise its mechanical properties with the addition of the conductive fillers.

2.3.3 Conductive Liquids

Liquids in elastic microchannels can flow freely without discontinuity without hysteresis and achieve an extreme level of deformation. A conformal electronic system can be created by embedding liquid conductors into elastomers such as PDMS (Cheng and Wu, 2012). Liquid conductors such as electrolyte solutions are common, but their low electrical conductivity has been a major limitation for the RF electronic components.

Mercury is a well-known conductive liquid metal (electrical conductivity of 1.04×10^4 S/cm), and it is commonly utilized in a variety of practical applications including barometers, thermometers, and fluorescent lamps. Mercury in the form of droplets has been used by the microfluidic systems as the miniaturized models of the macroscale thermal and electric contacts (Ray et al., 1993, Nalwa, 1999). However, due to its high toxicity (Clarkson and Magos, 2006) and very low vapor pressure, accidentally inhaled

mercury vapor can suppress many important physiological functions, which is harmful to the body. Furthermore, its intrinsically high surface energy (>400 mN m^{-1}) prevents it from forming a stable structure, making it challenging to be patterned into definite shapes for making antennas and wires. (Dickey et al., 2008).

Later years, low toxicity and melting temperature alloys have been getting attention as suitable alternatives. In 1875, Gallium is discovered as an alternative which has extremely low vapor pressure (it is effectively zero at room temperature) (Haynes, 2011), low toxicity (Chandler et al., 1994, Lu et al., 2015), and low melting point (30ºC). The melting point can be reduced by adding other metals such as tin (Galinstan, an alloy of 68.5 wt% of Ga, 21.5 wt% of In, 10 wt% of Sn) (Morley et al., 2008) and indium (Eutectic Gallium Indium, 75.5 wt% of Ga, 24.5 wt% of In) (Dickey et al., 2008, Chiechi et al., 2008) to create useful room-temperature liquid metals. As a result, the melting points of Galinstan and Eutectic Gallium Indium (EGaIn) are -19ºC and 15.5ºC, respectively. Both have a similar electrical conductivity of 3.4×10^4 S/cm.

The low viscosity characteristics of Gallium-based alloys make them easily be injected into microchannels. Then, rapid formation of the native oxide skin (~1-3 nm) occurs when exposed to oxygen and this will maintain the specific shape of the liquid in the microchannel (Dickey et al., 2008, Cademartiri et al., 2012, Regan et al., 1997, Scharmann et al., 2004, Plech et al., 1998, Chabala, 1992). They also can be manipulated in either the solid or liquid

form at specific temperatures since their melting temperatures are around room temperature.

2.4 Fabrication Methods for Stretchable Microfluidic Devices

As opposed to the conventional rigid electronic materials, elastomers and liquids and have drastically different mechanical properties. New fabrication techniques have been developed for the stretchable microfluidic devices. The fabrication techniques can be generally categorized as: liquid filling (injecting into a microchannel) and liquid printing (imprinting and selective surface wetting).

2.4.1 Injection Method

Injection is a simple approach for fabricating stretchable liquid-based electronic devices (Dickey et al., 2008, Cheng and Wu, 2012, Kim et al., 2008). By applying sufficient pressure from a syringe (or vacuum (Fassler and Majidi, 2013)), the oxide layer, which is to maintain the shape, starts to fracture and allow the liquid metal to flow into the microchannels. When the liquid is filled up, its oxide skin forms due to the presence of oxygen and create a stable structure within the microchannel (Dickey et al., 2008).

2.4.2 Imprinting Method

Imprinting liquid metal such as EGaIn with elastomeric molds is a simple patterning technique (Gozen et al., 2014). An elastomeric mold with a certain topographical feature pushes against a thin coating of liquid metal that has been distributed on a flat surface, forcing the liquid metal into the mold's holes. The EGaIn in the hole forms a thin Ga-oxide layer at the interface between the metal and the PDMS upon exposing to air, which helps in adhering to the walls of the cavity (Dickey et al., 2008). As a result, the metal can hold its molded shapes even after the mold is removed from the substrate (Gozen et al., 2014). This method is feasible to create liquid metal traces as thin as two-micron line width and submicron depth.

2.4.3 Selective Surface Wetting Method

This procedure was designed to sputter an intermediate layer of wetting. To facilitate wetting between the channel walls and liquid metal, a small coating of gold was sprayed onto the PDMS channel before printing the liquid metal using a Teflon squeegee (Kim et al., 2009). This ensures strong wetting between the PDMS channel and the liquid metal but increases the fabrication process complexity.

2.5 Introduction to Stretchable Strain Sensors

2.5.1 Background

Strain sensors/gauges are devices that can transduce mechanical deformations into electrical signals to determine the strain on an object (Lee et al., 2014, Suzuki et al., 2016). Recently, interest in stretchable strain sensors has been increasing as they can be used for the detection of human motion. Resistive- and capacitive-mechanism are often employed in stretchable strain sensors. Touch, strain, and pressure inputs can be detected by measuring the corresponding changes in resistance or capacitance of the sensors. These working mechanisms have relatively simple read-out systems (Amjadi et al., 2014, Yamada et al., 2011, Cai et al., 2013). Strain sensors of other mechanisms such as Raman shift, fiber Bragg grating (FBG), piezoelectricity, and triboelectricity for wearable applications are not so popular due to the poor dynamic performance, low resolution, and requirement of expensive measurement equipment (Obitayo and Liu, 2012, Guo et al., 2016, Gogurla et al., 2019, Khan et al., 2018, Rosenberger et al., 2014, Rantala et al., 2011). Hence, only resistive-type and capacitive-type strain sensors are focused in this thesis.

2.5.2 Comparison of Strain-Sensing Mechanisms

2.5.2.1 Resistive Sensing

Resistive-based sensors are usually made of conductive films and flexible substrates. The resistance value of the conductive sensing film changes when the composite structure deforms or stretches. When the structure stretches, there is a tendency to contract in the transverse direction due to Poisson's ratio of υ. The resistance of a conductor is given by $R = \rho L/A$, where A is the cross-sectional area, L is the length, and ρ is the electrical resistivity of the conductor. As a result, the conductor's resistance can be increased by increasing the conductor's length or decreasing the conductor's cross-sectional area.

Stretchable conductors, such as graphene, silver nanowires (AgNWs), single-walled carbon nanotubes (SWCNTs), and conductive polymers, are often used to manufacture the stretchable resistive strain sensors (Sahatiya and Badhulika, 2017, Chen et al., 2019, Shengbo et al., 2018). For a SWCNT-based thin-film stretchable strain sensor, it will fracture into islands and gaps with unpredictable manner, which can lead to non-linear resistivity (Yamada et al., 2011, Bocharov et al., 2016). On the other hand, axial elongation of an elastomer filled with liquid metal in the microchannel causes the microchannel to narrow in the transverse direction, based on Poisson's ratio. As a result, the resistance increases in a predictable manner (Overvelde et al., 2014, Park et al., 2010). These types of liquid-based sensors are suitable for human gait

monitoring (Wang et al., 2018b), measuring joint angle (Zhou et al., 2019), and soft robotic collision detection (Yeo et al., 2016).

2.5.2.2 Capacitive Sensing

For fabricating a capacitive strain sensor, the dielectric elastomer can be sandwiched by conductive elastomer electrodes. An algorithm technique called lumped-parameter equivalent electrical circuit is used to calculate the sensor's capacitance (Anderson et al., 2012). The electrodes are typically interdigitated (comb-drive) to create a patterned capacitive strain sensor with a large surface area (Kim et al., 2017). The initial capacitive C_0 of a parallel-plate capacitor with initial cross-sectional area (A_0), and dielectric layer's thickness (d_0), can be expressed as equation (2.1), as shown here:

$$C_0 = \varepsilon_o \varepsilon_r \frac{A_0}{d_0} \tag{2.1}$$

where ε_o and ε_r denote dielectric constant of vacuum and relative permittivity of dielectric media, respectively. Therefore, the capacitance of capacitive-type sensors increases when undergoing an increase in the capacitive area or a reduction in the dielectric layer's thickness.

A capacitive-based stretchable strain sensor can be fabricated using laser rasterization and metal deposition method. Since the conductive region has an electromechanical feature, the conductive electrodes can retain their conductivity even when subjected to a 250% strain and an 85% linear output.

To monitor breathing and human motions, this capacitive strain sensor was integrated into a thoracic belt and a wearable arm sleeve, respectively (Atalay et al., 2017). However, it has a smaller gauge factor than a resistive strain sensor due to the decrease of relative permittivity of the dielectric elastomer during elongation (Shintake et al., 2018, Tagarielli et al., 2012).

2.6 Introduction of Patch Antenna: Background, Theory and Analysis

2.6.1 Background

The demand for patch antenna has risen rapidly ever since its invention a half-century ago, particularly within the past two decades (Deschamps, 1953, Gutton and Baissinot, 1955, Munson, 1974, Carver and Mink, 1981). This is because of the patch antenna is easy to be fabricated, low profile, and integrable with other solid-state devices. These properties have led to the popularity of the patch antennas in both the military and commercial applications such as terrestrial cellular communications, mobile satellite communications, and global positioning systems (GPS).

The early development of the patch antenna is shown in Figure 2.5. The dielectric substrate, which has two sides (top and bottom), comprises of a metallic ground plane on the bottom and a radiating metallic patch on the top. Normally, rectangular or circular patch are often used in designing patch antenna. However, circular patch will be the focus of this thesis as only the radius of the patch (one degree of freedom) is needed to control.

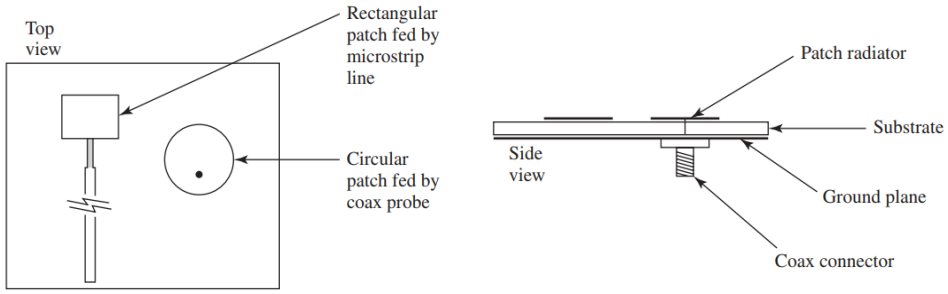

(a) (b)

Figure 2.5: (a) Top view and (b) side view of the patch elements fed by microstrip line or coaxial probe (Balanis, 2011).

2.6.2 Theory of Circular Patch Design

The circular patch antenna's modes are able to be identified by treating the substrate, ground plane, and patch as a circular cavity. The mode TM^z, where z is measured perpendicular to the patch, is supported primarily by a circular patch antenna with a low substrate height ($h << \lambda$). For the circular patch, only one degree of freedom can be manipulated, which is the radius of the patch. The order of the modes will not be altered by changing the patch radius but the resonant frequency will (Balanis, 2012). Figure 2.6 shows the general design of a circular patch antenna where the circular patch's radius (a) can be determined as follow:

$$a = \frac{F}{\left\{1 + \frac{2h}{\pi\varepsilon_r F}\left[\ln\left(\frac{\pi F}{2h}\right) + 1.7726\right]\right\}^{\frac{1}{2}}} \tag{2.2}$$

where

$$F = \frac{8.791 \times 10^9}{f\sqrt{\varepsilon_r}} \tag{2.3}$$

where

ϵ_r = dielectric constant of the substrate

f = resonant frequency, Hz

h = height of the substrate, cm

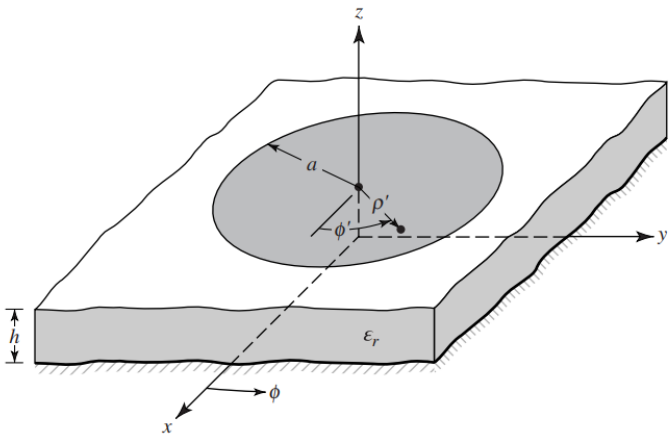

Figure 2.6: Geometry of circular patch antenna (Balanis, 2016).

2.6.3 Advantages of Liquid-based Patch Antenna

Most of the conventional microstrip patch antennas are rigid and unable to be bent as they are often constructed by etching the copper cladding to form static conductor shapes on the rigid substrates (Alzoubi et al., 2011). To overcome this, the rigid substrates and copper layers can be replaced with elastomers (such as PDMS) and EGaIn, respectively. As seen in Figure 2.7, injecting EGaIn through the elastomer's microchannels offers a simple route to shape the metal into a radiator, as reported in (Hayes et al., 2012). It can form highly stretchable liquid antennas, without compromising their electrical properties (So et al., 2009).

2.6.4 Additional Feature in Liquid-based Patch Antenna

With the high stretchability of the patch antenna, its electrical characteristics are altered at different mechanical strains, causing the operating frequency to shift; hence, it can also act as a reversible strain sensor (Cheng and Wu, 2011).

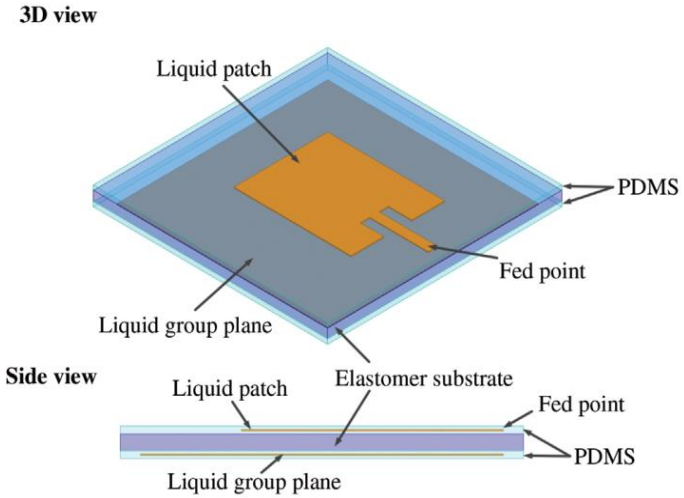

Figure 2.7: Structure of liquid metal patch antenna (Hayes et al., 2012).

2.7 Introduction of Dielectric Resonator Antenna: Background, Theory and Analysis

2.7.1 Background

With the fast development of low-loss ceramic materials since 1960s, many researchers have started to investigate dielectric resonators. Dielectric resonators are commonly employed in shielded microwave circuits (oscillators and filters) which are made from high-permittivity ($\varepsilon_r \approx 20-100$) and low-loss

materials (tan $\delta \approx 10^{-4}$) (Kajfez and Guillon, 1986). In 1983, the concept of dielectric resonator antenna (DRA) was created when the use of dielectric resonator as a radiator was first proposed by Long (Long et al., 1983). The DRA's dimension is in the order of $\lambda_0/\sqrt{\varepsilon_r}$, where ε_r is the resonator material's dielectric constant and λ_0 is the free space wavelength. A high value of ε_r able to significantly reduce the size of the DRA. Furthermore, the radiation efficiency is relatively higher due to the absence of inherent conductor loss in DRA. This characteristic is beneficial for antennas that have high loss in their metallic parts when operating in the millimeter (mm)-wave region.

Nearly all microwave and mm-wave transmission lines can be coupled using the DRAs simple coupling techniques. It makes them suitable for easy integration with different planar technologies. By adjusting the dielectric resonator's (DR) position in relation to the transmission line, it is possible to control the coupling between a DR and the line. As a result, it is simple to optimize the DRA's performance. The selection of right resonator parameters can vary the operating bandwidth of a DRA. Different radiation characteristics can be obtained by exciting different modes of a DRA.

2.7.2 Comparison of Excitation Schemes

A variety of feeding structures can excite different modes of a DRA, such as coaxial probe, microstrip-slot, microstrip line, and coplanar waveguide. When the coaxial probe is placed collinearly with the resonator axis, the $TM_{01\delta}$ mode is excited (Mongia et al., 1993b). Placing the probe away from the center

axis can cause the E_z component to be zero at the axis, which excites the $HE_{11\delta}$ mode, as shown in Figure 2.8 (a) (Long et al., 1983). However, for half-split cylindrical DR, the placement of probe conductor away from the center will excite the $TE_{01\delta}$ mode, as shown in Figure 2.8 (b) (Mongia, 1989).

The microstrip-slot coupling scheme shown in Figure 2.8 (c) and (d) is another excitation scheme that can be very useful for combining DRA with the microwave integrated circuits (MIC) (Martin et al., 1990). The ground plane is etched with a small rectangular design (slot) before placing the DR above, whereas the microstrip transmission line is located below the etched slot. The DR is excited via the microstrip line's fields "leaking" through the slot, where this method is commonly used in exciting the half-split cylindrical (Mongia et al., 1993a), rectangular (Ittipiboon et al., 1993), and spherical DRs (Leung et al., 1993).

An excitation scheme where the microstrip line contacts directly the DR was also proposed, as shown in Figure 2.8 (e) and (f) (Kranenburg and Long, 1988). This excitation technique may create surface waveguide modes in the dielectric substrate, even though it provides a highly convenient coupling scheme. Figure 2.8 (g) and (h) show that coplanar lines can also be used to excite DRs, which is quite promising especially for coupling the DRs to the monolithic MICs (MMICs) (Kranenburg et al., 1991).

2.7.3 Design of Resonant Frequency for Cylindrical DRA

Any dielectric structure can become a radiator at certain given frequencies by using the right excitation technique. The cylindrical and rectangular radiating dielectric resonators are the most common ones. However, the rectangular DRA is difficult to analyze due to the increased number of edge-shaped boundaries, whereas cylindrical DRA is widely used due to its simpler fabrication and the ability to excite various modes. Figure 2.9 shows the

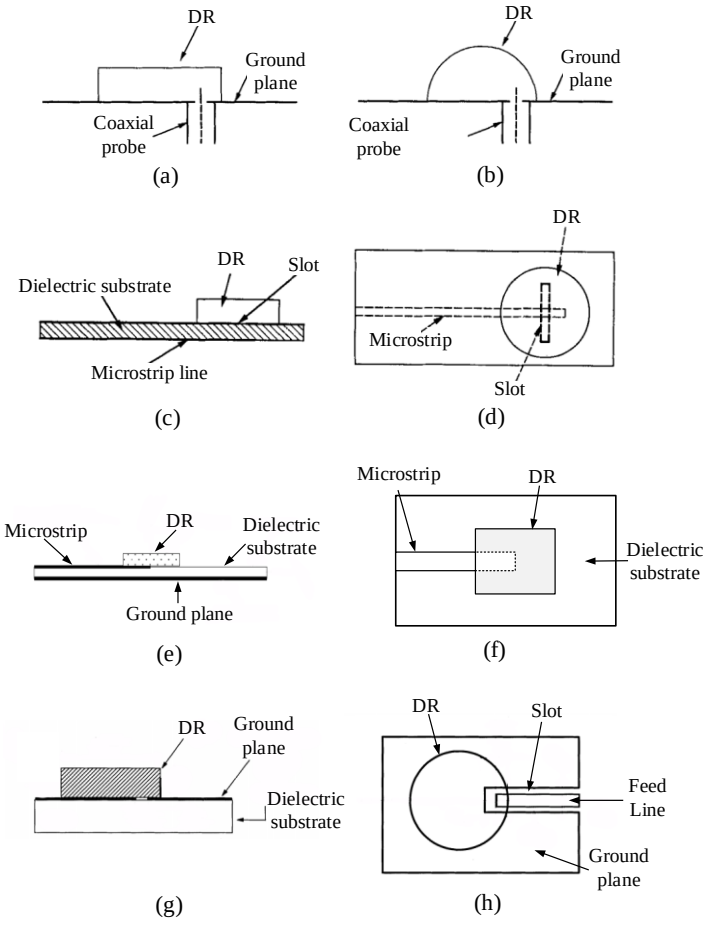

Figure 2.8: Probe excitation method for (a) a cylindrical DRA and (b) a half split cylindrical DRA placed on a metal plate. (c) Side view and (b) top view of a DRA with microstrip slot excitation method (Mongia and Bhartia, 1994). Microstrip feed method for a DRA at the (d) side view and (e) top view (Saed and Yadla, 2006). Coplanar waveguide scheme for a DRA at the (g) side view and (h) top view (Guo and Luk, 2003).

cylindrical DRA excited by probe feeding. The resonant frequency (*f*) of the cylindrical DRA for $HEM_{11\delta}$ mode can be determined using equation (2.4) taken from (Mongia and Bhartia, 1994).

$$f = \frac{6.324c}{2\pi a\sqrt{\varepsilon_r + 2}}\left[0.27 + 0.36\left(\frac{a}{2h}\right) + 0.02\left(\frac{a}{2h}\right)^2\right] \qquad (2.4)$$

where

a = dielectric radius, m

h = dielectric height, m

c = velocity of light in free-space, m/s

ε_r= dielectric constant

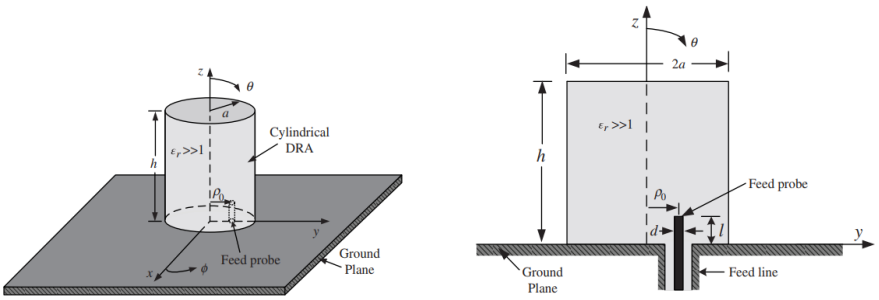

Figure 2.9: (a) Three-dimensional and (b) cross-sectional view of the probe-fed cylindrical DRA (Balanis, 2016).

A new configuration called ring/annular DRA can be created, as shown in Figure 2.10, if the central portion near the cylindrical axis is removed by an amount of radius *b*. The modes supported by this annular DRA are the same as those supported by a cylindrical DRA. An annular DRA's resonant frequencies, on the other hand, are higher than those of the cylindrical DRA. This is because removing the central portion decreases the DRA's effective dielectric constant, causing the radiation Q-factor to reduce and the bandwidth to increase at the same time.

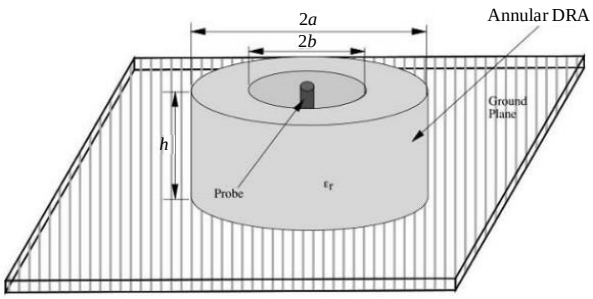

Figure 2.10: The probe-fed annular DRA.

2.7.4 Types of Dielectrics for DRA

The selection of a suitable dielectric to be used for designing a DRA is usually based on the electric capacitance per unit of volume (dielectric constant) and the energy loss per unit volume per cycle (dielectric loss). Traditionally, the solid dielectrics are often used due to their high dielectric constant and low dielectric loss. However, the difficulty to machine the brittle dielectric into a specific shape has led to the exploration of liquid dielectrics in recent years.

2.7.4.1 Solid Dielectrics

The introduction of rutile, with a high dielectric constant (around 100) in the 1960s, had reignited the interest in the dielectric resonators (Okaya, 1960). However, the rutile's low-temperature tolerance can cause unstable resonant frequency and prevent it from the production of practical microwave components. Then, in the 1970s, low-loss and temperature-stable ceramics, such as barium tetratitanate, $BaTi_4O_9$, and zirconium tin titanate, $(Zr\text{-}Sn)TiO_4$, were introduced and used for the design of the high-performance microwave components such as filters and oscillators.

The authors in (Leung et al., 2012) showed that the glass dielectric resonators could be used as light covers. This paper presents a dual-band hemispherical glass (hollow and solid) DRA. A light-emitting diode (LED) was inserted into the air gap of a transparent glass through the ground plane, resulting in a DRA that could be used as a light cover for the home lighting system. A plastic-based super-shaped DRA was also introduced in (Simeoni et al., 2011, Simeoni et al., 2009), where the polyvinyl chloride (PVC) was used as a dielectric material because of its low cost and easy to machine properties.

2.7.4.2 Liquid Dielectrics

Complex shapes of resonators are difficult to realize with using the conventional solid dielectrics that are hard and brittle; as a result, liquid dielectrics, which can offer fluidity and conformability, have been explored for designing various DRAs. The liquid dielectric can take any shape of the container. Different from the solid dielectrics, a liquid dielectric can partially recover its dielectric strength from the event of electrical breakdown, after the applied electric field is removed.

Pure water is typically used for the fabrication of the compact liquid dielectric resonator antennas (LDRAs) due to its high permittivity (ε_r ~ 78), abundance, and safety (O'Keefe et al., 2007, Zhou et al., 2014). However, the drawback of using water is that it has a high dielectric loss, which can degrade the radiation efficiency of the antenna at high frequency bands (>1 GHz). Furthermore, water has small tolerance on the phase changes as it can turn into

ice when the ambient temperature goes below 0ºC, which further limits the usage of water in the cold climate region.

Organic solvents, which have a larger temperature tolerance such as ethyl acetate, has been used to replace water (Chen and Wong, 2017b, Chen and Wong, 2017a). It is low in cost, low in toxicity, and stable in dielectric constant throughout the target frequency band. Furthermore, the freezing point of ethyl acetate falls below -89.3ºC, making the LDRA suitable to work at a low-temperature environment. Although the ethyl acetate has a low dielectric constant (ε_r ~ 5.77), its loss tangent (tan δ ~ 0.052) is much lower than that of water (tan δ ~ 0.13), which allows the LDRA to work at the UHF bands.

2.7.5 Advantages of Liquid Dielectric Resonator Antenna

LDRAs open up a new possibility of antenna design where its physical shape can be altered dynamically, such as changing the volume of the resonator in order to change the resonant frequency (O'Keefe et al., 2007). This feature allows the antenna to be fine-tuned to the frequency of transmission or tune to another band. A simple pumping arrangement can be used to perform the tuning of the antenna. This can also be used to compensate for fluctuations in the liquid's permittivity caused by temperature changes. The LDRA can be used for pattern (Chen and Wong, 2017b) and polarization (Chen and Wong, 2017a) reconfigurability by controlling the liquid volume in its container.

Easy prototyping is another advantage of the LDRAs. DRAs of unique shapes can sometimes be needed for certain experimental purposes. Molds and containers can be easily filled with liquid for the construction of a unique shaped LDRA. Also, usually for the solid DRAs, it is difficult to have a smooth surface contact between the ground plane and the solid dielectric or between the probe and the dielectric. Hence, small air gap may exist, and this can result in large discrepancies between simulated and measured results (Junker et al., 1994a, Junker et al., 1995, Junker et al., 1994b). Avoiding air gaps in the solid dielectric materials is extremely difficult but this problem can be solved with the use of the liquid dielectrics.

2.8 Introduction of Electromagnetic Bandgap for Wearable Antenna

2.8.1 Background

Ungrounded antenna such as dipole has a radiation pattern directed in both the upper and lower directions. As a result, human body will be exposed to such radiation if the antenna is directly placed on the human skin. To reduce the backward radiation, a perfect electrical conductor (PEC) can be used as a ground plane for isolating the antenna. However, an image current, which is opposite in direction (out of phase) with the antenna, is formed on the PEC. The dipole's radiation may be cancelled by the reverse image current, resulting in a low radiation efficiency. A perfect magnetic conductor (PMC) can replace the PEC to overcome the image current problem. Nevertheless, the existence of the PMC can affect the antenna impedance, causing impedance mismatch. As a

result, a new type of isolation mechanism is required to improve the radiation performance and impedance matching of the antenna.

Electromagnetic bandgap (EBG) structure can prevent the propagation of certain electromagnetic wavelengths due to its periodic nature. Therefore, EBG is useful for microwave applications. The EBG structure is made up of dielectric or metal elements that are repeated periodically. The EBG surface reduces the amount of unwanted radiation towards the human body by limiting the transmission of waves within a certain frequency range (known as a bandgap) (Sievenpiper et al., 1999, Yang and Rahmat-Samii, 2009).

2.8.2 Working Principle and Characteristics of EBG

With the presence of the EBG, the image current becomes in the same direction as the wire current (in-phase reflection), thus enhancing the antenna's radiation. Illustrations are shown in Figure 2.11. As a result, the EBG can reflect a large portion of the EM energy to the desired direction, which behaves like a EM reflector.

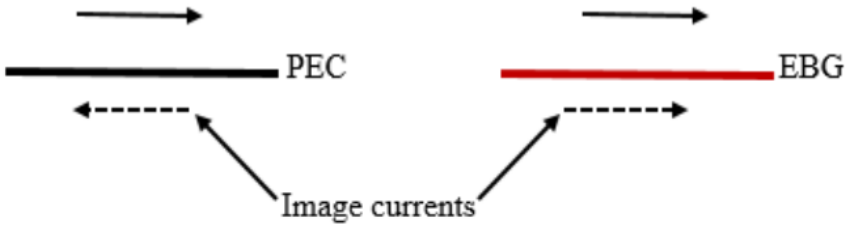

Figure 2.11: A wire current placed above the PEC and EBG surfaces (Zhu, 2008).

Reflection coefficient (ratio of the reflected wave to the transmitted wave) can be used to describe the reflection characteristics of the reflective surface. The reflection phases for PEC and PMC surfaces are constant 180º and 0º, respectively, whereas the EBG can configure the reflection phase between 180º to -180º. (Yang and Rahmat-Samii, 2003, Bashir, 2009, Sievenpiper et al., 1999). The reflection phase of a general EBG structure can be calculated by utilizing the frequency domain solver in the CST Microwave Studio to build a unit cell model, as shown in Figure 2.12. The frequency range at which the surface impedance exceeds the free-space impedance is taken to be the operating bandwidth, and it is defined as the range when the reflection phase falls within 90º and -90º. Also, the low-profile wire antenna can achieve a good reflection coefficient in the frequency range of 90º±45º (Yang and Rahmat-Samii, 2003).

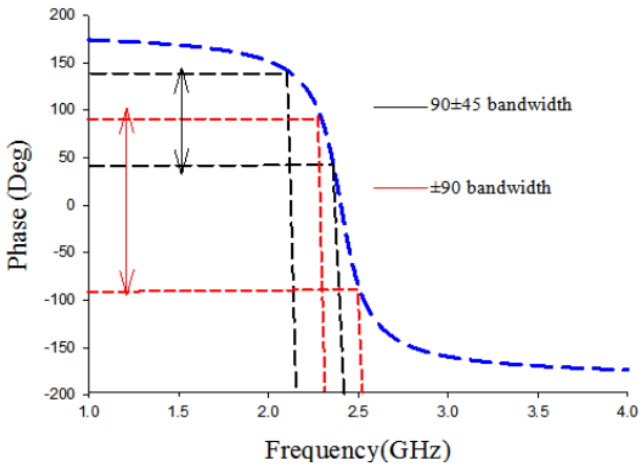

Figure 2.12: Reflection phase of an EBG unit cell (Ashyap et al., 2017).

Employing the EBG structure to control the reflection phase is crucial to ensure that the backward waves of an antenna are reflected in the same phase as the forward waves (in-phase). It can focus the EM energy in the antenna's

boresight direction, thus increasing the antenna's boresight gain, as shown in Figure 2.13.

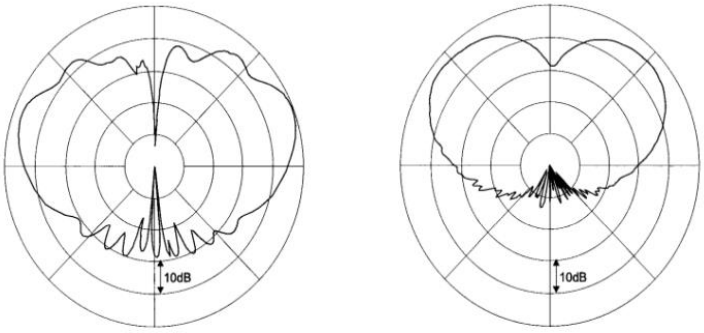

(a) (b)

Figure 2.13: A vertical monopole antenna's measured radiation pattern: (a) above the PEC ground plane and (b) above the EBG ground plane (Sievenpiper et al., 1999).

2.8.3 Design and Fabrication of Flexible EBG

Metal or dielectric elements are usually arranged in periodical patterns in typical EBG structures. Sievenpiper was the first to propose a mushroom-like EBG structure, where the structure consisted of metal patches, dielectric substrate, connecting vias, and ground plane, as illustrated in Figure 2.14 (Sievenpiper et al., 1999). The uniplanar electromagnetic bandgap (UC-EBG) is the other type of EBG configuration that offers a simpler design (no vias), cheaper, and higher compatibility with the standard planar circuit technology, making it better for wearable antennas (Zhu, 2008, Goussetis et al., 2006).

A parallel resonant circuit or an LC filter array can explain the working mechanism of the EBG structure, as illustrated in Figure 2.15. As the two neighbouring patches are separated by a small gap, it creates a capacitance effect,

whereas the current flow from one patch to the neighbouring patches through the pin vias creates inductance. For the UC-EBG (via-less), the inductance is caused by the proximity of the ground plane to the patch (Zhu, 2008, Bashir, 2009).

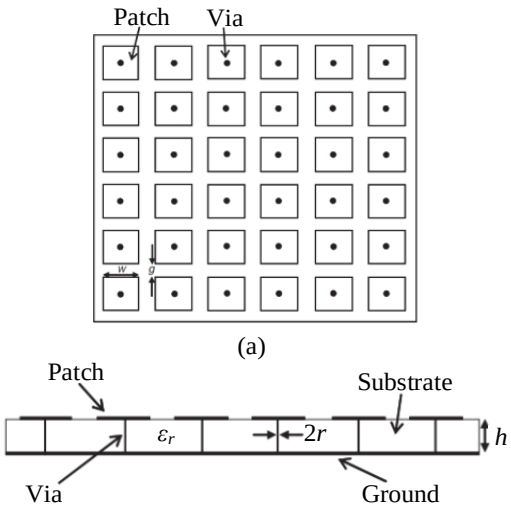

Figure 2.14: EBG surface: (a) Top view and (b) side view (Rea et al., 2006).

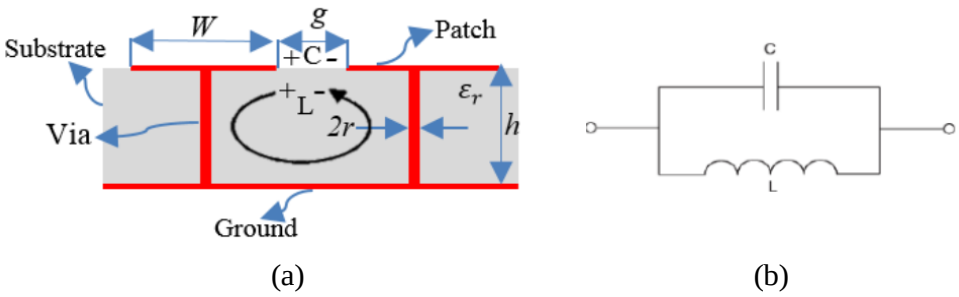

Figure 2.15: EBG unit cell (a) vias EBG parameters and (b) lumped element equivalent circuit of the EBG (Bashir, 2009).

2.8.3.1 Copper-based EBG

The EBG-based antenna design was first proposed in (Salonen et al., 2001). The use of the conventional inflexible FR-4 substrate was just to study the performance of the antenna near a human arm. Here, the antenna was

fabricated on FR-4 substrate, and the ground plane was etched with circles patterns to form EBG. Hence, the antenna with EBG has improved performance such as wider bandwidth, smaller footprint, lower backward radiation, and higher radiation gain. As it was built of the conventional inflexible FR-4 substrate, it was not suitable for wearable applications. To improve the flexibility, a thin bendable substrate such as RO3010 can be used to make the flexible EBG, making it conform better on the human skin, as shown in Figure 2.16 (Hadarig et al., 2013).

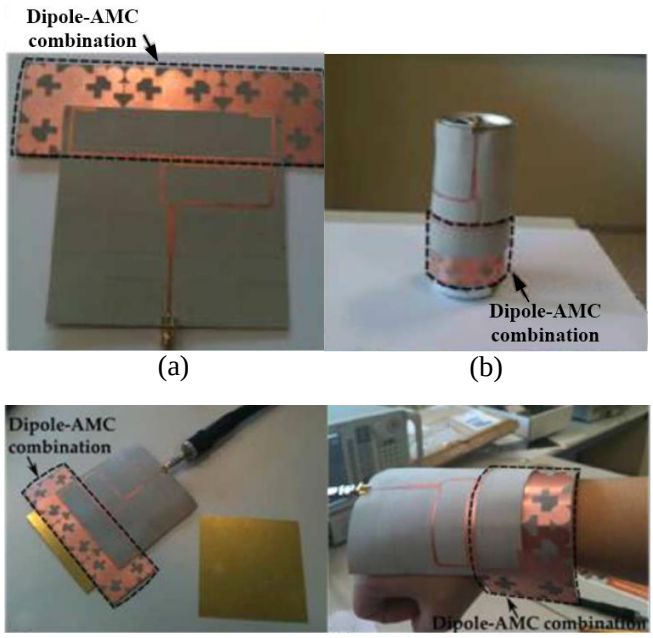

Figure 2.16: (a) Dipole-EBG made using the RO3010 flexible substrate. (b) Dipole-EBG bent and surrounding a metallic can. (c) Dipole-EBG being fixed over a metallic plate. (d) Dipole-EBG being conformed around the wrist (Hadarig et al., 2013).

2.8.3.2 Fabric-based EBG

Fabric materials were then subsequently used in developing completely wearable EBG antennas for improving comfortability when people were

carrying it as a wearable antenna (Salonen et al., 2004). Integrating fabric EBG with antenna also shows 50% improvement of the bandwidth and 30% reduction in antenna size, as compared with the antenna without EBG. The impact of bending and crumpling on the fabric antenna with fabric EBG was found to be very minor (Shakhirul et al., 2014, Hu et al., 2015). On the other hand, another study on the fabric-based wearable antenna shows that the antenna bandwidth and impedance can change with the moisture levels (Shakhirul et al., 2014). The fabric wearable monopole antenna is shown in Figure 2.17.

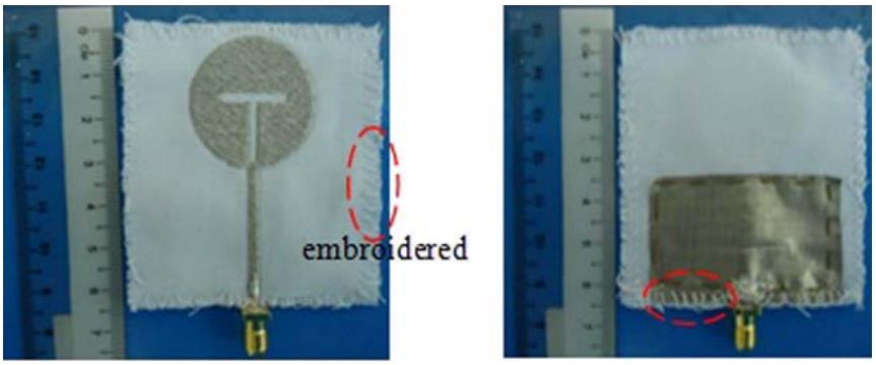

(a) (b)

Figure 2.17: (a) Front view and (b) back view of textile antenna with T-slot. (Shakhirul et al., 2014).

2.8.3.3 Elastomer-based EBG

To improve the stability of the wearable textile antenna under moisture conditions, the substrate is replaced with elastomer such as PDMS, as shown in Figure 2.18 (Gao et al., 2020, Simorangkir et al., 2016). This is because the PDMS has unique features such as water resistance and chemical stability, which improves the wearable performance of the antenna. To protect the conductive fabric, it can be encapsulated with the PDMS substrate, and the antenna's performance showed resilience under washability test (Simorangkir

et al., 2018). The stretchability can be further enhanced by replacing the conductive textile with AgNWs (Jiang et al., 2017).

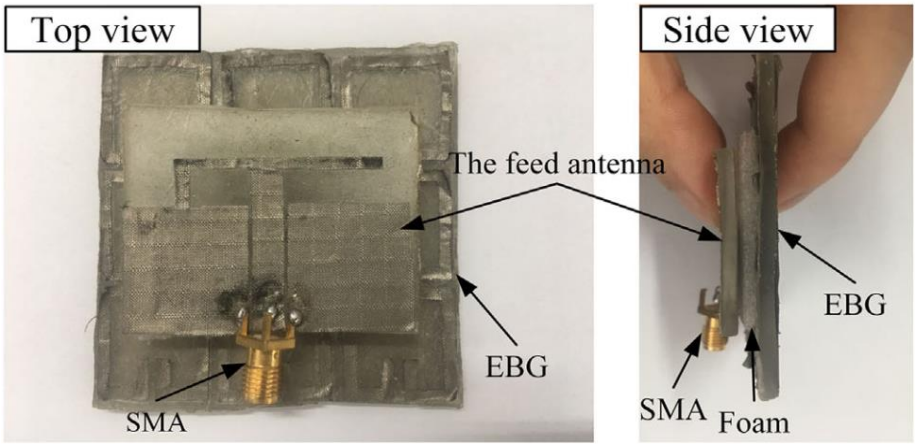

Figure 2.18: (a) Top view and (b) side view of a wearable PIFA with an EBG structure which is designed using the PDMS (Gao et al., 2020).

2.9 Conclusion

As this thesis involves both sensor and antenna elements, the fundamental backgrounds and theories of the stretchable sensors, patch antenna, DRA, and EBG for the wearable antenna have been reviewed. The materials such as elastomers and liquids have shown to be used in fabricating stretchable sensors and antennas. Elastomers such as PDMS and Ecoflex are often used to replace rigid substrates such as FR-4 to have better stretchability and conformity on human skin, whereas liquids (conductive and dielectric) are used to replace the solid conductors of the sensors as well as the radiator of the antennas. The EBG has better compatibility with the antenna, as opposed to PEC and PMC, as it can improve the impedance matching of the antenna and does not form opposite image current with the antenna. The EBG is used to reflect the EM wave away from the human skin and to improve the radiation performance of

the antenna. In this thesis, stretchable sensors with wireless capabilities will be implemented. As for the wearability, the EBG is chosen to be attached with the stretchable antenna to ensure the human body is unharmed during operation.

CHAPTER 3

DESIGN OF A WIRELESS SMART INSOLE USING STRETCHABLE MICROFLUIDIC SENSOR FOR GAIT MONITORING

3.1 Introduction

Conventional sensors using rigid components are non-flexible and non-conformal to human skin. They tend to get damaged when stretched beyond their strain limit. Hence, there is a need for stretchable materials to improve the conformity and durability of wearable sensors. In this project, a microfluidic sensor with high stretchability and good conformity to human skin was proposed. The microfluidic sensor can conform to human skin due to its flexibility and provide comfort to the user as it has a similar Young's Modulus of average human skin. Furthermore, the microfluidic sensor is made of Ecoflex 00-50, which is certified skin safe (Smooth-On, 2021). The proposed microfluidic sensor was fabricated by soft lithography which involves the use of 3D printed molds to form the microchannel for the conductive liquid to fill up. As a proof-of-concept, this sensor was used for gait monitoring by measuring the localized foot pressure and ankle angle. Owing to its unique and stretchable structure, the sensor is able to detect the pressure from the human foot and strain from the ankle joint.

3.2 Design and Working Principle

Figure 3.1 (a) shows the conceptual design of an EGaIn-filled stretchable sensor that can be attached on a shoe insole and displayed the gait parameters on a smartphone through Bluetooth communication. The entire length of the microfluidic channel is 348 mm. The microfluidic channel is designed in spiral shape with the outer diameter of 30 mm and a cross-sectional area of 1.0 mm (width) × 0.5 mm (height). This dimension is based on the minimum printing resolution in the 3D printing process. The spiral shape microfluidic channel is chosen because it can sense in both the longitudinal and transverse directions (Park et al., 2012). To monitor gait patterns at the plantar region, two stretchable sensors are placed around the heel and metatarsal areas as these are the regions which are exposed to greater stresses for broad age groups (children, young, and old adults (Shu et al., 2010, Kellis, 2001, Hessert et al., 2005)).

Figure 3.1 (b) and (c) show the simulated sensor's response when the pressure is exerted in the axial and normal directions, respectively. The simulation settings of COMSOL Multiphysics for the boundary conditions and loads for both axial and normal deformations are shown in Figure 3.1 (d) and (e). The physics module used was Solid Mechanics as it can be used to simulate force and deformation. In the Solid Mechanics settings, prescribed displacement (12 mm) was used for axial strain condition, and boundary load (1 N/m) was used for normal pressure condition. According to Pouillet's Law (equation (3.1)), the resistance (R) can be determined by the bulk resistivity (ρ) and the

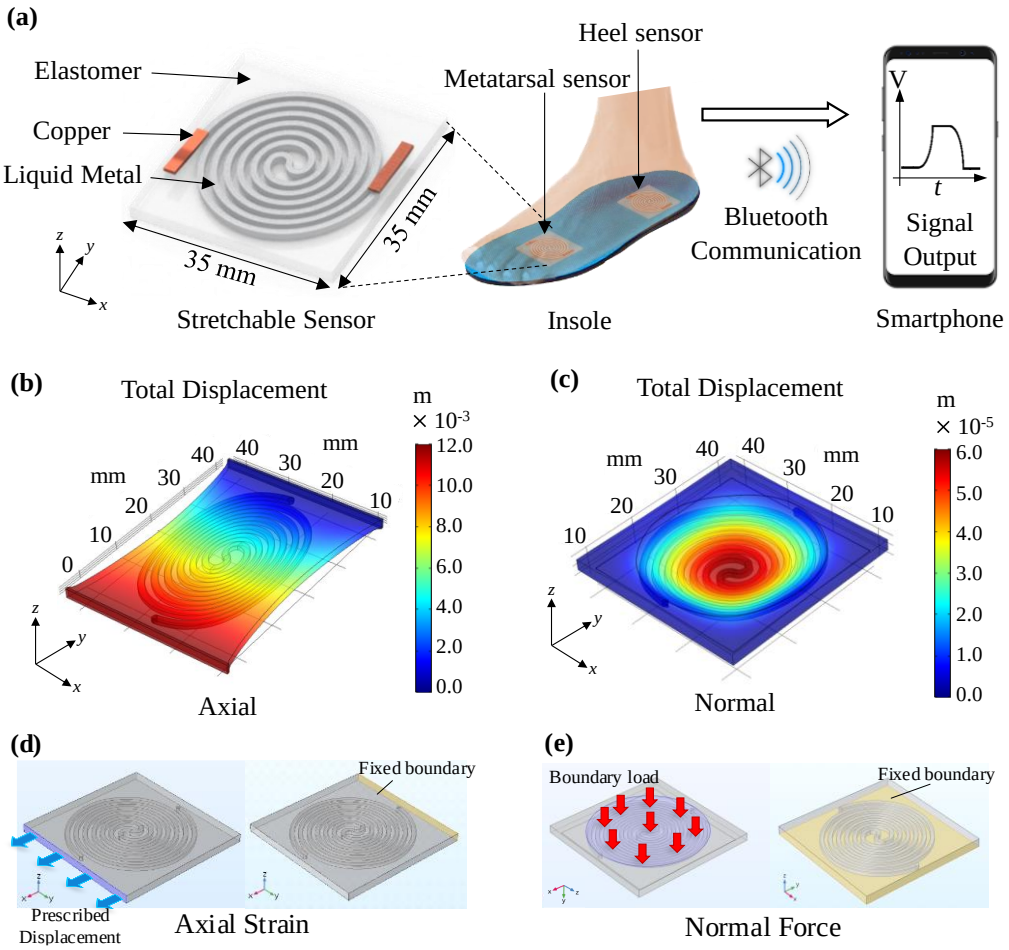

Figure 3.1: (a) The proposed sensor can be placed on the shoe insole to detect foot pressure. Resistance change of the sensor is transferred wirelessly through Bluetooth to a smartphone. Sensor deformation is modelled for (b) axial strain (c) normal pressure (The colours in the scale bar represent the magnitude of the sensor displacement). Simulation settings of COMSOL Multiphysics for the boundary conditions and loads for both (d) axial and (e) normal deformations. (Prescribed Displacement: 12 mm; Boundary Load: 1 N/m.)

dimensions (l/A) of the spiral pattern. When the spiral pattern is deformed, the electrical resistance of the EGaIn increases due to the reduction of the cross-sectional area.

$$R = \rho \frac{l}{A} \tag{3.1}$$

3.2.1 Strain Sensing

When the sensor is elongated, it lengthens in the direction of elongation and contracts transversely, simultaneously, according to the Poisson effect of the material. The following relationship can be used to explain the change of electrical resistance of the liquid metal:

$$\Delta R = \rho \left[\frac{L + \Delta L}{(w + \Delta w)(h + \Delta h)} - \frac{L}{wh} \right] \tag{3.2}$$

where ΔR is the change in electrical resistance, ρ is the electrical resistivity of the liquid metal, and h, w, and L are the height, width, and length of the channels, respectively (Park et al., 2012).

For elastomer, the material is incompressible, and the Poisson ratio is ν = 0.5. The relationship between the change in length, height, and width of the sensor is defined by the strain, $\epsilon = \Delta L/L$, such that $\Delta w = -\nu\epsilon w$ and $\Delta h = -\nu\epsilon h$. Applying these geometric conditions, the equation (3.2) can be simplified to

$$\Delta R = \frac{\rho\epsilon L(8 - \epsilon)}{wh(2 - \epsilon)^2} \tag{3.3}$$

To measure the joint angle, the sensor's response can be correlated to the distance change between two points that are connected across a joint. The change in length (ΔL) between these points can be related to the change in the joint angle ($\Delta\theta$) and scaled by the radius of the joint (r), that is, $\Delta L = \Delta\theta r$

(Mengüç et al., 2014). Hence, the equation of the sensor response to body joint rotation can be expressed as:

$$\Delta R = \frac{\rho L(8-(\Delta\theta r/L))}{wh(2-(\Delta\theta r/L))^2}\left(\frac{\Delta\theta r}{L}\right) \tag{3.4}$$

3.2.2 Pressure Sensing

Pressing the surface of the elastomer skin decreases the cross-sectional area of the microchannel and increases its electrical resistance. The relationship between the resistance change and contact pressure can be expressed as (Park et al., 2012):

$$\Delta R = \frac{\rho L}{wh}\left[\frac{1}{1-2(1-\nu^2)w\rho/Eh}-1\right] \tag{3.5}$$

where *E* is the elastic modulus of the elastomer material.

3.3 Fabrication of Microfluidic Sensor

3.3.1 Microchannel Fabrication

The microfluidic sensor was fabricated using the soft lithography technique. To ease the fabrication process, the microchannel was fabricated using the 3D printed scaffold-removal method (Saggiomo and Velders, 2015). First, a spiral-patterned microchannel mold was printed using a 3D printer (Ultimaker 3, Netherlands). The Ecoflex 00-50 (Smooth-On, Easton,

Pennsylvania) was then prepared in a mixing ratio of 1:1 (resin to hardener ratio) and poured into a petri dish. It was left for 4 hours at room temperature for the curing process to form a base layer with a thickness of 0.5 mm. Next, the 3D printed microchannel mold, which was made of the acrylonitrile butadiene styrene (ABS) material, was placed on the cured Ecoflex 00-50, as shown in Figure 3.2 (a), followed by pouring a second layer (1.5 mm) of Ecoflex 00-50 to encapsulate the microchannel mold, leaving only the two tips exposed (shown in Figure 3.2 (b)). Once the entire Ecoflex 00-50 was cured, it was removed from the petri dish (Figure 3.2 (c)) and immersed in acetone solution for 24 hours at the room temperature to soften and melt the ABS-made microchannel until a hollow microchannel is formed, as shown in Figure 3.2 (d).

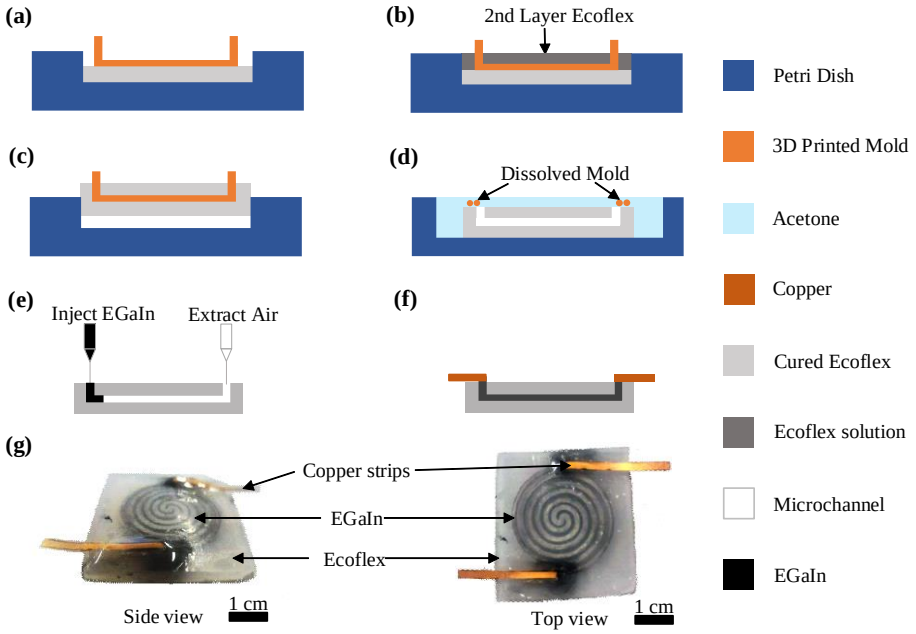

Figure 3.2: Fabrication processes: (a) The spiral-patterned mold was placed on a cured Ecoflex layer for fabricating the microchannel. (b) Ecoflex solution was then poured into the petri dish to form the second layer. (c) The cured Ecoflex together with the mold was removed from the petri dish. (d) The cured Ecoflex with the mold was immersed inside acetone for 24 hours. (e) The Ecoflex was removed from the acetone and the EGaIn solution was injected into the microchannel using two syringes. (f) The two ends of microchannel were connected to copper strips. (g) 3D view of the prototype of the stretchable sensor.

3.3.2 Injection of Liquid Metal into Microchannel

Here, the EGaIn liquid metal is injected into the microchannel using two syringes (one for injecting the liquid from the inlet and the other for withdrawing the trapped air in the outlet), as shown in Figure 3.2 (e). During the EGaIn filling process, air bubbles that are trapped in the microchannel may lead to the increase of resistance or even break the electrical connection. Hence, pre-strain process was performed during the injection of EGaIn where the sensor was stretched and pressed lightly to remove the trapped air bubbles.

3.3.3 Electronic Integration

Next, the two ends of the microchannel were attached with two electrodes, which are made of copper-clad polyimide film (AP9121, Pyralux Polyimide Film, DuPont, Singapore), for connecting electrically to an external electronic board. Finally, they are sealed with Sil-poxy^{TM} Silicone Adhesive (Smooth-on Inc, Pennsylvania) to prevent leakage, as shown in Figure 3.2 (f). The Sil-poxy^{TM} has a fast-curing time of 15 minutes and strong bonding with the Ecoflex 00-50 for enabling strong sealing. Figure 3.2 (g) shows the complete fabricated prototype with a dimension of 35 mm × 35 mm and a thickness of 2 mm. The nominal resistance of the sensor was measured as 0.6 Ω.

Figure 3.3 depicts the electronic integration of the fabricated prototypes for forming a smart insole system. With reference to Figure 3.3 (a), the two sensors are then connected to a pair of reference resistors of 1 kΩ (A larger

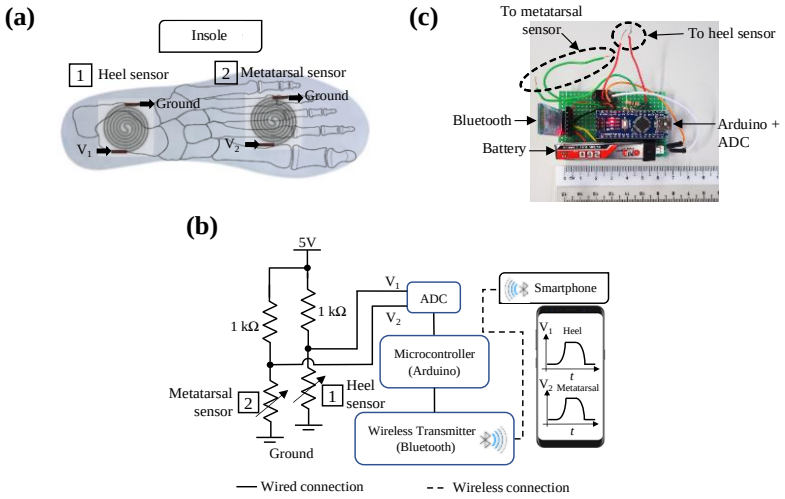

Figure 3.3: Schematic layout of the overall system. (a) Placement of sensors. (b) Electronic circuitry. (c) Circuit board.

value of reference resistor is used to accommodate a larger sensing range, as too low in the resistance value might cause short circuit (under no load condition)) to form a voltage divider so that the voltage changes can be measured at the metatarsal and heel regions. Figure 3.3 (b) shows the output voltage of each sensor is first sent to the analog-to-digital converter (ADC) module. Next, the digital signals are processed by the microcontroller module (Arduino Nano ATmega328) and, finally, the processed signals are sent to a smartphone through a Bluetooth module (HC-05). All the components in the electronic circuitry are shown in Figure 3.3 (c).

3.4 Experimental Results and Discussion

3.4.1 Experimental Setup

Figure 3.4 (a) and (b) show the experimental setups for measuring the sensor response in the normal and axial directions. Shimadzu ServoPulser E-

series (Shimadzu, Kyoto, Japan) was used for both characterizations. The output of the sensor was measured using the NI ELVIS Board II+ (National Instrument, United States) with a sampling rate of 3.5 Hz. The data obtained were analysed using the NI LabVIEW.

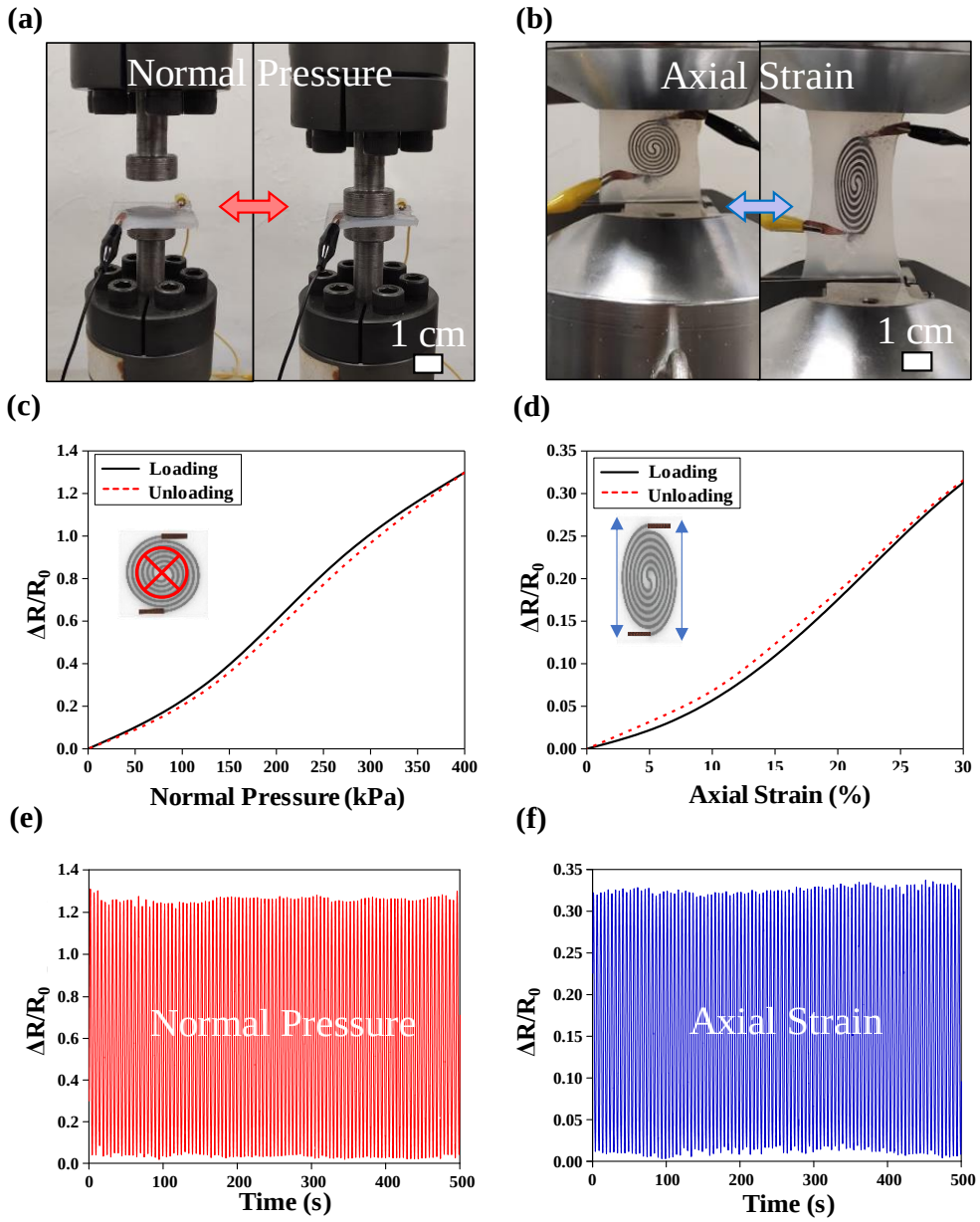

Figure 3.4: Experimental setups for (a) normal pressure and (b) axial strain of sensor. Sensor's output characteristics for (c) normal pressure and (d) axial strain. The mechanical durability characterization of sensor under 100 continuous working cycles for (e) normal pressure and (f) axial strain.

3.4.2 Sensor Characterization

The sensor was tested with high pressing load of 0 to 400 kPa (equivalent to the human weight of 50 kg). The motorized platform was translated with a linear speed of 0.2 mm/s. Figure 3.4 (c) shows the resistance of the sensor behaves non-linearly when a force is applied/released in the normal direction, as can be anticipated from equation (3.5). The dominant factor that contributes to the change of resistance in the normal direction is mainly attributed by the reduction of the cross-sectional area of the spiral microchannel. For strain test, the sensor was stretched up to 30% strain (10.5 mm) with a linear speed of 4.2 mm/s. The outputs in Figure 3.4 (d), on the other hand, shows linearity in strain sensing (Park et al., 2012). Referring to Figure 3.4 (c) and (d), the mechanical loading and unloading processes pose hysteresis with the percentages of 5.01%, and 4.24% for normal pressure and axial strain sensing, respectively. The hysteresis is mainly due to the properties of the polymer material (Park et al., 2012). It is worth noting that the hysteresis is within sensing tolerance and quite similar to the reported work in (Mengüç et al., 2014). The robustness of the stretchable resistive-based sensor was characterized by applying/releasing a pressure of 400 kPa, and strain of 30%, for 100 cycles for both cases, under a 0.2 Hz. As can be seen from Figure 3.4 (e) and (f), there is no obvious degradation, indicating good sensor's stability and durability.

3.4.3 Gait Monitoring of Plantar Region

Then, the characterized sensors were placed at the front and back positions of a shoe insole to detect pressure changes at the metatarsal and heel regions, respectively. A subject was instructed to wear the shoe insole on his left foot and walk on a treadmill. The speed of the treadmill was controlled such that the walking speed of the subject was maintained at a constant speed of 2 km/h with zero inclination angle. With the same parametric settings, the speed of the treadmill was then increased to 5 km/h to monitor the subject's running pattern. Figure 3.5 (a) and (b) depict the respective output signals of the sensors for the walking and running motions. The two output responses were all

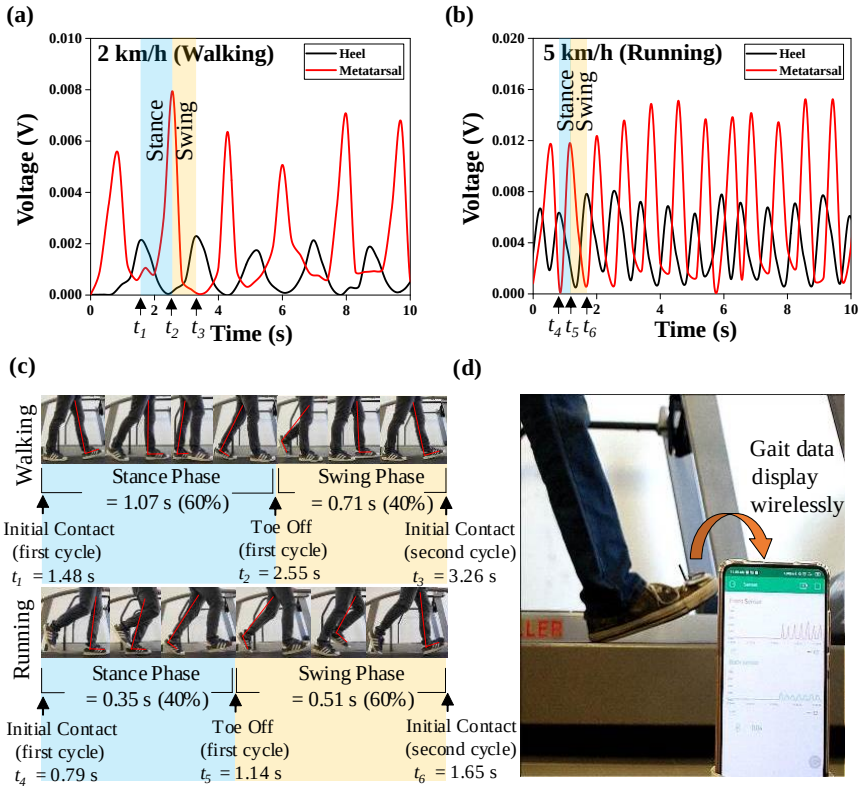

Figure 3.5: Sensors' outputs in terms of voltage for (a) walking gait and (b) running gait of the left foot. (c) Experimental motions for walking gait (top) and running gait (bottom). (d) The gait analysis viewed from a smartphone through Bluetooth communication.

compared in the same time frame of 10 s. It can be observed that, in every gait cycle, the sensor in the metatarsal region produces larger output responses than the heel region. A gait cycle is measured from a heel strike to the subsequent heel strike of the same foot. It is consisted of stance and swing phases. Stance phase refers to the motion of the heel when it makes an initial contact with the ground until the toe takes off from the ground; whereas swing phase is the period where the toe takes off from the ground and moves forward until the heel makes the next initial contact with the ground (Tao et al., 2012). Referring to Figure 3.5 (a) and (b), the period of the peak response from the heel to the metatarsal region is labelled as stance phase, whereas the period of the peak value from the metatarsal to the heel region is labelled as swing phase. The response time for the sensor is 0.286 s, which is sufficient to capture the data. Figure 3.5 (c) compares the stance phase (blue region) and swing phase (orange region) for the walking and running motions. It can be observed that, for a gait cycle (1.48 s to 3.26 s) of walking motion, a stance phase of 60% was measured, which was higher than the swing phase (40%). Running motion, on the other hand, has lower percentage of stance phase (40%) than the swing phase (60%) in a gait cycle (0.79 s to 1.65 s). With reference to Figure 3.5 (c), the results are agreeing well with those reported in (Whittle, 2014, Ounpuu, 1994), showing that the sensor is able to identify walking and running motions of a subject accurately. Figure 3.5 (d) shows the output voltages of both the heel and metatarsal sensors that are displayed on a smartphone through Bluetooth communication, which enables unobtrusive and real-time gait monitoring application.

3.4.4 Ankle Joint Angle Sensing

The stretchable resistive-based sensor can also be used for flex sensing application, such as ankle joint angle. The sensor was firmly attached onto the ankle support, then the ankle was moved in plantarflexion and dorsiflexion. The experiment results were plotted in Figure 3.6 (a) and (b). Figure 3.6 (a) shows the sensor's linear output in terms of the relative change of resistance at different ankle's joint angles. As compared to the piezoelectric-oriented flex sensing technique, the resistive-based sensing mechanism offers the advantage of speed independence (Cao et al., 2019). To evaluate the ankle's joint angle at a gait cycle, similar to the previous setup, the subject was instructed to walk on the treadmill with the speed of 2 km/h. The experimental result in Figure 3.6 (b)

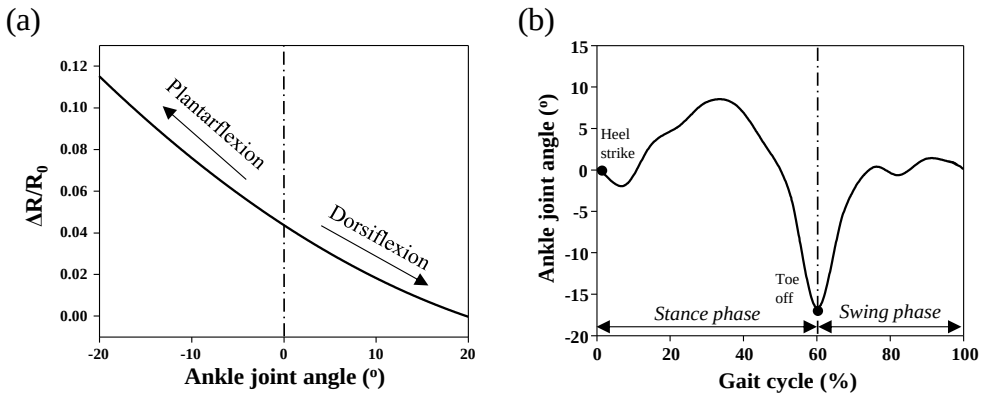

Figure 3.6: Experimental results of the sensor for (a) different ankle joint angles and (b) gait cycle of the subject's left ankle.

shows ~ 60% of the gait cycle was measured in a stance phase (defined as the ankle of 0º (heel strike) to extreme plantarflexion ~ -15º (toe off)), whereas ~ 40% of the gait cycle was measured at the swing phase (defined as the ankle returns to ~0º just after the toe off). This result shows a similar agreement with

those reported in (Mai and Commuri, 2016, Mengüç et al., 2014), proving the capability of the sensor in flex sensing.

3.5 Summary

This work has demonstrated a stretchable microfluidic-based resistive sensor for gait monitoring application. Our approach was to integrate a shoe's insole with soft sensor that has liquid metal embedded in microfluidic channel, enabling a soft, flexible, and deformable structure. Experimental results confirm that the soft sensor is able to sense the foot pressure in the plantar region (metatarsal and heel) and ankle joint angle. As an application for gait monitoring, the fabricated soft sensor is able to detect the pressure from the human foot by capturing accurately the weightages of the stance and swing phases. The data was then wirelessly transmitted to a smartphone via an external Bluetooth communication device to demonstrate real time monitoring.

CHAPTER 4

DEFORMABLE LIQUID METAL PATCH ANTENNA FOR AIR PRESSURE DETECTION

4.1 Introduction

In the previous project, stretchable sensor can be developed by replacing rigid substrate with elastomer and circuits with conductive liquid, and it can be made into wearable device. However, due to its non-self-wireless capability, an external Bluetooth is required for wireless data transfer, which increases the footprint of the overall design. In this project, a deformable liquid metal patch antenna, which is loaded with an air cavity underneath, is proposed for designing an air pressure-detecting antenna. Both the EGaIn and air cavity of the antenna structure are constructed inside a soft and deformable PDMS substrate. The existence of the air cavity has been proven to be crucial for making the antenna structure deformable. Here, the stretchable liquid antenna can work as a passive wireless air pressure sensor as its resonant frequency will change at different geometrical deformation (Wang et al., 2015, Cheng and Wu, 2010). The comparison between the two sensors is shown in Table 4.1.

Table 4.1: Comparison Between Previous and Current Proposed Sensor.

Type of Sensor	Functions	
	Physical Sensing	Wireless
Stretchable Sensor (Chapter 3)	Yes	No
Liquid Metal Patch Antenna (Current)	Yes	Yes

4.2 Antenna Configuration

The design of the proposed antenna is shown in Figure 4.1 where it is intended for operating at the resonant frequency of 5.8 GHz to miniaturize the antenna size and adhere to the Industrial, Scientific and Medical (ISM) standards. The building blocks of the antenna comprise two stretchable layers, each of which consists of a cavity, and both are made of the PDMS Sylgard 184 (ε_r = 2.5, tan δ = 0.08). An open-ended coaxial probe method (Lee et al., 2013) has been employed for measuring the dielectric properties. As can be seen from Figure 4.1, the top layer encapsulates liquid metal while the bottom layer comprises an air cavity, enabling the antenna to function as an air pressure sensor. The patch is circular in shape and the corresponding radius (r_m) for the TM_{110} mode (Balanis, 2016, Balanis, 1999) can be calculated using equation (2.2) and (2.3). Finally, the two layers are stacked and mounted on a square metallic ground plane (60 mm × 60 mm) to form the final antenna structure.

The design procedure starts from a simple thin circular patch that is made on a PDMS substrate (h = 4.5 mm) with infinite ground. To make the circular patch antenna resonates at 5.8 GHz, with the use of (3.2) and (3.3), the patch radius is calculated to be r_m = 8.23 mm. Then, the calculated radius is employed for constructing a simulation model using the CST Microwave Studio for verification. In the simulation process, the liquid patch ($\sigma = 3.4 \times 10^4$ S/cm with $t_1 \sim 0$ mm) is placed on the same PDMS substrate (d_2 = 20.8 mm & h = 4.5 mm) without any air cavity which is mounted on a ground plane (60 mm × 60 mm) and fed with a coaxial probe. In this case, the resonant frequency is found

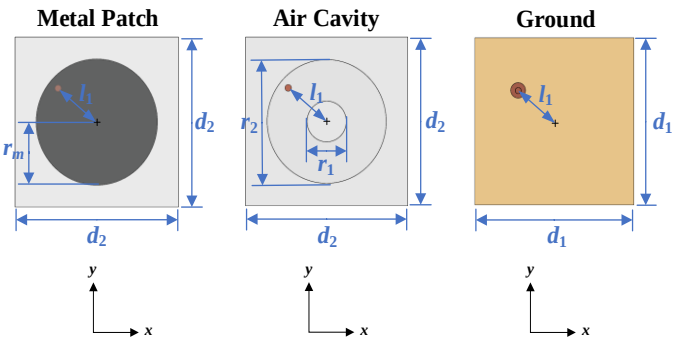

(a)

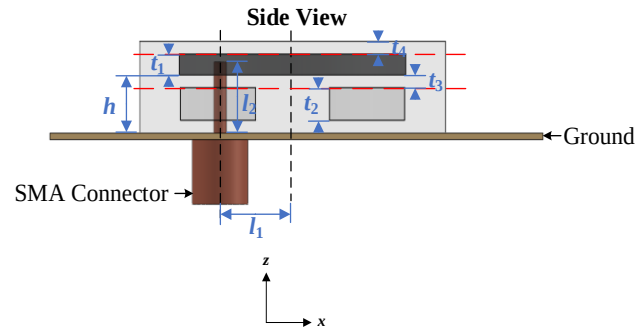

(b)

Figure 4.1: (a) Top view and (b) side view for the design of the proposed patch antenna.

to 5.887 GHz, which deviates only 1.5% from the calculated value. Next, the patch thickness is increased to t_1 = 1 mm, and it is encapsulated with the PDMS material to form the container for holding the metallic liquid. The antenna volume is increased, and it has further lowered the resonant frequency down to 5.416 GHz. Finally, an annular-shaped air cavity, which has a supporting beam at the center, is formed by removing a portion of the substrate under the patch, shifting up the resonant frequency to 5.926 GHz. Due to the loading effect of the air cavity, the effective permittivity decreases, and it causes the resonant frequency to increase. It will be proven that the inclusion of the air cavity is a crucial factor that enables the antenna structure to be used for sensing air pressure. Fine-tuning such as adjusting the feeding probe offset distance (l_1) is conducted on the antenna to bring the resonant frequency close to 5.8 GHz.

Finally, the length of the feeding probe (l_2) can be adjusted to improve the impedance matching of the patch antenna. As can be justified from the simulated resonant electric and magnetic fields shown in Figure 4.2, the proposed liquid patch antenna is excited in its fundamental TM_{110} mode. The final optimized parameters of the antenna working at 5.860 GHz are shown in Table 4.2. The fabricated liquid patch antenna is shown in Figure 4.3.

Table 4.2: Dimensions of The Liquid Patch Antenna.

Parameter	Dimension (mm)	Parameter	Dimension (mm)
d_1	60.00	t_3	1.00
d_2	20.80	t_4	1.00
r_1	4.00	l_1	6.36
r_2	18.00	l_2	5.00
t_1	1.00	r_m	9.00
t_2	2.50	h	4.50

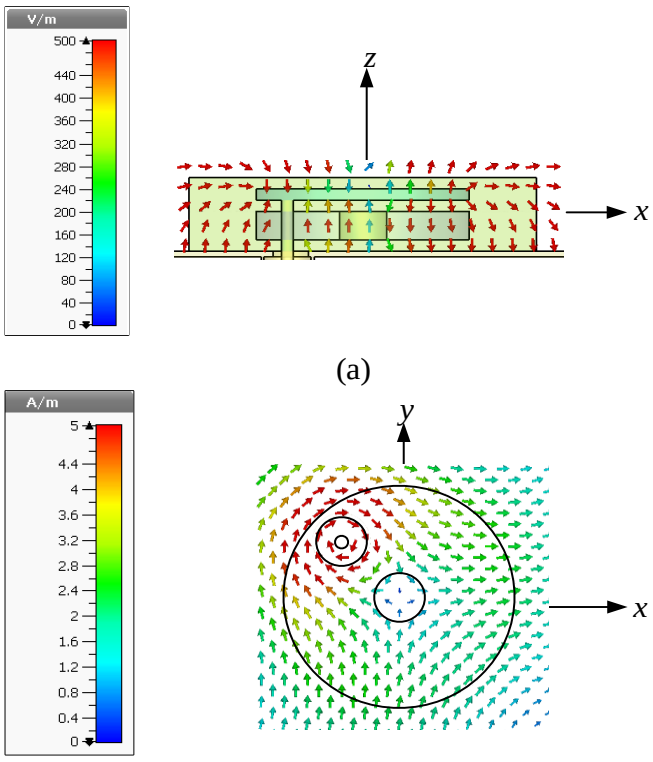

Figure 4.2: Distributions of the (a) electric fields and (b) magnetic fields of the liquid patch antenna.

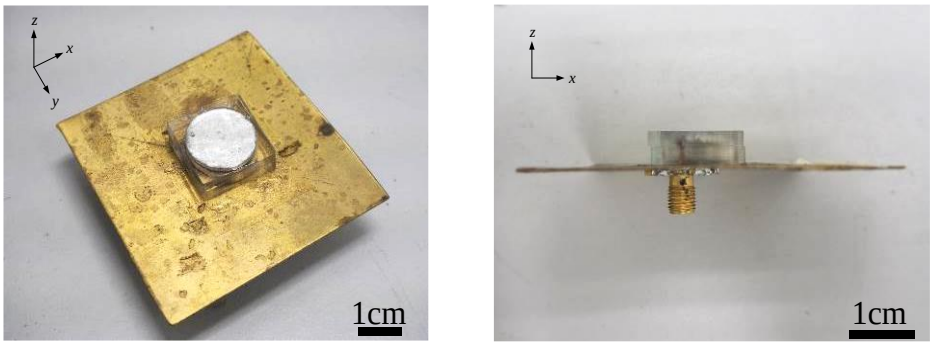

(a) (b)

Figure 4.3: Prototype of the proposed liquid patch antenna (a) 3D view and (b) side view.

4.3 Device Fabrication

The fabrication process of the proposed liquid patch antenna is shown in Figure 4.4. It is started with the fabrication of the flexible containers, which are made using the soft-lithography technique, for holding the liquid metal and air cavity, as shown in Figure 4.4 (a) to (c). To ease the fabrication, the PDMS container is split into three different layers (highlighted in dotted red lines in Figure 4.1 (b)), all of which are separately made, and they are sealed together at the end. First, three different plastic molds were printed using a 3D printer (Ultimaker 3, Netherlands). Next, the PDMS Sylgard 184 (Dow Corning Corp.) solution was prepared with 10:1 ratio of monomer and curing agent. The prepared PDMS solution was then placed in a desiccator for degassing before pouring into the three plastic molds. Trapped air bubbles in the PDMS solution can affect its electrical properties, which alter the resonant frequency of the antenna. All the plastic molds with PDMS solution were subsequently heated up to 65ºC using a hot plate for four hours to accelerate the curing process. Cured PDMS has low dielectric constant (2.5) and low loss tangent (0.08). The three PDMS layers were then peeled from the molds once they were cured. A

copper-made ground plane was first soldered with a SMA connector to enable probe feeding, as shown in Figure 4.4 (d). Then, the bottom PDMS layer was attached onto the ground plane by penetrating it through the probe. The PDMS layer was stuck to the ground plane using double-sided adhesive (Adhesives Research Inc., USA), as shown in Figure 4.4 (e). Then, the penetrated hole was sealed up using silicone adhesive (Sil-Poxy^{TM}, Smooth-On, USA) to prevent leakage. The other cured PDMS layers were also sealed together one-by-one using silicon adhesive (Sil-Poxy^{TM}, Smooth-On, USA) in the sequence shown in Figure 4.4 (f) to (g). The combined structure has two cavities. The first cavity in the bottom is filled with ambient air, and the second cavity in the top layer is filled with EGaIn using two syringes (one for injecting the liquid metal and the other for withdrawing the trapped air in the cavity), as shown in Figure 4.4 (h). The injected holes were sealed to prevent leakage. Finally, the completed prototype is shown in Figure 4.4 (i). We had initially thought of adding the liquid metal on the cavity of the top layer before sealing it with the cover lid. However, during the experiment, we found out that the liquid metal beaded up in the absence of oxide due to its high surface tension (~624 mN/m) (Dickey, 2017, Zrnic and Swatik, 1969). Hence, with the use of injection method (with 2 syringes), the liquid metal, which has low viscosity, readily fills up the cavity when a sufficient pressure is applied to yield the oxide layer (Dickey et al., 2008). This method ensures that the liquid metal fills the cavity entirely. Since PDMS is highly permeable to oxygen, the liquid metal in the cavity rapidly forms an oxide layer and it causes the liquid metal to stick to surfaces of the PDMS walls and stabilizes the shape of the liquid metal.

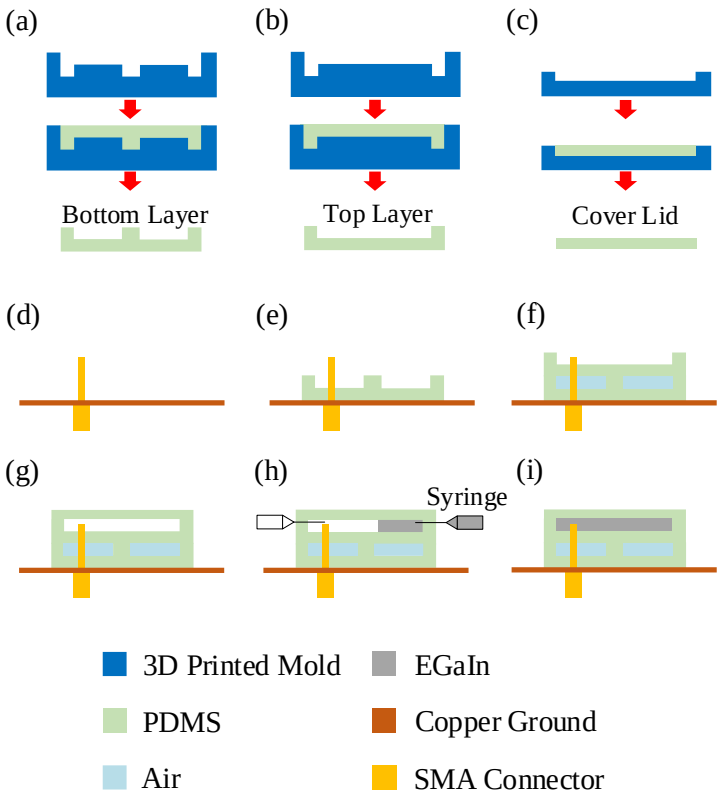

Figure 4.4: Fabrication process of the liquid patch antenna. Filling and curing of PDMS for (a) bottom layer, (b) top layer, and (c) cover lid. (d) Soldering SMA connector to the ground plane. Attaching the (e) bottom layer, (f) top layer, and (g) cover lid. (h) Injecting EGaIn into the cavity. (i) A completed liquid patch antenna.

4.4 Experiment Results and Discussion

4.4.1 Radiation Characterization

The simulations of the antenna were done using CST Microwave Studio, and measurements were carried out using a Rohde & Schwarz Vector Network Analyzer (VNA) to verify the simulated results. Figure 4.5 (a) and (b) show the antenna's simulated and measured results for both reflection coefficients and input impedances, having reasonable agreement. The simulated and measured resonant frequencies are 5.860 GHz and 5.806 GHz, respectively, with an error of 0.92%. The impedance bandwidths for simulated and measured are 14.74%

and 13.68%, respectively. The liquid patch antenna's simulated and measured radiation patterns are shown in Figure 4.6. As can be observed from the figure, the boresight direction shows an 8.02 dBi measured maximum antenna gain at 5.806 GHz, being slightly lesser than simulated maximum gain of 8.21 dBi at 5.806 GHz. A discrepancy of 0.19 dBi can be due to experimental fabrication tolerances.

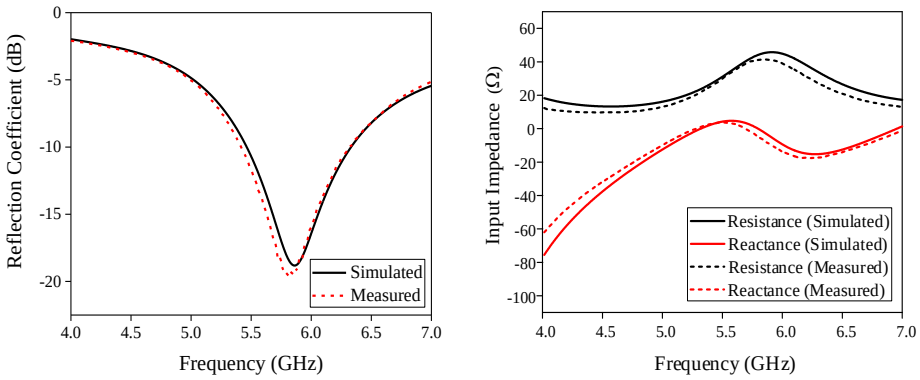

(a) (b)

Figure 4.5: Simulated and measured (a) reflection coefficients and (b) input impedances of the proposed liquid patch antenna.

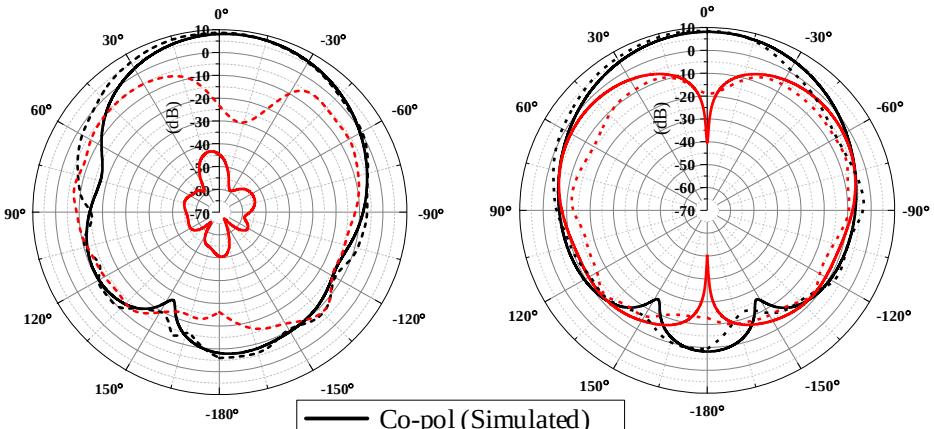

(a) (b)

Figure 4.6: Simulated and measured radiation patterns of the proposed liquid patch antenna for the (a) *E*- and (b) *H*-planes at 5.806 GHz.

4.4.2 Air Pressure Sensing

A pressure chamber, as shown in Figure 4.7 (a), has been constructed for analyzing the reflection characteristics of the proposed liquid patch antenna, which is connected to the VNA through a via hole on the base, under different ambient pressures. A glass cover, an air pump, and a pressure gauge are engaged for controlling and keeping the air pressure in the pressure chamber. The air pressure here refers to the gauge pressure which is zero-referenced against the ambient pressure. The antenna can only be tested in the range of -0.4 bar to 0.4

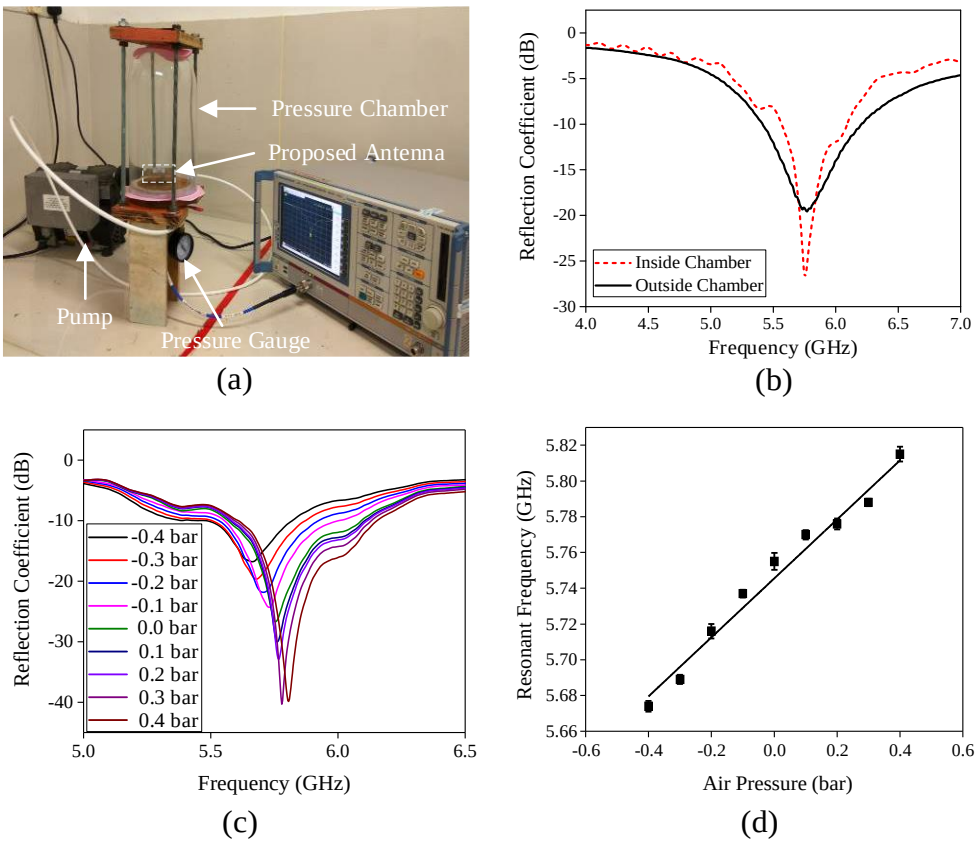

Figure 4.7: (a) Experimental setup for applying ambient pressure. (b) Comparison of reflection coefficients when the antenna is placed inside and outside the pressure chamber. (c) Measured reflection coefficients for ambient pressure from -0.4 to 0.4 bar. (d) Resonant frequency as a function of air pressure change.

bar due to the limitation of our pressure chamber. To understand the effects of the glass cover, reflection coefficients are measured by placing the liquid patch antenna inside (with glass cover) and outside (without glass cover) of the pressure chamber. It can be shown in Figure 4.7 (b) that the cover glass does not affect the resonant frequency much (~0.88%). To start the pressure test, the chamber is initially set at zero-gauge pressure (only atmospheric pressure). Figure 4.7 (c) shows the reflection coefficients, with the corresponding resonant frequencies shown in Figure 4.7 (d), when the ambient pressure is varied from -0.4 bar to 0.4 bar. With reference to Figure 4.7 (d), it can be seen that the liquid patch antenna's resonant frequency changes linearly with the ambient pressure in the range of 5.674 GHz–5.815 GHz. For every increment of 0.1 bar, the resonant frequency increases by approximately 0.0176 GHz. When the air pressure returns to zero at the release of pressure valve, the resonant frequency does not exhibit any hysteresis, indicating the antenna is reversibly deformable. In other words, the resonant frequency of the antenna structure is stable, and it can be easily restored after the external air pressure is removed, which is an important feature for frequency reconfiguration. This is possible due to the linear deformation of the PDMS at low strain (<40% strain) (Schneider et al., 2008, Johnston et al., 2014), which follows the linear relationship of Hooke's law.

The deformation of the proposed liquid patch antenna is also simulated and analyzed using the COMSOL Multiphysics software. Again, it is studied for the ambient pressures of -0.4 bar and 0.4 bar. Figure 4.8 (a) and (b) show the deformation of the proposed antenna (with air cavity) upon the exertion of

a fixed ambient pressure. At the normal ambient pressure (0 bar), external pressure exerting on the surfaces of the antenna structure is balanced out by the internal air pressure inside the air cavity. When the ambient pressure is reduced (<0 bar), the air pressure inside the air cavity of the antenna becomes larger. Since air tends to exert pressure in all directions of the cavity due to its free moving molecules, it expands the antenna volume by pushing the interior wall of the PDMS. This process inflates the antenna and causes the metal patch to bend outward until the pressure has achieved equilibrium with the atmospheric pressure. Increase in antenna volume causes the resonant frequency to decrease, as can be observed in Figure 4.7 (d). By applying a high ambient pressure (>0 bar), on the other hand, the internal air pressure is now lower than the ambient pressure, causing the antenna structure to get compressed. In this case, the resonant frequency increases. To show the importance of the air cavity, simulation has been conducted by filling up the air cavity with the PDMS material, as shown in Figure 4.8 (c) and (d), forming a similar antenna structure without any air cavity. With reference to Figure 4.8 (c) and (d), no obvious deformation/displacement is seen in the antenna structures when the external pressure is varied. The overall structure remains rigid due to the near incompressibility of both the PDMS and EGaIn. It shows that the existence of the air cavity is important, and it has made the structural deformation possible. The importance of incorporating air cavity can also be explained using kinetic theory of gases. This theory describes a gas as a huge number of particles (atoms or molecules) moving in rapid, constant, and random motion. The randomness is caused by the impacts of the particles with each other and with the walls of the cavity. Hence, in our proposed antenna, the air in the cavity exerts a

magnitude of pressure on the walls of the PDMS cavity. In the experiment, the air cavity is filled with the similar pressure as the atmospheric pressure. When there is a difference in the two air pressures, the imbalance changes the volume of the cavity. For example, at low ambient pressure, the air molecules in the cavity exert higher pressure on the walls of the cavity and it causes the volume of the elastic cavity to expand. As a result, the impact of the air molecules on the walls of the cavity reduces. It causes the air pressure to reduce and, eventually, the cavity pressure reaches the same magnitude as the ambient for stabilizing the antenna structure. Changes in pressure and volume of the air cavity can be described using Boyle's law. It states that, as volume increases, the pressure of the gas captured in a closed cavity decreases in proportion, given at a constant temperature. Hence, by changing the pressure, the volume (deformation) of the air cavity changes as well.

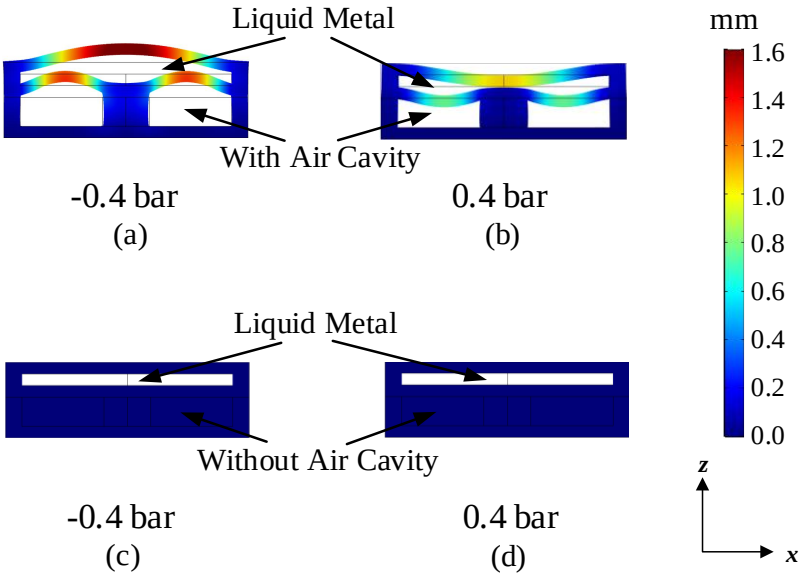

Figure 4.8: Deformation of the liquid patch antenna with an air cavity under (a) low and (b) high ambient pressures. Deformation of a similar liquid patch antenna without an air cavity under (c) low and (d) high ambient pressures.

4.5 Summary

A deformable liquid patch antenna, which is loaded with an air cavity underneath, has been proposed for sensing ambient pressure. Soft, flexible, and deformable elastomer platform has been fabricated using the soft-lithography technique for holding the liquid patch resonator and air cavity. With the use of a supporting PDMS pillar, the patch resonator has been made into one piece, without incorporating meshes of microchannel, for enabling a good antenna gain of 8.02 dBi at 5.806 GHz. Multiphysics analysis has been performed and proven that the air cavity is crucial so that the dual-functional liquid antenna is sensitive to changes in the ambient pressure. Incorporating pressure sensor into an antenna makes a dual-functional wireless device that is able to detect ambient pressure at the same time. The proposed antenna can be useful for applications that require sensing air pressure wirelessly in places such as aircraft cabin, cleanroom, weather monitoring, and crop monitoring (Pook et al., 2012, Chen et al., 2007, Sakthipriya, 2014, Xue-fen et al., 2018).

CHAPTER 5

COMPACT ORGANIC LIQUID DIELECTRIC RESONATOR ANTENNA FOR AIR PRESSURE SENSING USING SOFT MATERIAL

5.1 Introduction

In the previous project, it has been demonstrated that adding air cavity into the antenna design can improve its sensitivity on ambient pressure changes, making a multifunctional antenna that can function both as a sensor and a wireless transmitter. To further prove that this concept can be applied to any antenna, a new antenna design, which is the Liquid Dielectric Resonator Antenna (LDRA) with an air cavity is studied. The addition of an air cavity should improve the LDRA, making it more sensitive to the changes in ambient pressure, and it is able to perform as an air pressure sensor as well. Since the resonating element of LDRA is a liquid dielectric, a new organic liquid is proposed to replace conventional liquid dielectric such as water that has high loss tangent which restricts its performance in high frequency applications. This organic liquid has high dielectric constant and low loss tangent which can be employed to design a compact and high-performance LDRA.

5.2 Dielectric Characterization

It is essential to first know the dielectric characteristics of the liquids before employing them for designing a LDRA. Different types of liquids such

as chloroform, ethyl acetate, acetone, acetonitrile, and deionized water are characterized in the frequency range of 1 – 3 GHz. An open-ended coaxial probe (Lee et al., 2013) has been employed for measuring dielectric constant and loss tangent. The measured dielectric constants and loss tangents are shown in Figure 5.1 (a) and (b), respectively. It can be seen that water has the highest dielectric constant of 72.25 at 2.4 GHz; however, it cannot be used for designing an antenna due to its high loss tangent of ~ 0.13. The dielectric constants of chloroform (ε_r ~ 4.32, tan δ ~ 0.082) and ethyl acetate (ε_r ~ 5.77, tan δ ~ 0.056) are a bit too low for designing a compact LDRA. Acetone (ε_r ~ 20.28, tan δ ~ 0.052) and acetonitrile (ε_r ~ 32.8, tan δ ~ 0.053) have reasonably high dielectric constants and low loss tangents that can be used for designing a compact LDRA to achieve good antenna performances. Since acetonitrile has a higher dielectric constant, it is chosen for designing a compact LDRA for this project. Furthermore, the freezing point of acetonitrile is -45ºC, where this characteristic provides a possibility for the LDRA to work in cold climate areas without the need of adding antifreeze, which is needed for water antenna (Xing et al., 2015). The comparison of different liquid dielectrics is shown in Table 5.1.

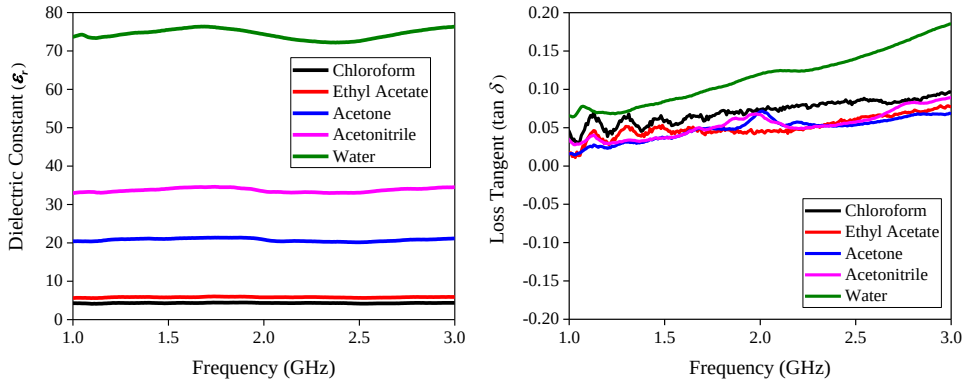

(a) (b)

Figure 5.1: Measured (a) dielectric constants and (b) loss tangents for the five liquid samples.

Table 5.1: Comparison of Different Liquid Dielectrics.

Type of liquid dielectric	Advantages	Disadvantages	Ref
Water (ε_r = 72, tan δ = 0.13)	- Water is cheap and abundant	- High loss tangent and freezing point	(O'Keefe et al., 2007, Wang and Chu, 2019, Jacobsen et al., 2019)
Ethyl acetate (ε_r = 7.1, tan δ = 0.089)	- Liquid with low freezing point	- Dielectric constant is not sufficiently high (<20) - Volatile	(Chen and Wong, 2017b, Chen and Wong, 2017a)
Choline L-alanine (ε_r = 9, tan δ = 0.05)	- Low vapour pressure ionic liquid - Relatively low loss tangent	- Dielectric constant is not sufficiently high (<20)	(Song et al., 2019)
Acetonitrile (εr = 32.8, tan δ = 0.053)	- High dielectric constant (>20) - Relatively low loss tangent	- Volatile organic solvent	**My approach**

5.3 Antenna Configuration and Working Principle

The 3D view of the proposed annular-shaped organic LDRA, as shown in Figure 5.2 (a), is fed by a coaxial probe at an offset distance of C = 8 mm from the center. The LDRA has a diameter of W = 32.4 mm and a height of T = 21.9 mm, with a square copper plate with length of G = 60 mm employed as ground plane. The operating principle of the proposed antenna structure is briefly described here. It is able to function as an air pressure sensor to detect low pressure condition (<0 bar gauge pressure), as can be seen in Figure 5.2 (b). When the ambient pressure reduces, air that is contained in the air cavity

expands and it deforms the liquid reservoir's structure, resulting in a change in the antenna volume, and it shifts the resonant frequency of the LDRA.

All of the simulations are done using the CST Microwave Studio. The design procedure starts from a cylindrical DRA with a diameter of D_{outer} and a height of H, which is mounted on a ground plane, and the resonant frequency (f) of its $HEM_{11\delta}$ mode (Long et al., 1983) can be calculated by equation (2.4).

By using equation (2.4), the $HEM_{11\delta}$ mode of a cylindrical DRA with diameter of D_{outer} = 24.4 mm, height of H = 17.9 mm, and ε_r = 32.8 is calculated to be 1.656 GHz (simulation: 1.616 GHz). In fact, the annular DRA is also able to be calculated using equation (2.4) for its $HEM_{11\delta}$ mode (Luk, 2003). Since the central portion is removed from the dielectric resonator, the actual resonant frequency of an annular DRA is usually higher than that of the cylindrical DRA. In our design, the liquid part of the LDRA is intended to be designed in an annular shape with a height of H = 17.9 mm, outer diameter of D_{outer} = 24.4 mm, inner diameter of D_{inner} = 12 mm, and a relative dielectric constant of ε_r = 32.8.

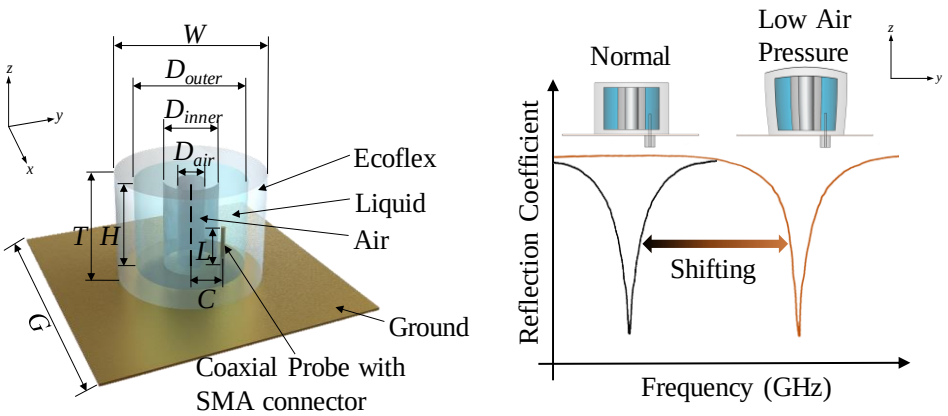

(a) (b)

Figure 5.2: (a) 3D view of the proposed LDRA (b) The effect of changing external air pressure on its resonant frequency.

Without including the Ecoflex, the simulated frequency of the liquid part is found to be 1.868 GHz. Then, the Ecoflex soft material is used to construct a container for holding the liquid, shifting the resonant frequency to 2.398 GHz. After removing the central portion of the Ecoflex to form the air cavity (D_{air} = 6 mm), the frequency will then shift to 2.402 GHz due to the decrease in dimension. It will be shown that the air cavity at the center can be used for air pressure sensing, which will be discussed in the later part. Finally, the impedance matching of the LDRA can be further improved by adjusting the length of the probe (L = 8 mm). As can be justified from the simulated resonant electric and magnetic field distributions shown in Figure 5.3 (a) and (b), respectively, the proposed LDRA is excited in its fundamental $HEM_{11\delta}$ mode (Guha et al., 2011, O'Keefe et al., 2002).

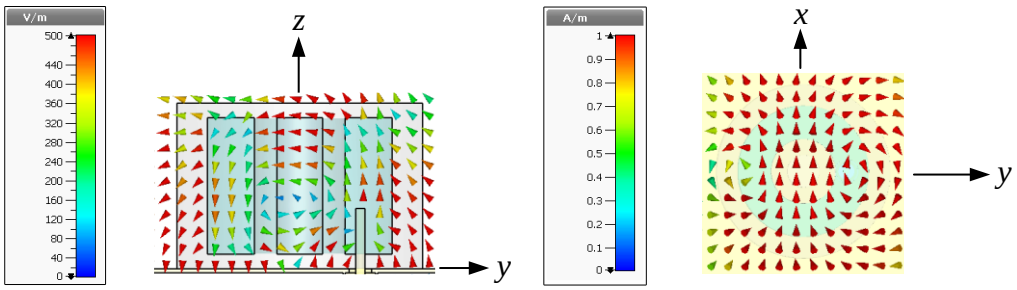

(a) (b)

Figure 5.3: Distributions of the simulated (a) electric fields and (b) magnetic fields of the LDRA at 2.4 GHz.

5.4 Fabrication Process

Figure 5.4 shows the fabrication processes of the proposed LDRA. It is started with the fabrication of the flexible container for holding the liquid dielectric, which is made using the soft-lithography technique. First, two plastic

molds were printed with ABS material using a 3D printer (Ultimaker 3, Netherlands), as shown in Figure 5.4 (a). This printer has a stated layer resolution of 20 – 200 μm (with a 400 μm nozzle), with XYZ resolutions of 12.5 μm, 12.5 μm, and 2.5 μm, respectively. The printed molds have good surface uniformity and they are able to produce good replicas (Dahlberg et al., 2018, Kamei et al., 2015). Instead of applying the conventional PDMS (Sylgard 184), which has been commonly employed for fluidic antennas, we are using Ecoflex 0030 (Smooth-on-Inc, USA) (elastic modulus, E = 125 kPa) for making the flexible container. Such material enables a larger degree of stretchability as it has higher elasticity than the PDMS with a mixing ratio of 10:1 (base to crosslinker) (elastic modulus, E = 750 kPa). Here, Ecoflex solution with a mixing ratio 1:1 (resin to hardener) was poured into the molds (see Figure 5.4 (b)) and degassed in a desiccator for 10 minutes to remove trapped air bubbles. Trapped air bubbles in the Ecoflex solution can degrade the mechanical strength of the container significantly. Later, they were left alone for 4 hours at room temperature to cure.

Figure 5.4 (c) depicts the cured Ecoflex container and cover lid, which were carefully disassembled from the plastic molds. The cured container has a liquid reservoir and an air cavity. Cured Ecoflex 0030 has low dielectric constant (2.02) and low loss tangent (0.0508). Then, the liquid reservoir was filled up with acetonitrile (dielectric constant of ε_r = 32.8 at 2.4 GHz, Sigma-Aldrich, USA) to form the LDRA, as shown in Figure 5.4 (d), and the air cavity was filled up with ambient air. The air cavity expands when the external air pressure is decreased, and vice versa, and this feature will be used for sensing

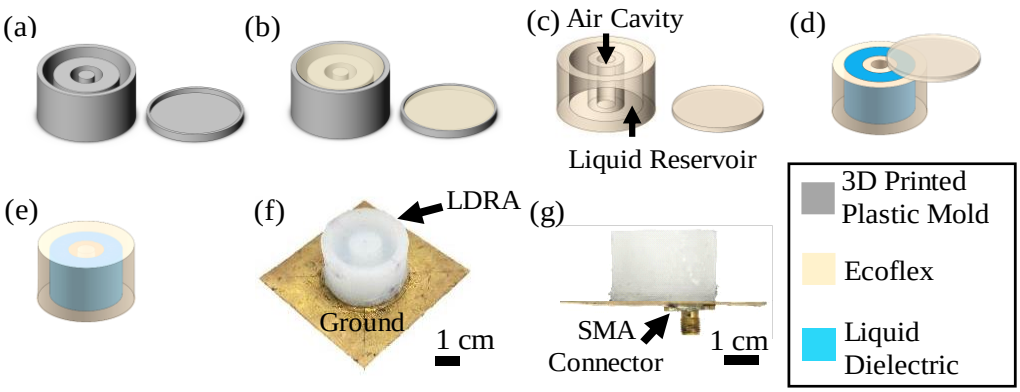

Figure 5.4: The fabricating processes of the LDRA. (a) 3D printed plastic molds. (b) Pouring Ecoflex solution into the molds. (c) Removing Ecoflex container from the molds. (d) Pouring liquid dielectric (acetonitrile) into the Ecoflex container. (e) Sealing up the container. (f) The LDRA is placed on a copper-based ground plane and soldered with an SMA connector. (g) Side view of the completed LDRA.

changes in air pressure. Finally, as can be seen in Figure 5.4 (e), the container was sealed with an Ecoflex-made cover lid using silicon adhesive (Sil-poxy, Smooth-on-Inc, USA). Sealing process is important as it can prevent liquid from leaking and evaporating away. The acetonitrile is volatile at room temperature, and it has a boiling point of 82ºC. In this design, nevertheless, the liquid dielectric is stored in an enclosed cavity and vaporization is negligible. The container, which is made of the soft Ecoflex 0030 silicone elastomer, is also able to offer good chemical (Chart, 2019) and impact resistances (Martinez et al., 2014). Finally, a copper-made ground plane (60 mm × 60 mm) was attached beneath the LDRA using silicon double sided adhesive (Adhesives Research Inc., USA), which was followed by the soldering of a SMA connector to enable the probe feeding (Figure 5.4 (f) and (g)). The connector was then connected to a vector network analyzer (VNA) for further measurements.

5.5 Experiment Results and Discussions

The reflection coefficients and input impedances of the LDRA are shown in Figure 5.5 (a) and (b) respectively, which show reasonable agreement. The dominant $HEM_{11\delta}$ mode is found to be at 2.4 GHz, covering a measured bandwidth of 24.3% (simulated bandwidth: 20.4%). The measured and simulated Q factors are found to be 4.12 and 4.90, respectively. Similar range (3.64 to 10.2) of Q factor is also found in other antennas (Chuang and Chung, 2011, Sun et al., 2015, Zhang et al., 2015). With reference to Figure 5.5 (a), the measured reflection coefficient shows a better matching level than the simulated one because the measured resistance is much closer to 50 Ω (shown in Figure 5.5 (b)). Actually, the difference between the simulated and measured input impedances is quite small. The minor discrepancy may be due to fabrication tolerances.

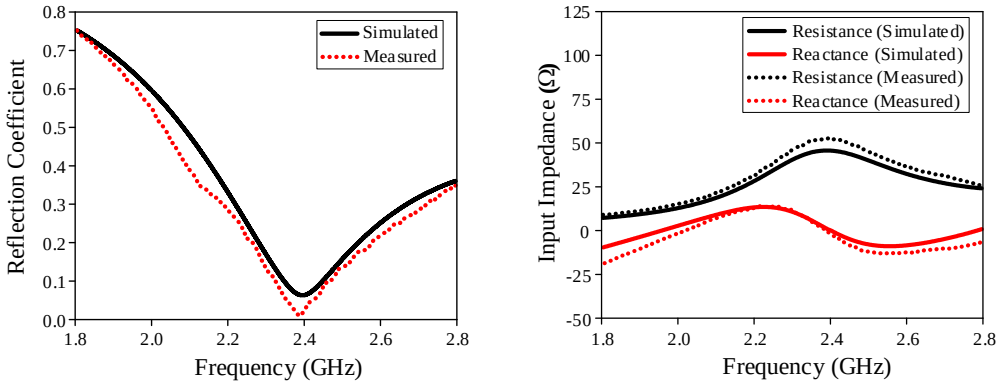

(a) (b)

Figure 5.5: Measured and simulated (a) reflection coefficients and (b) input impedances of the LDRA.

5.5.1 Radiation Characterization

The measured and simulated radiation patterns at the resonant frequency of 2.4 GHz are shown in Figure 5.6 (a) and (b). Broadside radiation patterns are observed, as expected for this mode. High cross-polarization is observed in the *H*-plane (Figure 5.6 (b)) due to the probe-fed mechanism that is employed by this design. Similar effect is also seen in other research papers (Shum and Luk, 1998, Liang et al., 2009). According to the explanation provided in reference (Liang et al., 2009), vertical electric fields introduced by the feeding probe can contribute to the increase of cross-polarization.

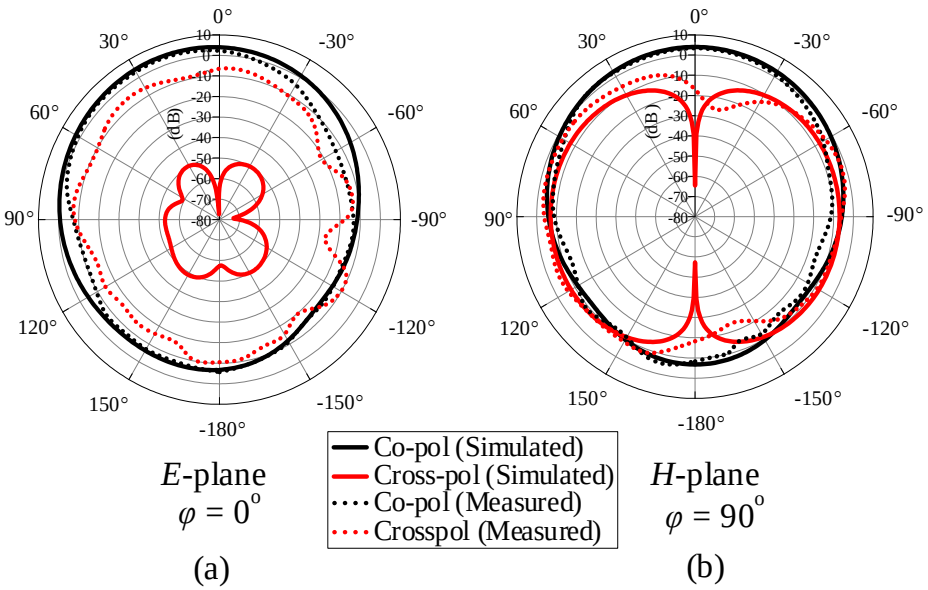

Figure 5.6: Measured and simulated radiation patterns of the LDRA in the (a) *E*- and (b) *H*-planes at 2.4 GHz.

A similar LDRA is also constructed using deionized water in the same frequency range for comparison purpose. The antenna gains of the water and acetonitrile LDRAs are compared in Figure 5.7. In general, the acetonitrile

LDRA has higher antenna gain (~ 2 dB) than the water LDRA. This is because acetonitrile has lower loss than water in this frequency range.

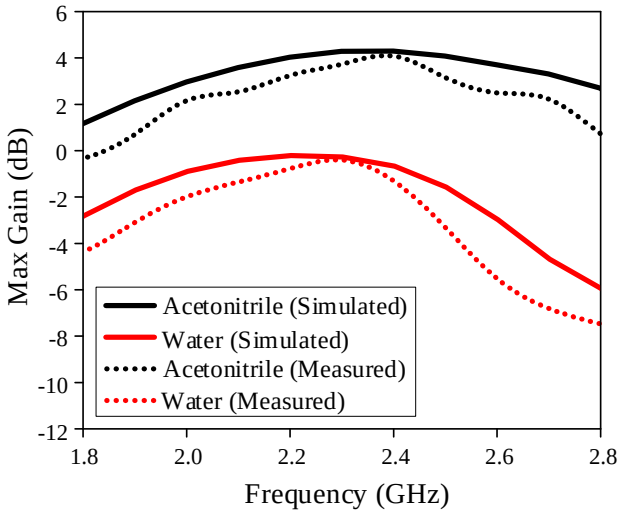

Figure 5.7: Measured and simulated antenna gains of the acetonitrile and water LDRAs.

Antenna efficiencies ($HEM_{11\delta}$ mode) of the proposed LDRA are simulated for the cases with and without including mismatch loss. To have the same antenna volume, all of the dimensions are fixed and only the liquid dielectric is replaced. The results are provided in Table 5.2, along with other important information such as dielectric constant, loss tangent, and resonant frequency. It can be seen that the antenna efficiency is inversely proportional with the loss tangent. Water has the highest loss tangent (0.130), as a result, it has the poorest antenna efficiency. Most others are able to go beyond 70%. The lower the loss tangent of a liquid dielectric, the higher the antenna efficiency is. With reference to the table, the total antenna efficiency (including impedance mismatch loss) of the proposed LDRA at 2.4 GHz, which is made of acetonitrile, is 72.04%. Although the resonant frequency of the $HEM_{11\delta}$ mode shifts when a different liquid dielectric is used for designing the LDRA, its radiation

characteristics such as electric and magnetic field distributions as well as the corresponding radiation patterns are maintaining the same.

Table 5.2: Comparison of LDRAs Made of Different Liquid Dielectrics (all are made with the same dimension).

Liquid Dielectric	Dielectric Constant, ε_r	Loss Tangent, tan δ	Resonant Frequency of $HEM_{11\delta}$ (GHz)	Radiation Efficiency excluding Impedance Mismatch Loss (%)	Total Efficiency including Impedance Mismatch Loss (%)
Water	72.25	0.130	1.71	29.37	29.02
Acetonitrile	32.80	0.053	2.40	72.33	72.04
Acetone	20.28	0.052	2.89	74.08	74.06
Ethyl acetate	5.77	0.056	4.42	72.11	72.06
Chloroform	4.32	0.082	4.72	70.78	68.94

5.5.2 Air Pressure Sensing

Experimental setup for changing the ambient pressure is shown in Figure 5.8 (a), where a vacuum pump and a pressure gauge are engaged for controlling the air pressure in a pressure chamber. The pressure in context refers to the gauge pressure which is zero-referenced against ambient pressure. Figure 5.8 (b) depicts that the antenna's resonant frequency increases linearly when the ambient pressure is reduced. Different placement angles have been studied and a comparison is shown in Figure 5.8 (b). Placement angle of 0^o shows the highest sensitivity (270 MHz/bar). The sensitivity decreases as the tilting angle is increased until it is reaching zero response at 70^o. This is because the liquid in the reservoir can produce different forces on the walls of the air cavity at a different placement angle due to the influence of gravity. This feature can be employed for sensing the ambient pressure surrounding the LDRA. The effect

of the altitude (level above the sea level) of the sensor is minimal, according to equation (5.1), where P is the atmospheric pressure at a given altitude of h (Cavcar, 2000). This effect can be eliminated through calibration when a new measurement is performed. Ambient factor such like temperature can also affect the pressure sensing mechanism, but it can also be easily removed through proper calibration. The air pressure responses will be simulated using multi-physical simulation software and analyzed shortly. Due to the limitation of our pressure chamber, experiment on increasing air pressure cannot be done.

$$P\ (bar) = 1.01325(1 - 2.25577 \times 10^{-5} \times h)^{5.25588} \qquad (5.1)$$

Shape deformation of the proposed acetonitrile LDRA is also simulated and analyzed using the COMSOL Multiphysics software. It is studied for the surrounding ambient pressures of -0.8 bar and 0.8 bar. Figure 5.9 (a) and (b) show the deformation of the acetonitrile LDRA with an air cavity when it is placed in ambient pressure of -0.8 bar and 0.8 bar, respectively. By filling up the air cavity with Ecoflex forming a LDRA without any air cavity, the

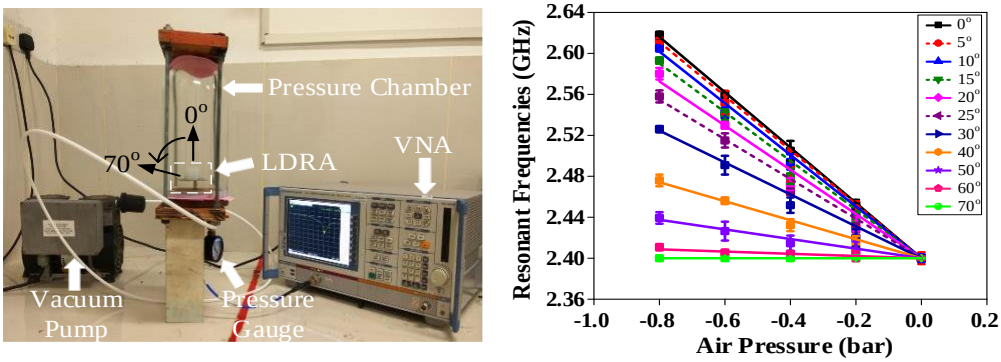

(a) (b)

Figure 5.8: (a) Experimental setup for sensing changes in air pressure. (b) Resonant frequencies of the LDRA as a function of air pressure change at different placement angles.

corresponding deformed shapes are also shown in Figure 5.9 (c) and (d) for the two similar pressures. All of the displacements are shown in the same scale at all points on the surfaces. With reference to Figure 5.9 (a) and (b), for the LDRA with an air cavity, obvious changes in displacement are observed in the horizontal and vertical directions. At the normal ambient pressure (0 bar), external pressure exerting on the surfaces of the LDRA (with air cavity) is balanced out by the internal air pressure inside the air cavity. When there is a reduction of ambient pressure (<0 bar), the internal air pressure becomes higher than the surrounding. Since air tends to exert pressure in all directions of the cavity due to its free moving molecules, it pushes the interior wall of the Ecoflex and expands the air cavity. This process inflates the air cavity and causes the liquid dielectric to bend outward until the pressure has achieved equilibrium with the atmospheric pressure. Increase in the air cavity's volume causes the resonant frequency to increase, as can be observed in Figure 5.8 (b), due to the

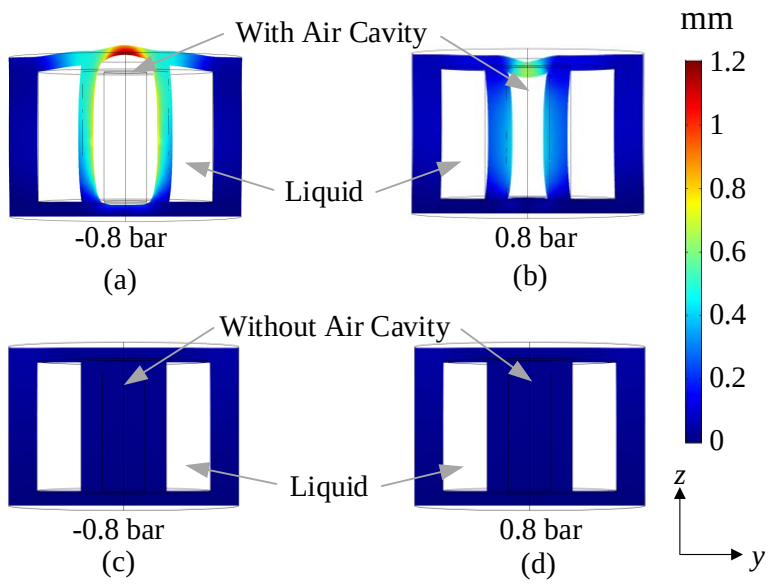

Figure 5.9: Simulated shape deformation of the acetonitrile LDRA with an air cavity under a surrounding ambient pressure of (a) -0.8 bar and (b) 0.8 bar; Simulated shape deformation of the acetonitrile LDRA without an air cavity under a surrounding ambient pressure of (c) -0.8 bar and (d) 0.8 bar.

decrease in the effective dielectric constant of the antenna. For high ambient pressure (> 0 bar), on the other hand, the internal air pressure is lower than the surrounding ambient pressure, causing the whole structure to get compressed.

Without having an air cavity inside the LDRA, as can be seen in Figure 5.9 (c) and (d), the antenna structures are unable to deform when the external pressure is varied. The overall structure remains unchanged due to the near incompressibility of both Ecoflex and acetonitrile. It is obvious that the existence of the air cavity makes the pressure sensitivity of the structure much higher. The antenna can now function as both the radiating element and the air pressure sensor, reducing the need for multiple commercial electronic components.

5.6 Summary

For the first time, a dual-functional annular LDRA has been proposed for sensing ambient pressure. Organic liquid dielectric with high permittivity and low loss has been successfully employed for designing a compact and efficient LDRA. A soft, flexible, and deformable elastomer platform has been fabricated using soft-lithography technique for holding the liquid dielectric. The central air cavity of the annular DRA has been again proven to be crucial so that the antenna structure is sensitive to changes in the ambient pressure. It has been shown that the antenna gain of the proposed acetonitrile LDRA is at least 2 dB higher than that of the water LDRA in the frequency range of 1.8 GHz – 2.8 GHz. The air pressure sensing feature of the proposed LDRA is sensitive

enough (270 MHz/bar) to detect any changes in the ambient pressure. The proposed LDRA can be applied for detecting air pressure in sensitive environments such as airplane cabin, weather monitoring, and crop monitoring, where the data can be transferred wirelessly (Sakthipriya, 2014, Xue-fen et al., 2018).

CHAPTER 6

LIQUID ELECTROMAGNETIC BANDGAP FOR STRETCHABLE AND WEARABLE SLOT ANTENNA

6.1 Introduction

From the previous projects, it has been proven that the stretchable antennas can also be used as wireless strain sensors as their electrical properties can alter with the change in the geometry. Of course, a single stretchable antenna that can function as both as a physical quantity sensing device and a communication device is also very welcome as a wearable device on human body. However, the ground planes used in the previous designs are made of rigid copper, which do not conform to human skin. Also, the human body tends to detune the antenna and absorb large amount of radiation power. Therefore, a multi-functional antenna structure that is able to isolate the effect of human body is much needed. In this project, a stretchable EBG that is made of elastomer and liquid metal is fabricated using the microfluidic approach. This is to realize a multifunctional wearable antenna that can be used for biomedical applications.

6.2 Antenna Design

The wearable antenna involves two parts designs: antenna and EBG. Design and analysis of the antenna and the EBG structure are carried out using the CST Microwave Studio software for full-wave electromagnetic simulation.

6.2.1 Antenna Configuration

Figure 6.1 (a) shows the isolated liquid slot antenna structure. It consists of a conductive liquid (EGaIn) that is being encapsulated inside a soft Ecoflex 0030 (Smooth-on-Inc, USA) substrate, which has a dielectric constant and loss tangent of 2.6 and 0.02, respectively. The dielectric characteristics are measured using the open-ended coaxial probe method (Lee et al., 2013). The encapsulated conductive liquid is infused into the substrate's cavity through injection, and it has a conductivity of 3.4×10^6 S/m. With reference to Figure 6.1 (a), the antenna is excited by a 50 Ω SMA connector whose inner conductor is immersed inside cavity that forms the central conductor of a short segment of coplanar waveguide, which also has a characteristic impedance of 50 Ω. The LEBG unit cell, as shown in Figure 6.1 (b), which is also made of conductive liquid, comprises a top square loop and a bottom ground patch (hidden structure shown in dotted contour). Each side of the patch is loaded with a short stub, which will be translated into an inter-connecting bridge when unit cell is extended into an array. The ground plane is designed to have narrow bridges inter-connecting the adjacent unit cells for reducing the wobbly effect of the dense liquid metal. It should be mentioned that no via is involved in this structure. This is very crucial

as it is very difficult to make a via in the flexible liquid structure. Six LEBG elements are then cascaded to form a 3×2 array, and it is placed underneath the slot antenna, as shown in Figure 6.1 (c), to form the proposed wearable antenna. The proposed antenna with the final optimized parameters working at 3.437 GHz are shown in Table 6.1. It has a compact footprint of 33 mm (W) × 69.5 mm (L).

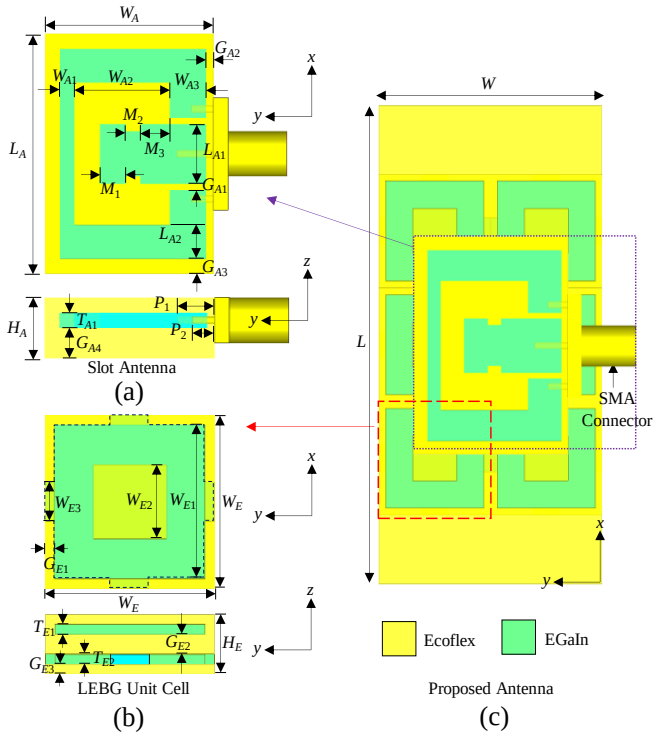

Figure 6.1: Configurations of the (a) liquid slot antenna, (b) liquid EBG unit cell, and (c) the proposed liquid slot antenna with liquid EBG structure.

Table 6.1: Design Parameters of The Proposed Liquid Antenna.

Parameters	Value (mm)	Parameters	Value (mm)	Parameters	Value (mm)
W	33.0	P_1	5.0	H_E	6.0
L	69.5	P_2	3.0	W_E	16.5
W_A	23.0	G_{A1}	0.8	W_{E1}	14.5
L_A	32.0	G_{A2}	1.0	W_{E2}	6.5
H_A	8.0	G_{A3}	2.0	W_{E3}	4.0
W_{A1}	2.0	G_{A4}	4.0	G_{E1}	1.0
W_{A2}	13.0	M_1	3.5	G_{E2}	2.0
W_{A3}	5.0	M_2	2.0	G_{E3}	1.0
L_{A1}	8.0	M_3	4.0	T_{E1}	1.0
L_{A2}	4.5	T_{A1}	2.0	T_{E2}	1.0

6.2.2 EBG Structure

The typical mushroom-shaped EBG structure cannot be used for fluidic circuits due to the existence of the vias. To ease the integration with liquid antenna, a via-less EBG structure has been proposed in this paper. Figure 6.2 shows the simulation settings of the unit cell for studying the reflection phase of the LEBG. The unit cell's boundary conditions are set as "unit cell" in both the *x*- and *y*-directions. Port 1 is then configured to propagate a linearly polarized plane wave in the *z*-direction (de-embedded with a distance of 50 mm from the surface of unit cell). After the simulation is completed, the top surface of the LEBG unit cell is set as the reference plane. Figure 6.3 (a) shows the proposed via-less LEBG's equivalent circuit model with a top-loading square loop (Langley and Parker, 1982, Amjadi and Soleimani, 2006). The total surface impedance of the equivalent circuit can be expressed as:

$$Z_0(\omega) = Z_1(\omega)//Z_2(\omega) = j\omega L_1 \frac{1-\omega^2 C_2 L_2}{1-\omega^2(L_2 + L_1)C_2} \tag{6.1}$$

From equation (6.1), the resonant frequency (*f*) of the structure can be calculated as (Amjadi and Soleimani, 2006):

$$f = \frac{1}{2\pi\sqrt{(L_1 + L_2)C_2}} \tag{6.2}$$

where L_1, L_2, C_1 are the inductance between loop and ground plane, unit inductance, and capacitance between units, respectively. These values can be

calculated by the equations found in (Yang and Rahmat-Samii, 2009, Ashyap et al., 2018, Holloway and Kuester, 1998).

To lower the operating frequency of the LEBG structure, a top-loading square loop is used instead of square patch, although both do not require the use of vias. Figure 6.3 (b) shows the comparison of the reflection phases for both cases, which are obtained from the unit cell simulations. It is observed that the top-loading loop has a lower operating frequency than the top-loading patch. This is because etching the center of the patch with a square hole to form a loop makes it functions more like an inductive wire, rather than a traditional patch that behaves as a capacitive surface with the ground plane. The square loop appears to remain unchanged to the equivalent capacitance C_2 between adjacent unit cells, however, both the equivalent inductances L_1 (formed in the square loop) and L_2 (between the square loop and the ground) increase, therefore

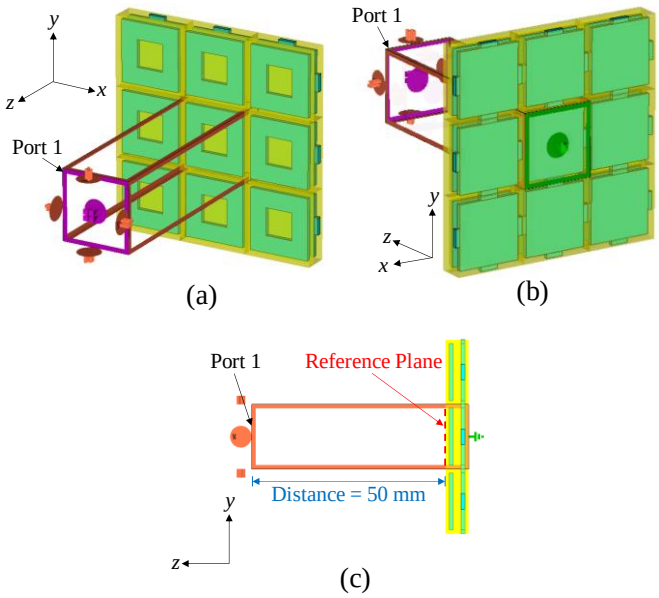

Figure 6.2: 3D view with (a) top and (b) bottom view visible, and (c) side view of the simulation setup of the liquid EBG.

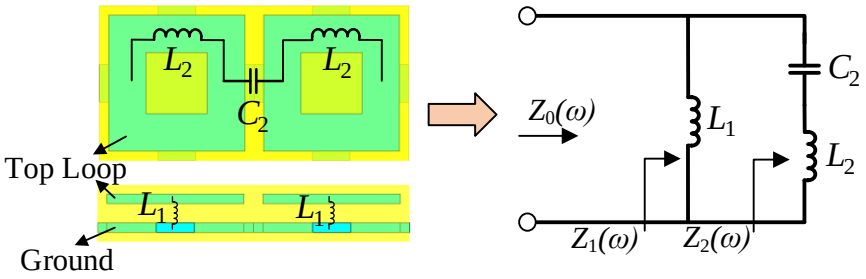

(a)

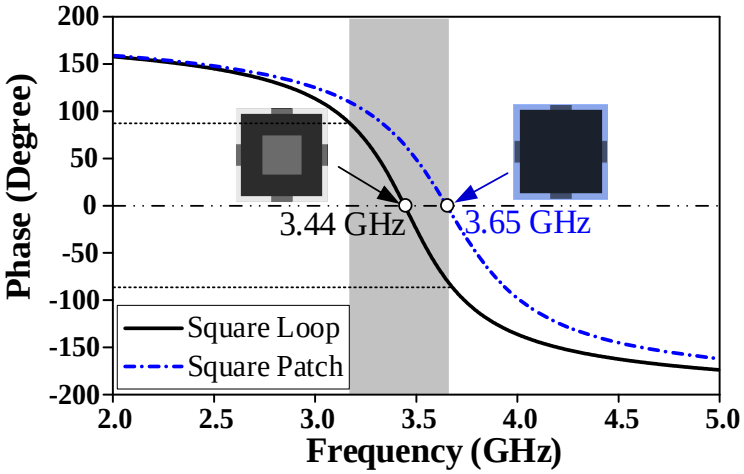

(b)

Figure 6.3:(a) Equivalent circuit of the square loop LEBG. (b) Comparison of reflection phases of the proposed square loop LEBG and conventional square patch EBG. The greyed region and black dotted lines signify the ±90º bandwidth for proposed square loop LEBG.

reducing the operating frequency of the structure. The proposed square loop LEBG is designed to have a zero reflection phase frequency point at 3.44 GHz. Figure 6.4 shows the surface current distribution of the proposed antenna at 3.437 GHz. As the proposed antenna's resonant frequency falls within the operation range of the LEBG, the surface currents flowing in the vertical direction of the LEBG flow in the same direction as those on the antenna (outer loop), as can be seen in the figure, which has in turn improved the antenna's radiation performance.

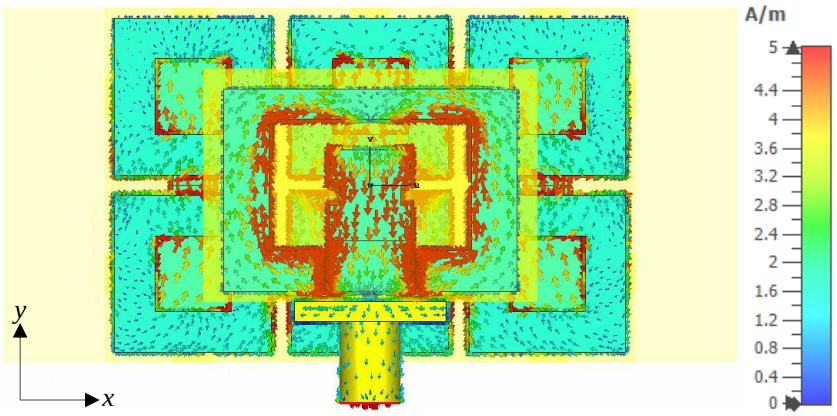

Figure 6.4: Surface current distributions of the proposed antenna and LEBG at 3.437 GHz. The arrows indicate the direction of the surface current, and the colour indicates the intensity of the surface current distributions.

6.2.3 Effect of LEBG Array

It is impractical to design a huge EBG array for the wearable antenna. Here, the LEBG element is translated into a small and finite array and the effects are studied. In Figure 6.5, the reflection coefficients of the liquid slot antenna with the backing LEBG array of 3×2, 3×3, and 4×3 number are studied, where the frequency is found to fluctuate in the range of 3.3 – 3.4 GHz. The 3D radiation patterns at the respective resonant frequencies are shown in Figure 6.6. For all cases, the corresponding antenna gains in the boresight are found to be in the range of 5.45 – 5.96 dBi. At the end, the 3×2 LEBG array is selected because it has the smallest size and the largest gain. This is an optimum design point because the resonant frequency of the slot antenna has the closest operating frequency with the LEBG 0º reflection phase of the 3×2 array.

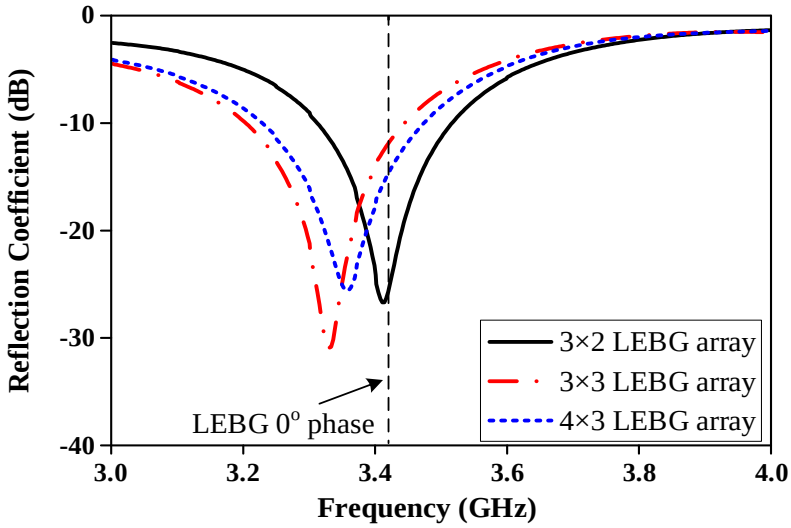

Figure 6.5: Simulated reflection coefficients of the proposed wearable antenna backed with different number of LEBG arrays. The LEBG 0º phase frequency is indicated as black dashed line.

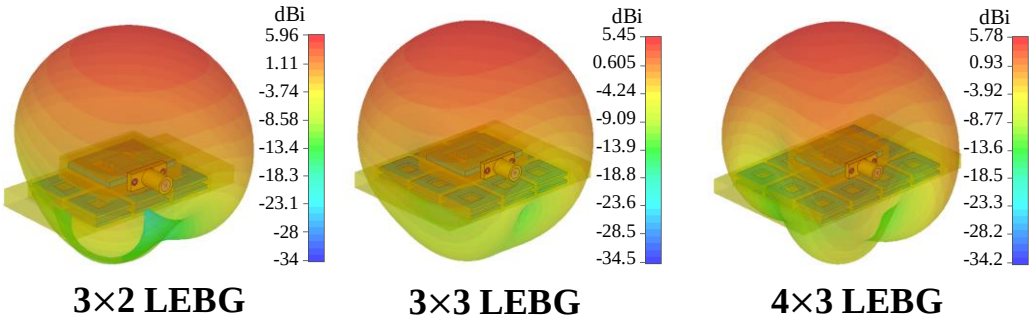

Figure 6.6: Radiation patterns of the proposed wearable antenna backed by different number of LEBG arrays at their respective resonant frequencies.

6.3 Fabrication Processes

Figure 6.7 shows the fabrication processes of the slot antenna and LEBG. It is started with the fabrication of the slot antenna, which is made using the soft-lithography technique, as shown in Figure 6.7 (a)-(c) (Xia and Whitesides, 1998). This fabrication method allows for rapid prototyping of new antenna design. The single "master" can be repeatedly used for replicating many identical antennas. To ease the fabrication, the Ecoflex container was split into

2 different layers (highlighted in dotted red line), all of which were separately made, and they were sealed together at the end. First, two plastic molds were printed using a 3D printer (Ultimaker 3, Netherlands). Next, an Ecoflex prepolymer solution with a mixing ratio 1:1 (resin to hardener) was poured into the molds and degassed in a desiccator for 10 minutes to remove trapped air bubbles. Trapped air bubbles in the Ecoflex solution could affect its dielectric properties, which could affect the antenna's resonant frequency. Later, they were left alone for 4 hours at room temperature to cure. An SMA connector was poked into the base layer before sealing it with the cover lid using silicon adhesive (Sil-Poxy, Smooth-On, USA). The formed cavity is then filled with

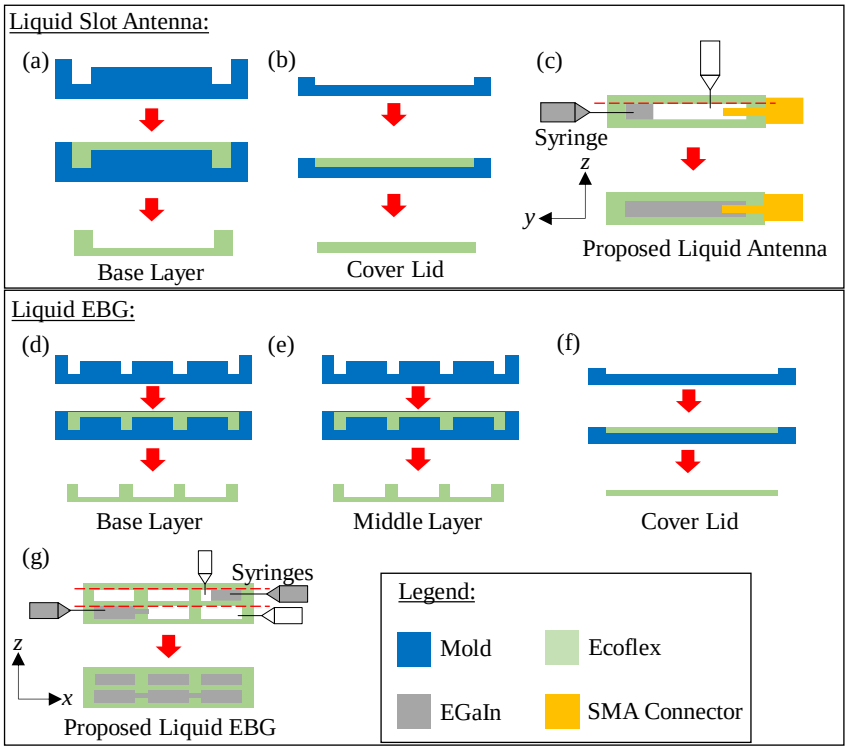

Figure 6.7: Fabrication processes of the liquid slot antenna and LEBG. Filling and curing of Ecoflex for the (a) base layer and (b) cover lid of antenna. (c) Bonding the two Ecoflex layers together before injecting the EGaIn into the cavity to form a liquid slot antenna. Filling and curing of Ecoflex for the (d) base layer, (e) middle layer, and (f) cover lid of LEBG. (g) Bonding the three Ecoflex layers together before injecting the EGaIn into the cavities to form a LEBG.

EGaIn using two syringes - One for injecting the liquid metal and the other for withdrawing the trapped air in the cavity, as shown in Figure 6.7 (c). The injected holes were finally sealed to prevent leakage. Similar technique was used in the fabrication processes of the LEBG as shown in Figure 6.7 (d)-(g). Finally, the completed prototype is shown in Figure 6.8.

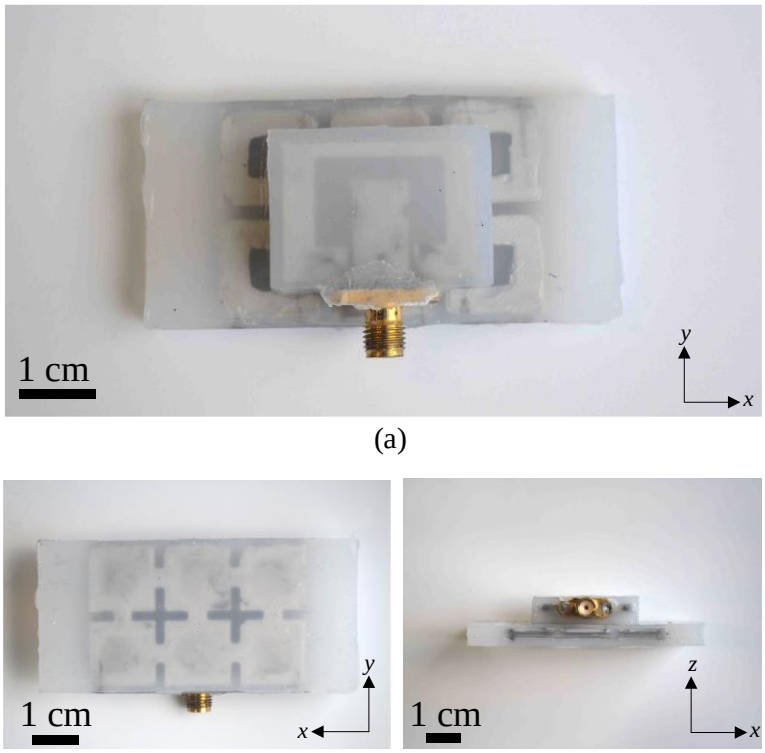

Figure 6.8: Fabricated prototype of the proposed LEBG-backed antenna at (a) top view, (b) bottom view, and (c) side view.

6.4 Experiment Results and Discussion

6.4.1 S_{11} Parameter

The CST Microwave Studio was used to simulate the proposed antenna, and measurements were carried out using a Rohde & Schwarz VNA. Measured

and simulated reflection coefficients of the antenna with/without LEBG are shown in Figure 6.9, where the corresponding input impedances are shown in Figure 6.10 (a) and (b), showing reasonable agreement. For the antenna without LEBG, the simulated and measured resonant frequencies are 2.993 GHz and 3.020 GHz, respectively, with an error of 0.9%. The corresponding simulated and measured impedance bandwidths are 10.79% and 8.34%. The operating frequency band of the antenna shifted up when the LEBG array is added. The simulated and measured resonant frequencies are 3.437 GHz and 3.401 GHz, respectively, which can cover the desired sub-6GHz of 5G (3300-3600 MHz) bands (Liu et al., 2018). After the antenna is loaded with the LEBG layer, it can be observed that the impedance matching level improves. In this case, the simulated and measured impedance bandwidths are 6.14% and 10.27%, respectively.

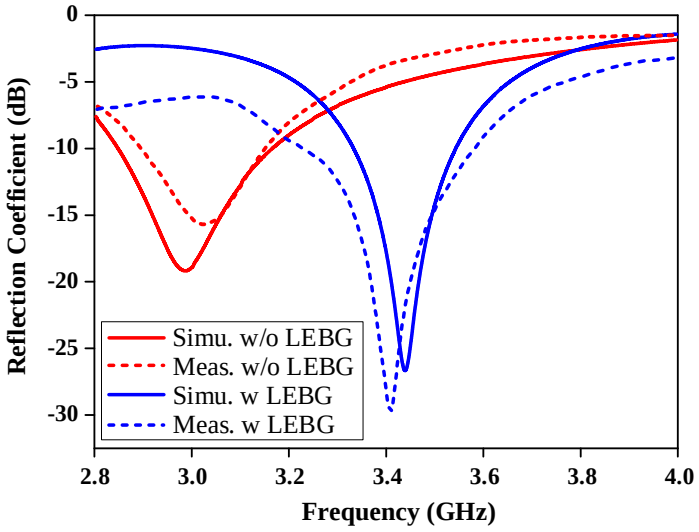

Figure 6.9: Reflection coefficients of the proposed antenna with/without LEBG.

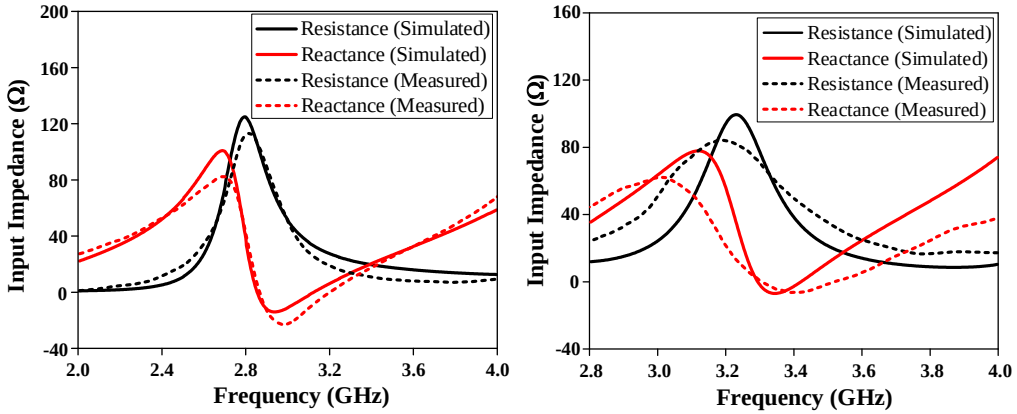

Figure 6.10: Simulated and measured input impedances of the proposed antenna for the cases (a) without LEBG and (b) with LEBG.

6.4.2 Radiation Patterns and Antenna Gains

Figure 6.11 (a)-(c) show the simulated and measured radiation patterns of the proposed antenna for the cases with and without being loaded with the LEBG at their resonant frequencies for 3 different planes. Reasonable agreement is observed between the findings of simulation and measurement. For the case without LEBG, it is obvious that the liquid slot antenna alone has a bi-directional pattern. Backing the antenna with the LEBG has truncated the radiation in the direction of θ = 180º, as shown in the *xz*- and *yz*-planes, making it a unidirectional antenna. The bandgap structure has improved the boresight (θ = 0º) field strength significantly. Also, can be observed from Figure 6.11 (a) and (b), the antenna without LEBG has a measured maximum antenna gain of 2.24 dB (simulated gain: 2.35 dB) at 3.020 GHz in the boresight. The measured gain is enhanced to 5.80 dB (simulated gain: 5.96 dB) after incorporating the LEBG layer. Whereas in the *xy*-plane, as shown in Figure 6.11 (c), the effect of adding LEBG is not as significant as in the other two planes, this is because the antenna is mostly radiating in the ± *z* direction.

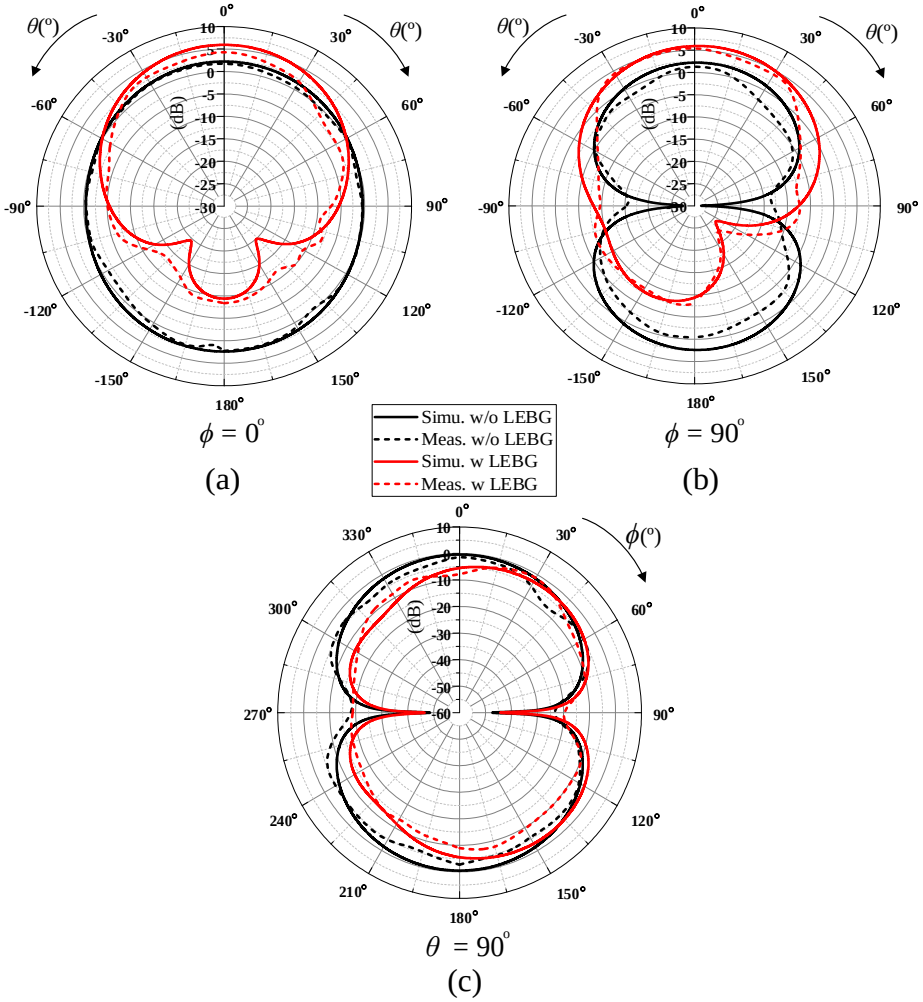

Figure 6.11: Simulated and measured radiation patterns of the proposed antenna with/without LEBG for (a) *xz*-plane, (b) *yz*-plane, and (c) *xy*-plane.

6.4.3 The Effects of Human Body on the S_{11} Parameter

The antenna is put on various areas of human body as well as an artificial skin (phantom) to investigate the effects of human body. Figure 6.12 (a) and (b) show the S_{11} curves of the antenna, with and without LEBG, respectively, in free space and on human body conditions. The curves in Figure 6.12 (a) have slight differences with the bandwidths of S_{11} < -10 dB cover the sub-6GHz of 5G band in all conditions. However, in Figure 6.12 (b), we can see that the S_{11} curves for antenna without LEBG shift largely. Hence, this shows that the LEBG is isolating the effect of human skin on its impedance matching.

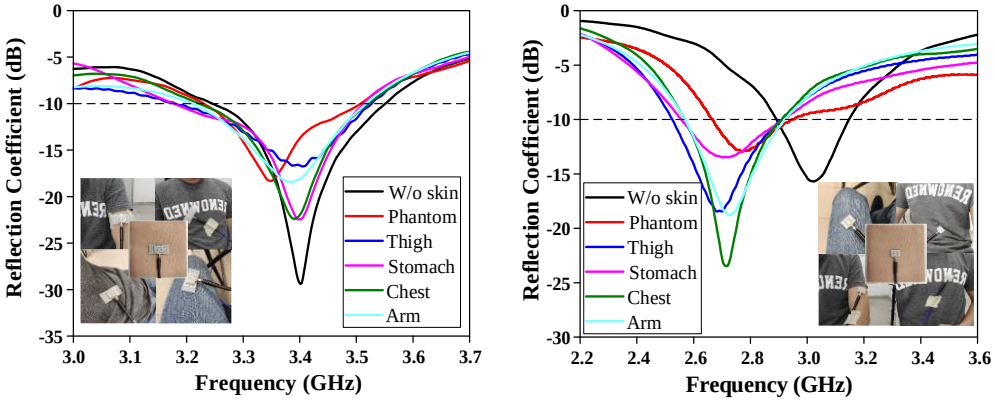

Figure 6.12: Measured S_{11} for the proposed antenna placed on different parts of human body for the cases (a) with LEBG and (b) without LEBG. Inset shows the measurement setup.

6.4.4 SAR Evaluation

SAR is an important metric for determining if a wearable antenna is suitable on human body in practical. To ensure that the proposed LEBG-backed slot antenna can be used on human without harm, simulations of the SAR values were performed. A cuboid-shaped multilayer human tissue model with a dimension of 100×100×40 mm^3 was employed to mimic the human body, which consists of four layers, each representing skin, fat, muscle, and bone (Gao et al., 2018). The respective electromagnetic parameters are listed in Table 6.2 (Jiang et al., 2014). The distance between the model and the antenna (with/without the LEBG surface) is 1 mm. The SAR levels were simulated using the CST Microwave Studio with a benchmark of 0.1 W input power by referring to the IEEE/IEC 62704-1 standard.

Figure 6.13 (a) and (b) show the antenna's SAR value without the LEBG. The standards of 1 g and 10 g are used for the calculation of SAR value. By referring to the same figures, the center of the antenna has the most radiation.

The 1 g standard result shows the maximum SAR value of 4.89 W/kg, which is higher than the US limit of 1.6 W/kg. For the 10 g standard, the highest SAR value is 2.31 W/kg, exceeding the European limit of 2.0 W/kg as well.

Figure 6.13 (c) and (d) show that, after adding the LEBG to the antenna, the central area of the antenna shows weaker radiation, and the power is dispersed into a larger area around the unit cells. From the same figure, the maximum SAR value for 1 g and 10 g standards are 1.25 W/kg and 0.454 W/kg, respectively. This gives a reduction of 74.4% and 80.3% in SAR for 1 g and 10 g, respectively, when compared to the antenna without LEBG. The amount of absorbed radiation in the human model is reduced to a bare minimum. The comparison of the antenna with and without LEBG are shown in Table 6.3,

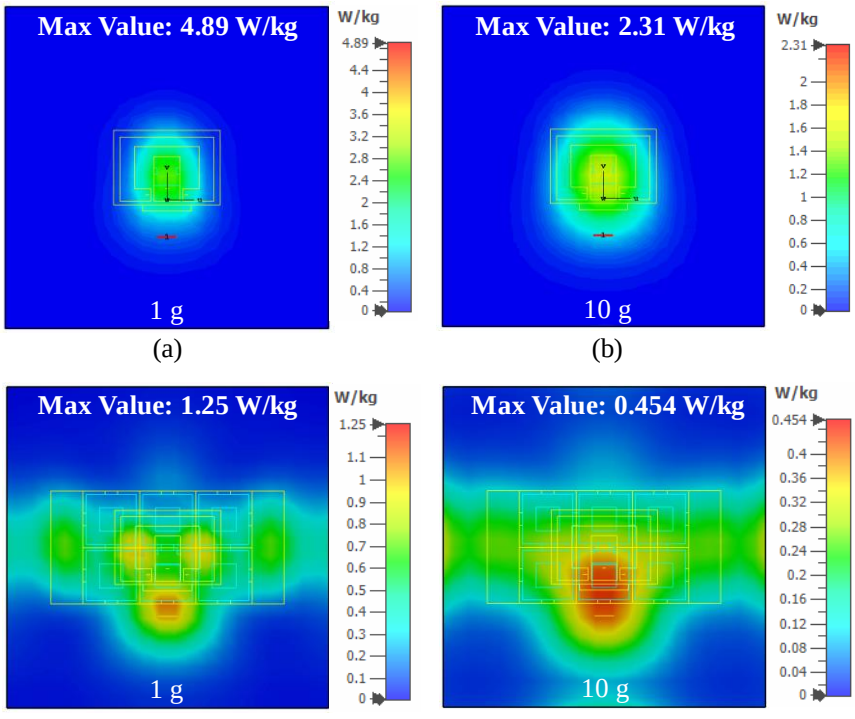

Figure 6.13: Simulated SAR of the proposed antenna without LEBG for (a) 1 g and (b) 10 g standards, respectively. Simulated SAR of the proposed antenna with LEBG for (c) 1 g and (d) 10 g standards, respectively.

indicating the proposed antenna is capable of SAR reduction to fulfil for both the US and Europe standards.

Table 6.2: Material Properties of the Human Body Model.

	Skin	Fat	Muscle	Bone
$\boldsymbol{\varepsilon_r}$	37.95	5.27	52.67	18.49
$\boldsymbol{\sigma(S/m)}$	1.49	0.11	1.77	0.82
Density (kg/m^3)	1001	900	1006	1008
Thickness (mm)	2	5	20	13

Table 6.3: SAR Values of The Antennas (unit: W/kg).

	With LEBG	Without LEBG	Max Value
1 g standard (US)	1.25	4.89	1.6
10 g standard (EUR)	0.454	2.31	2.0

6.4.5 Bending Test

Wearable antennas are also expected to be bent to uneven human body surfaces. To study the stability of the resonant frequency of the wearable antenna when it is bent, experiment is conducted on the proposed LEBG-backed slot antenna under different degrees of structural deformations. The experiments were done (in free space) using polystyrene cylinders with different diameters (D = 76, 102, 127 mm), which were chosen based on typical sizes of average human arm, thigh, and chest, respectively (Ashyap et al., 2018, Raad et al., 2012). Adhesive tape is used to attach the antenna on the polystyrene cylinders. Since the length of the antenna is twice of the width, it is more likely to be bent along its *y*-axis in practical scenario. Hence, the respective reflection coefficients being bent along the antenna's *y*-axis on the three different cylinders are shown in Figure 6.14. The measured reflection coefficients have

slightly or negligible shift in frequency. The impedance bandwidth ($|S_{11}|$ < -10 dB) is very stable, and it can cover the desired frequency band (3300−3600 MHz). It implies that the proposed antenna is stable under different bending conditions.

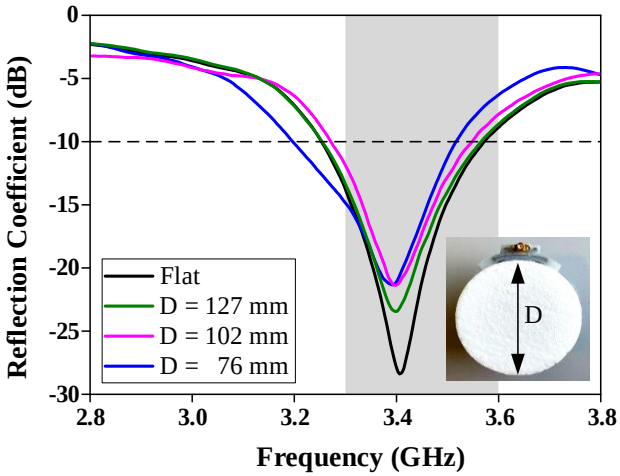

Figure 6.14: Measured $|S_{11}|$ of the proposed LEBG-backed antenna under different bending conditions. The greyed region represents the sub-6GHz passband (3300-3600 MHz). Inset shows the experimental setup.

6.4.6 Strain Sensing

Since the antenna and the LEBG are both made of elastomer and liquid metal, the resulted antenna structure is fully stretchable. This feature is important as the antenna is most likely to stretch when it is applied on human body. Since the deformation in the geometry of the liquid metal can vary the electrical properties of the antenna (Wang et al., 2015, Low et al., 2019), the proposed antenna will be elongated in the axial direction (*x*-axis) to study the response in the reflection coefficient. In the experiment, a 3D printed plastic holder was used to clamp the two ends of the LEBG. The acrylonitrile butadiene styrene (ABS) material used for 3D printing has a very minimal effect on the

antenna. The measured reflection coefficients for strains (ε) of $0 - 30\%$ along the axial direction are shown in Figure 6.15 (a), with the experimental setup illustrated in the inset. The proposed antenna was not stretched beyond 30% strain because the average elongation of human skin is about 15.5% (Sugihara et al., 1991). The impedance matching level has been good for all cases. Since the strain is applied on the LEBG, it causes the bandgap structure to elongate more, causing its operating frequency to vary (zero-phase frequency point has shifted away). As a result, the resonant frequency of the LEBG-backed slot antenna shifts up linearly from 3.401 to 3.512 GHz when the strain is increased from 0% to 30%. A line of best fit was plotted and a sensitivity of 3.71 MHz/strain(%) is obtained. With this linear relationship, the proposed antenna is suitable to be a strain sensor for wearable biomedical applications. In Figure 6.15 (b), when the strain returns to zero, the resonant frequency is able to return to its original frequency. It implies that the antenna has no hysteresis, reversibly deformable, and stable under different strains.

Next, the radiating performance of the LEBG-loaded slot is studied under the same strain conditions. Figure 6.16 shows the maximum farfield gains of the proposed antenna under the same strain conditions. With reference to the same figure, the maximum gain drops as the strain is increased due to the fluctuation of the operating frequency of the bandgap structure, as explained earlier. In general, the elongated antenna maintains a good and stable radiating performance of ~5.08 dBi on average, which is good enough for long-range wearable applications, as compared with other literature (Yan et al., 2014, Agarwal et al., 2016, Raad et al., 2012, Sanusi et al., 2019).

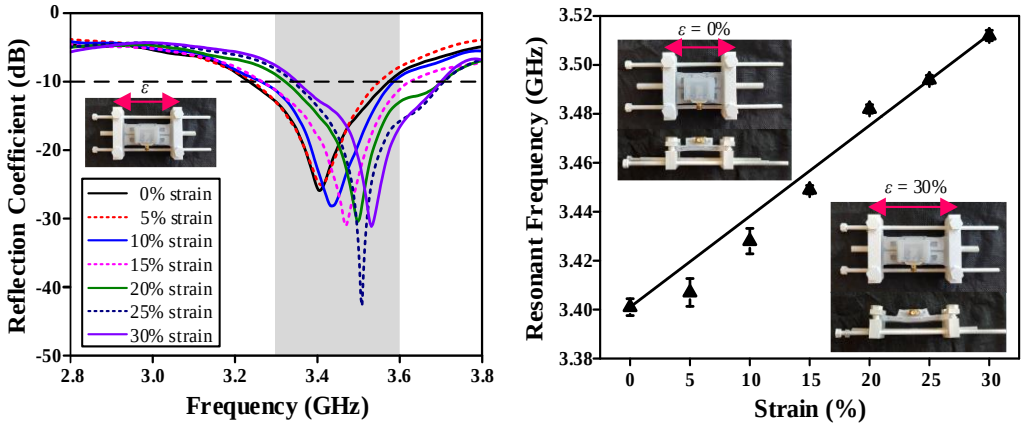

(a) (b)

Figure 6.15: (a) Measured $|S_{11}|$ and (b) resonant frequency of the proposed LEBG-backed slot antenna under different strains (ε). Insets show the measurement setup. The greyed region represents the sub-6GHz passband (3300-3600 MHz).

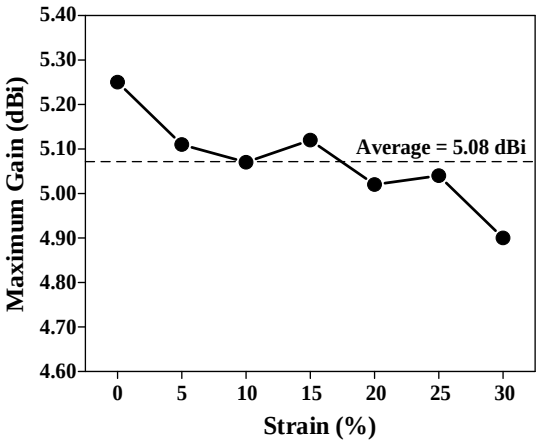

Figure 6.16: Measured maximum farfield gains at 3.401 GHz for different strains at θ = 0º in the *xz*-plane. The horizontal dashed line indicates the average gain.

6.5 Summary

A wearable antenna has been designed using an elastomer platform that is embedded with liquid metal to form an EBG-backed liquid antenna. The dielectric and conductive parts of the slot antenna as well as the LEBG are both made using the highly stretchable Ecoflex and EGaIn liquid, respectively, which allow bendability and stretchability. The LEBG is placed beneath the antenna

for mitigating the effects of human body on the radiation performance. It has been demonstrated that the insertion of the LEBG structure underneath the slot antenna can improve the antenna gain from 2.24 to 5.80 dBi by substantially reducing the back lobes. At the same time, the SAR can be reduced from 4.89 to 1.25 W/kg (1 g US standard). The proposed antenna resonates at 3.401 GHz and has good impedance matching in the entire sub-6 GHz band (3300−3600 MHz). Due to the existence of the LEBG, the impedance of the antenna is very stable when being applied on the different parts of human body. The high elasticity of Ecoflex and negligible stiffness of EGaIn allow the proposed antenna to bend and stretch while maintaining a stable bandwidth in the sub-6 GHz band, making it suitable for wearable application. The elongation of the antenna causes the resonant frequency to shift linearly from 3.401 GHz to 3.512 GHz when it is stretched from 0% to 30% strain, with a sensitivity of 3.71 MHz/strain(%). This shows that the antenna is able to detect strain change. The antenna is also shown to radiate well with an average of 5.08 dBi even at high strain conditions. Since the elastomer platform does not absorb water or sweat, the proposed antenna can be used in humid environment. The electrical properties of the Ecoflex are very stable since it is waterproof. Therefore, the proposed antenna is suitable for wearable applications.

CHAPTER 7

CONCLUSIONS AND FUTURE WORKS

7.1 Conclusions

In this thesis, a stretchable microfluidic sensor was first proposed for better mechanical compliance with human body and to measure human motion. It was fabricated by using the soft lithography technique, making it conformable well on human body. The sensor's high stretchability was made possible by embedding EGaIn into a spiral-shaped microchannel, which was fabricated inside a highly stretchable Ecoflex substrate. The sensing mechanism is based on the change of resistance when the sensor is being compressed or stretched. It shows that the sensor is able to detect pressure and strain. As a proof-of-concept demonstration for human motion monitoring, the proposed sensor was placed on human foot to detect foot pressure. From the sensor's output, the weightage of the stance and swing phases were captured accurately, showing the sensor is able to detect the pressure from the human foot. Since the sensor does not have wireless capability, an external antenna (Bluetooth) has to be connected to transfer data wirelessly.

To integrate wireless capability into a sensor, a new design, which is the liquid patch antenna, was made stretchable by injecting EGaIn into a stretchable PDMS substrate. The antenna has an air cavity loaded underneath the liquid

patch to increase its sensitivity towards changes in ambient pressure. When the ambient pressure changes, the internal air pressure of the antenna will change accordingly, causing the antenna to expand or contract. The deformation of the antenna structure varies under different ambient pressure conditions (-0.4 bar to 0.4 bar). It alters the electrical properties of the antenna and shifts its resonant frequency linearly in the range of 5.674 GHz – 5.815 GHz with a sensitivity of 176 MHz/bar. The antenna has also been shown to have a high radiation gain of 8.02 dBi due to the use of a single patch structure, instead of microchannels. The antenna can now function as both the radiating element and the air pressure sensor, as opposed to commercial electronic components which have only a single function.

The effects of incorporating an air cavity into the antenna design was further studied in another type of antenna called liquid dielectric resonator antenna (LDRA). To design a compact and efficient LDRA, a high-permittivity and low-loss organic liquid dielectric was contained inside an Ecoflex container. The proposed organic liquid dielectric (acetonitrile) was able to produce a high antenna gain, being 2 dB higher than that of the conventional water based LDRA. The air cavity loaded in the central part of the LDRA allows it to detect any changes in the ambient pressure with a sensitivity of 270 MHz/bar.

Lastly, a stretchable LEBG was designed using liquid metal and elastomer. It is to be attached beneath an antenna for mitigating the effects of human body on the antenna's performance. The placement of the LEBG underneath a new antenna design (slot antenna) has improved the antenna gain

in the boresight and reduced the SAR. Furthermore, the impedance of the antenna was found to be very stable when being applied on the different parts of human body. The high elasticity of the Ecoflex and the negligible stiffness of the EGaIn have allowed the proposed antenna to bend, while maintaining a stable bandwidth in the sub-6 GHz band (3300-3600 MHz). It is suitable for wearable applications. Due to the stretchability of the antenna, its resonant frequency shifts linearly from 3.401 GHz to 3.512 GHz when it is stretched from 0% to 30% strain, with a sensitivity of 3.71 MHz/strain(%). This final design of antenna has strain sensing capability, high mechanical compliance with human skin, and negligible harm to the human body. At the end of the thesis, a stretchable antenna that works well as a wearable and wireless strain sensor is developed.

7.2 Future Works

The proposed multifunctional antennas have been demonstrated to show its ability of frequency shifting when being stretched. However, the antennas' mobility is much constrained with the requirement of a coaxial cable and VNA to measure the resonant frequencies. Therefore, for the future work, we propose to incorporate Radio-frequency Identification (RFID) chip with the antennas so that the resonant frequencies can be obtained using a RFID mobile scanner. To improve the wearability, new fabrication techniques are needed to reduce the thickness of the wearable antennas. Currently, the design of the antennas (resonant frequency, radiation gain, and radiation pattern) have only been simulated using the CST simulation software. However, the sensing

performance (shifting of resonant frequency at different strains) of the multi-functional antenna is not known until the experiment is conducted. To design such multi-functional efficiently, in the future, the sensing performances of the antennas will be evaluated by using the COMSOL Multiphysics during the design stage. In addition, the performance of multifunctional antenna will be compared with existing commercialized flexible sensors.

REFERENCES

Agache, P. G., Monneur, C., Leveque, J. L. & De Rigal, J. 1980. Mechanical properties and young's modulus of human skin in vivo. *Archives of dermatological research,* 269**,** 221-232.

Agarwal, K., Guo, Y.-X. & Salam, B. 2016. Wearable amc backed near-endfire antenna for on-body communications on latex substrate. *IEEE Transactions on components, packaging and manufacturing technology,* 6**,** 346-358.

Alzoubi, K., Hamasha, M. M., Schadt, M., Lu, S., Sammakia, B. & Poliks, M. Effect of lamination on the bending fatigue life of copper coated pet substrate. Advances in Display Technologies; and E-papers and Flexible Displays, 2011. International Society for Optics and Photonics, 79560X.

Amjadi, M., Pichitpajongkit, A., Lee, S., Ryu, S. & Park, I. 2014. Highly stretchable and sensitive strain sensor based on silver nanowire–elastomer nanocomposite. *ACS nano,* 8**,** 5154-5163.

Amjadi, M., Yoon, Y. J. & Park, I. 2015. Ultra-stretchable and skin-mountable strain sensors using carbon nanotubes–ecoflex nanocomposites. *Nanotechnology,* 26**,** 375501.

Amjadi, S. M. & Soleimani, M. 2006. A novel compact artificial magnetic conductor based on multiple non-grounded vias. *PIERS Online,* 2**,** 672-675.

Anderson, I. A., Gisby, T. A., Mckay, T. G., O'brien, B. M. & Calius, E. P. 2012. Multi-functional dielectric elastomer artificial muscles for soft and smart machines. *Journal of Applied Physics,* 112**,** 041101.

Arriola, A., Sancho, J., Brebels, S., Gonzalez, M. & De Raedt, W. 2011. Stretchable dipole antenna for body area networks at 2.45 ghz. *IET microwaves, antennas & propagation,* 5**,** 852-859.

Ashyap, A. Y., Abidin, Z. Z., Dahlan, S. H., Majid, H. A., Kamarudin, M. R., Alomainy, A., Abd-Alhameed, R. A., Kosha, J. S. & Noras, J. M. 2018. Highly efficient wearable cpw antenna enabled by ebg-fss structure for medical body area network applications. *IEEE Access,* 6**,** 77529-77541.

Ashyap, A. Y., Abidin, Z. Z., Dahlan, S. H., Majid, H. A., Shah, S. M., Kamarudin, M. R. & Alomainy, A. 2017. Compact and low-profile textile ebg-based antenna for wearable medical applications. *IEEE Antennas and Wireless Propagation Letters,* 16**,** 2550-2553.

Ashyap, A. Y., Dahlan, S. H. B., Abidin, Z. Z., Abbasi, M. I., Kamarudin, M. R., Majid, H. A., Dahri, M. H., Jamaluddin, M. H. & Alomainy, A. 2020. An overview of electromagnetic band-gap integrated wearable antennas. *IEEE Access,* 8**,** 7641-7658.

Atalay, O., Atalay, A., Gafford, J., Wang, H., Wood, R. & Walsh, C. 2017. A highly stretchable capacitive ‐based strain sensor based on metal deposition and laser rastering. *Advanced Materials Technologies,* 2**,** 1700081.

Balanis, C. A. 1999. *Advanced engineering electromagnetics*, John Wiley & Sons.

Balanis, C. A. 2011. *Modern antenna handbook*, John Wiley & Sons.

Balanis, C. A. 2012. *Advanced engineering electromagnetics*, John Wiley & Sons.

Balanis, C. A. 2016. *Antenna theory: Analysis and design*, John wiley & sons.

Bashir, S. 2009. *Design and synthesis of non uniform high impedance surface based wearable antennas*. Loughborough University.

Bocharov, G., Eletskii, A. & Knizhnik, A. 2016. Nonlinear resistance of polymer composites with carbon nanotube additives in the percolation state. *Technical Physics,* 61**,** 1506-1510.

Bowden, N., Brittain, S., Evans, A. G., Hutchinson, J. W. & Whitesides, G. M. 1998. Spontaneous formation of ordered structures in thin films of metals supported on an elastomeric polymer. *Nature,* 393**,** 146-149.

Cademartiri, L., Thuo, M. M., Nijhuis, C. A., Reus, W. F., Tricard, S., Barber, J. R., Sodhi, R. N., Brodersen, P., Kim, C. & Chiechi, R. C. 2012. Electrical resistance of agts–s (ch2) n− 1ch3//ga2o3/egain tunneling junctions. *The Journal of Physical Chemistry C,* 116**,** 10848-10860.

Cai, L., Song, L., Luan, P., Zhang, Q., Zhang, N., Gao, Q., Zhao, D., Zhang, X., Tu, M. & Yang, F. 2013. Super-stretchable, transparent carbon nanotube-based capacitive strain sensors for human motion detection. *Scientific Reports,* 3**,** 1-9.

Cao, Y., Li, W. & Sepúlveda, N. 2019. Performance of self-powered, water-resistant bending sensor using transverse piezoelectric effect of polypropylene ferroelectret polymer. *IEEE Sensors Journal,* 19**,** 10327-10335.

Carver, K. & Mink, J. 1981. Microstrip antenna technology. *IEEE Transactions on Antennas and Propagation,* 29**,** 2-24.

Cavcar, M. 2000. The international standard atmosphere (isa). *Anadolu University, Turkey,* 30.

Chabala, J. M. 1992. Oxide-growth kinetics and fractal-like patterning across liquid gallium surfaces. *Physical Review B,* 46**,** 11346.

Chandler, J., Messer, H. & Ellender, G. 1994. Cytotoxicity of gallium and indium ions compared with mercuric ion. *Journal of Dental Research,* 73**,** 1554-1559.

Chart, R. C. R. 2019. Available: https://mykin.com/rubber-chemical-resistance-chart/ [Accessed 03 October 2019].

Chen, J.-J., Lan, C.-H., Jeng, M.-S. & Xu, T. 2007. The development of fan filter unit with flow rate feedback control in a cleanroom. *Building and Environment,* 42**,** 3556-3561.

Chen, X., Li, B., Qiao, Y. & Lu, Z. 2019. Preparing polypyrrole-coated stretchable textile via low-temperature interfacial polymerization for highly sensitive strain sensor. *Micromachines,* 10**,** 788.

Chen, Z. & Wong, H. 2017a. Liquid dielectric resonator antenna with circular polarization reconfigurability. *IEEE Transactions on Antennas and Propagation,* 66**,** 444-449.

Chen, Z. & Wong, H. 2017b. Wideband glass and liquid cylindrical dielectric resonator antenna for pattern reconfigurable design. *IEEE Transactions on Antennas and Propagation,* 65**,** 2157-2164.

Cheng, S. & Wu, Z. 2010. Microfluidic stretchable rf electronics. *Lab on a Chip,* 10**,** 3227-3234.

Cheng, S. & Wu, Z. 2011. A microfluidic, reversibly stretchable, large‐area wireless strain sensor. *Advanced Functional Materials,* 21**,** 2282-2290.

Cheng, S. & Wu, Z. 2012. Microfluidic electronics. *Lab on a Chip,* 12**,** 2782-2791.

Chiechi, R. C., Weiss, E. A., Dickey, M. D. & Whitesides, G. M. 2008. Eutectic gallium‐indium (egain): A moldable liquid metal for electrical characterization of self‐assembled monolayers. *Angewandte Chemie International Edition,* 47**,** 142-144.

Chuang, C.-T. & Chung, S.-J. 2011. A compact printed filtering antenna using a ground-intruded coupled line resonator. *IEEE Transactions on Antennas and Propagation,* 59**,** 3630-3637.

Clarkson, T. W. & Magos, L. 2006. The toxicology of mercury and its chemical compounds. *Critical Reviews in Toxicology,* 36**,** 609-662.

Dahlberg, T., Stangner, T., Zhang, H., Wiklund, K., Lundberg, P., Edman, L. & Andersson, M. 2018. 3d printed water-soluble scaffolds for rapid production of pdms micro-fluidic flow chambers. *Scientific Reports,* 8**,** 1-10.

Deschamps, G. A. Microstrip microwave antennas. Proceedings of the Third Symposium on the USAF Antenna Research and Development Program, Oct, 1953. 18-22.

Dickey, M. D. 2017. Stretchable and soft electronics using liquid metals. *Advanced materials,* 29**,** 1606425.

Dickey, M. D., Chiechi, R. C., Larsen, R. J., Weiss, E. A., Weitz, D. A. & Whitesides, G. M. 2008. Eutectic gallium‐indium (egain): A liquid metal alloy for the formation of stable structures in microchannels at room temperature. *Advanced Functional Materials,* 18**,** 1097-1104.

Ding, S., Jiu, J., Gao, Y., Tian, Y., Araki, T., Sugahara, T., Nagao, S., Nogi, M., Koga, H. & Suganuma, K. 2016. One-step fabrication of stretchable copper nanowire conductors by a fast photonic sintering technique and its application in wearable devices. *ACS applied materials & interfaces,* 8**,** 6190-6199.

Fahim, M., Bijwe, J. & Nalwa, H. S. 2001. Polyimides for microelectronics and tribology applications. *Supramolecular photosensitive and electroactive materials.* Elsevier.

Fan, Q., Qin, Z., Gao, S., Wu, Y., Pionteck, J., Mäder, E. & Zhu, M. 2012. The use of a carbon nanotube layer on a polyurethane multifilament substrate for monitoring strains as large as 400%. *Carbon,* 50**,** 4085-4092.

Fassler, A. & Majidi, C. 2013. 3d structures of liquid-phase gain alloy embedded in pdms with freeze casting. *Lab on a Chip,* 13**,** 4442-4450.

Fuard, D., Tzvetkova-Chevolleau, T., Decossas, S., Tracqui, P. & Schiavone, P. 2008. Optimization of poly-di-methyl-siloxane (pdms) substrates for studying cellular adhesion and motility. *Microelectronic Engineering,* 85**,** 1289-1293.

Gao, G.-P., Hu, B., Wang, S.-F. & Yang, C. 2018. Wearable circular ring slot antenna with ebg structure for wireless body area network. *IEEE Antennas and Wireless Propagation Letters,* 17**,** 434-437.

Gao, G., Wang, S., Zhang, R., Yang, C. & Hu, B. 2020. Flexible ebg‐backed pifa based on conductive textile and pdms for wearable applications. *Microwave and Optical Technology Letters,* 62**,** 1733-1741.

Gogurla, N., Roy, B., Park, J.-Y. & Kim, S. 2019. Skin-contact actuated single-electrode protein triboelectric nanogenerator and strain sensor for biomechanical energy harvesting and motion sensing. *Nano Energy,* 62**,** 674-681.

Goussetis, G., Feresidis, A. P. & Vardaxoglou, J. C. 2006. Tailoring the amc and ebg characteristics of periodic metallic arrays printed on grounded dielectric substrate. *IEEE Transactions on Antennas and Propagation,* 54**,** 82-89.

Gozen, B. A., Tabatabai, A., Ozdoganlar, O. B. & Majidi, C. 2014. High‐density soft‐matter electronics with micron‐scale line width. *Advanced materials,* 26**,** 5211-5216.

Guha, D., Banerjee, A., Kumar, C. & Antar, Y. M. 2011. Higher order mode excitation for high-gain broadside radiation from cylindrical dielectric resonator antennas. *IEEE Transactions on Antennas and Propagation,* 60**,** 71-77.

Guo, Y.-X. & Luk, K.-M. 2003. On improving coupling between a coplanar waveguide feed and a dielectric resonator antenna. *IEEE Transactions on Antennas and Propagation,* 51**,** 2144-2146.

Guo, Y., Kong, J., Liu, H., Hu, D. & Qin, L. 2016. Design and investigation of a reusable surface-mounted optical fiber bragg grating strain sensor. *IEEE Sensors Journal,* 16**,** 8456-8462.

Gutton, H. & Baissinot, G. 1955. Flat aerial for ultra high frequencies. *French patent,* 703113.

Hadarig, R. C., De Cos, M. E. & Las-Heras, F. 2013. Uhf dipole-amc combination for rfid applications. *IEEE Antennas and Wireless Propagation Letters,* 12**,** 1041-1044.

Hayes, G. J., So, J.-H., Qusba, A., Dickey, M. D. & Lazzi, G. 2012. Flexible liquid metal alloy (egain) microstrip patch antenna. *IEEE Transactions on Antennas and Propagation,* 60**,** 2151-2156.

Haynes, W. 2011. Crc handbook of chemistry and physics 92nd edition crc press. Taylor and Francis, Boca Raton.

Hessert, M. J., Vyas, M., Leach, J., Hu, K., Lipsitz, L. A. & Novak, V. 2005. Foot pressure distribution during walking in young and old adults. *BMC geriatrics,* 5**,** 8.

Holloway, C. L. & Kuester, E. F. 1998. Net and partial inductance of a microstrip ground plane. *IEEE Transactions on Electromagnetic Compatibility,* 40**,** 33-46.

Hu, B., Gao, G.-P., He, L.-L., Cong, X.-D. & Zhao, J.-N. 2015. Bending and on-arm effects on a wearable antenna for 2.45 ghz body area network. *IEEE Antennas and Wireless Propagation Letters,* 15**,** 378-381.

Huang, Y., He, X., Gao, L., Wang, Y., Liu, C. & Liu, P. 2017. Pressure-sensitive carbon black/graphene nanoplatelets-silicone rubber hybrid conductive composites based on a three-dimensional polydopamine-modified polyurethane sponge. *Journal of Materials Science: Materials in Electronics,* 28**,** 9495-9504.

Huang, Y., Wang, Y., Xiao, L., Liu, H., Dong, W. & Yin, Z. 2014. Microfluidic serpentine antennas with designed mechanical tunability. *Lab on a Chip,* 14**,** 4205-4212.

Huang, Y., Zhao, Y., Wang, Y., Guo, X., Zhang, Y., Liu, P., Liu, C. & Zhang, Y. 2018. Highly stretchable strain sensor based on polyurethane substrate using hydrogen bond-assisted laminated structure for monitoring of tiny human motions. *Smart Materials and Structures,* 27**,** 035013.

Ittipiboon, A., Mongia, R., Antar, Y., Bhartia, P. & Cuhaci, M. An integrated rectangular dielectric resonator antenna. Proceedings of IEEE Antennas and Propagation Society International Symposium, 1993. IEEE, 604-607.

Jacobsen, R. E., Lavrinenko, A. V. & Arslanagić, S. 2019. Electrically small water-based hemispherical dielectric resonator antenna. *Applied Sciences,* 9**,** 4848.

Jiang, Z. H., Brocker, D. E., Sieber, P. E. & Werner, D. H. 2014. A compact, low-profile metasurface-enabled antenna for wearable medical body-area network devices. *IEEE Transactions on Antennas and Propagation,* 62**,** 4021-4030.

Jiang, Z. H., Cui, Z., Yue, T., Zhu, Y. & Werner, D. H. 2017. Compact, highly efficient, and fully flexible circularly polarized antenna enabled by silver nanowires for wireless body-area networks. *IEEE transactions on biomedical circuits and systems,* 11**,** 920-932.

Johnston, I., Mccluskey, D., Tan, C. & Tracey, M. 2014. Mechanical characterization of bulk sylgard 184 for microfluidics and microengineering. *Journal of Micromechanics and Microengineering,* 24**,** 035017.

Junker, G., Kishk, A., Glisson, A. & Kajfez, D. 1994a. Effect of an air gap around the coaxial probe exciting a cylindrical dielectric resonator antenna. *Electronics Letters,* 30**,** 177-178.

Junker, G., Kishk, A., Glisson, A. & Kajfez, D. 1995. Effect of fabrication imperfections for ground-plane-backed dielectric-resonator antennas. *IEEE Antennas and propagation Magazine,* 37**,** 40-47.

Junker, G., Kishk, A., Glisson, A. & Kajifez, D. 1994b. Effect of air gap on cylindrical dielectric resonator antenna operating in tm/sub 01/mode. *Electronics Letters,* 30**,** 97-98.

Kajfez, D. & Guillon, P. 1986. Dielectric resonators. *Norwood*.

Kamei, K.-i., Mashimo, Y., Koyama, Y., Fockenberg, C., Nakashima, M., Nakajima, M., Li, J. & Chen, Y. 2015. 3d printing of soft lithography mold for rapid production of polydimethylsiloxane-based microfluidic devices for cell stimulation with concentration gradients. *Biomedical Microdevices,* 17**,** 36.

Kellis, E. 2001. Plantar pressure distribution during barefoot standing, walking and landing in preschool boys. *Gait & posture,* 14**,** 92-97.

Khan, H., Razmjou, A., Ebrahimi Warkiani, M., Kottapalli, A. & Asadnia, M. 2018. Sensitive and flexible polymeric strain sensor for accurate human motion monitoring. *Sensors,* 18**,** 418.

Kim, H.-J., Maleki, T., Wei, P. & Ziaie, B. 2009. A biaxial stretchable interconnect with liquid-alloy-covered joints on elastomeric substrate. *Journal of Microelectromechanical Systems,* 18**,** 138-146.

Kim, H.-J., Son, C. & Ziaie, B. 2008. A multiaxial stretchable interconnect using liquid-alloy-filled elastomeric microchannels. *Applied physics letters,* 92**,** 011904.

Kim, S.-R., Kim, J.-H. & Park, J.-W. 2017. Wearable and transparent capacitive strain sensor with high sensitivity based on patterned ag nanowire networks. *ACS applied materials & interfaces,* 9**,** 26407-26416.

Kim, Y.-S., Basir, A., Herbert, R., Kim, J., Yoo, H. & Yeo, W.-H. 2019. Soft materials, stretchable mechanics, and optimized designs for body-wearable compliant antennas. *ACS applied materials & interfaces,* 12**,** 3059-3067.

Kranenburg, R. & Long, S. 1988. Microstrip transmission line excitation of dielectric resonator antennas. *Electronics Letters,* 24**,** 1156-1157.

Kranenburg, R. A., Long, S. A. & Williams, J. T. 1991. Coplanar waveguide excitation of dielectric resonator antennas. *IEEE Transactions on Antennas and Propagation,* 39**,** 119-122.

Kubo, M., Li, X., Kim, C., Hashimoto, M., Wiley, B. J., Ham, D. & Whitesides, G. M. 2010. Stretchable microfluidic radiofrequency antennas. *Advanced materials,* 22**,** 2749-2752.

Kuo, A. C. 1999. Poly (dimethylsiloxane). *Polymer data handbook***,** 411-435.

Lacour, S. P., Jones, J., Wagner, S., Li, T. & Suo, Z. 2005. Stretchable interconnects for elastic electronic surfaces. *Proceedings of the IEEE,* 93**,** 1459-1467.

Lacour, S. P., Wagner, S., Huang, Z. & Suo, Z. 2003. Stretchable gold conductors on elastomeric substrates. *Applied physics letters,* 82**,** 2404-2406.

Langley, R. J. & Parker, E. A. 1982. Equivalent circuit model for arrays of square loops. *Electronics Letters,* 18**,** 294-296.

Lee, J., Kim, S., Lee, J., Yang, D., Park, B. C., Ryu, S. & Park, I. 2014. A stretchable strain sensor based on a metal nanoparticle thin film for human motion detection. *Nanoscale,* 6**,** 11932-11939.

Lee, K. Y., Chung, B. K., You, K. Y., Cheng, E. M. & Abbas, Z. 2013. Study of dual open ended coaxial sensor system for calculation of phase using two magnitudes. *IEEE Sensors Journal,* 14**,** 129-134.

Leung, K., Lai, K., Luk, K. & Lin, D. 1993. Input impedance of aperture coupled hemispherical dielectric resonator antenna. *Electronics Letters,* 29**,** 1165-1167.

Leung, K. W., Fang, X., Pan, Y., Lim, E., Luk, K. M. & Chan, H. 2012. Dual-function radiating glass for antennas and light covers—part ii: Dual-band glass dielectric resonator antennas. *IEEE Transactions on Antennas and Propagation,* 61**,** 587-597.

Li, Q., Li, J., Tran, D., Luo, C., Gao, Y., Yu, C. & Xuan, F. 2017. Engineering of carbon nanotube/polydimethylsiloxane nanocomposites with enhanced sensitivity for wearable motion sensors. *Journal of Materials Chemistry C,* 5**,** 11092-11099.

Liang, X.-L., Denidni, T. A. & Zhang, L.-N. 2009. Wideband l-shaped dielectric resonator antenna with a conformal inverted-trapezoidal patch feed. *IEEE Transactions on Antennas and Propagation,* 57**,** 271-274.

Lin, P.-C. & Yang, S. 2007. Spontaneous formation of one-dimensional ripples in transit to highly ordered two-dimensional herringbone structures through sequential and unequal biaxial mechanical stretching. *Applied physics letters,* 90**,** 241903.

Lin, Y., Liu, S., Chen, S., Wei, Y., Dong, X. & Liu, L. 2016. A highly stretchable and sensitive strain sensor based on graphene–elastomer composites with a novel double-interconnected network. *Journal of Materials Chemistry C,* 4**,** 6345-6352.

Liu, Y., Wang, S., Li, N., Wang, J.-B. & Zhao, J. 2018. A compact dual-band dual-polarized antenna with filtering structures for sub-6 ghz base station applications. *IEEE Antennas and Wireless Propagation Letters,* 17**,** 1764-1768.

Liu, Z., Fang, S., Moura, F., Ding, J., Jiang, N., Di, J., Zhang, M., Lepró, X., Galvao, D. & Haines, C. 2015. Hierarchically buckled sheath-core fibers for superelastic electronics, sensors, and muscles. *Science,* 349**,** 400-404.

Long, S., Mcallister, M. & Shen, L. 1983. The resonant cylindrical dielectric cavity antenna. *IEEE Transactions on Antennas and Propagation,* 31**,** 406-412.

Low, J.-H., Chee, P.-S. & Lim, E.-H. 2019. Deformable liquid metal patch antenna for air pressure detection. *IEEE Sensors Journal,* 20**,** 3963-3970.

Lu, N., Lu, C., Yang, S. & Rogers, J. 2012. Highly sensitive skin‐mountable strain gauges based entirely on elastomers. *Advanced Functional Materials,* 22**,** 4044-4050.

Lu, Y., Hu, Q., Lin, Y., Pacardo, D. B., Wang, C., Sun, W., Ligler, F. S., Dickey, M. D. & Gu, Z. 2015. Transformable liquid-metal nanomedicine. *Nature communications,* 6**,** 10066.

Luk, K. M. L., Kwok Wa 2003. *Dielectric resonator antennas,* Baldock, U.K., Research Studies Press.

Mai, A. & Commuri, S. 2016. Intelligent control of a prosthetic ankle joint using gait recognition. *Control Engineering Practice,* 49**,** 1-13.

Martin, J. S., Antar, Y., Kishk, A., Ittipiboon, A. & Cuhaci, M. 1990. Dielectric resonator antenna using aperture coupling. *Electronics Letters,* 26**,** 2015-2016.

Martinez, R. V., Glavan, A. C., Keplinger, C., Oyetibo, A. I. & Whitesides, G. M. 2014. Soft actuators and robots that are resistant to mechanical damage. *Advanced Functional Materials,* 24**,** 3003-3010.

Matsuhisa, N., Inoue, D., Zalar, P., Jin, H., Matsuba, Y., Itoh, A., Yokota, T., Hashizume, D. & Someya, T. 2017. Printable elastic conductors by in situ

formation of silver nanoparticles from silver flakes. *Nature materials,* 16**,** 834-840.

Mengüç, Y., Park, Y.-L., Pei, H., Vogt, D., Aubin, P. M., Winchell, E., Fluke, L., Stirling, L., Wood, R. J. & Walsh, C. J. 2014. Wearable soft sensing suit for human gait measurement. *The International Journal of Robotics Research,* 33**,** 1748-1764.

Mongia, R. 1989. Half-split dielectric resonator placed on metallic plane for antenna applications. *Electronics Letters,* 25**,** 462-464.

Mongia, R., Ittipiboon, A., Antar, Y., Bhartia, P. & Cuhaci, M. 1993a. A half-split cylindrical dielectric resonator antenna using slot-coupling. *IEEE Microwave and Guided wave letters,* 3**,** 38-39.

Mongia, R., Ittipiboon, A., Bhartia, P. & Cuhaci, M. 1993b. Electric-monopole antenna using a dielectric ring resonator. *Electronics Letters,* 29**,** 1530-1531.

Mongia, R. K. & Bhartia, P. 1994. Dielectric resonator antennas—a review and general design relations for resonant frequency and bandwidth. *International Journal of Microwave and Millimeter‐Wave Computer‐Aided Engineering,* 4**,** 230-247.

Morley, N., Burris, J., Cadwallader, L. & Nornberg, M. 2008. Gainsn usage in the research laboratory. *Review of Scientific Instruments,* 79**,** 056107.

Munson, R. 1974. Conformal microstrip antennas and microstrip phased arrays. *IEEE Transactions on Antennas and Propagation,* 22**,** 74-78.

Nalwa, H. S. 1999. *Handbook of low and high dielectric constant materials and their applications, two-volume set,* Elsevier.

O'keefe, G, S. & Kingsley, S. P. 2007. Tunability of liquid dielectric resonator antennas. *IEEE Antennas and Wireless Propagation Letters,* 6**,** 533-536.

O'keefe, S. G., Kingsley, S. P. & Saario, S. 2002. Fdtd simulation of radiation characteristics of half-volume hem-and te-mode dielectric resonator antennas. *IEEE Transactions on Antennas and Propagation,* 50**,** 175-179.

Obitayo, W. & Liu, T. 2012. A review: Carbon nanotube-based piezoresistive strain sensors. *Journal of Sensors,* 2012.

Okaya, A. 1960. The rutile microwave resonator. *PROCEEDINGS OF THE INSTITUTE OF RADIO ENGINEERS,* 48**,** 1921-1921.

Ounpuu, S. 1994. The biomechanics of walking and running. *Clinics in sports medicine,* 13**,** 843-863.

Overvelde, J. T., Mengüç, Y., Polygerinos, P., Wang, Y., Wang, Z., Walsh, C. J., Wood, R. J. & Bertoldi, K. 2014. Mechanical and electrical numerical analysis of soft liquid-embedded deformation sensors analysis. *Extreme Mechanics Letters,* 1**,** 42-46.

Pailler-Mattei, C., Bec, S. & Zahouani, H. 2008. In vivo measurements of the elastic mechanical properties of human skin by indentation tests. *Medical Engineering & Physics,* 30**,** 599-606.

Park, Y.-L., Chen, B.-R. & Wood, R. J. 2012. Design and fabrication of soft artificial skin using embedded microchannels and liquid conductors. *IEEE Sensors Journal,* 12**,** 2711-2718.

Park, Y.-L., Majidi, C., Kramer, R., Bérard, P. & Wood, R. J. 2010. Hyperelastic pressure sensing with a liquid-embedded elastomer. *Journal of Micromechanics and Microengineering,* 20**,** 125029.

Petrović, Z. S. & Budinski-Simendić, J. 1985. Study of the effect of soft-segment length and concentration on properties of polyetherurethanes. Ii. The effect on mechanical properties. *Rubber Chemistry and Technology,* 58**,** 701-712.

Plech, A., Klemradt, U., Metzger, H. & Peisl, J. 1998. In situ x-ray reflectivity study of the oxidation kinetics of liquid gallium and the liquid alloy. *Journal of Physics: Condensed Matter,* 10**,** 971.

Pook, M., Loo, S. M. & Kiepert, J. Monitoring of the aircraft cabin environment via a wireless sensor network. 42nd International Conference on Environmental Systems, 2012. 3462.

Preston, J. & Black, W. 1967. New high temperature polymers. Vi. Ordered heterocycle copolymers. *Journal of Polymer Science Part A‐1: Polymer Chemistry,* 5**,** 2429-2439.

Raad, H. R., Abbosh, A. I., Al-Rizzo, H. M. & Rucker, D. G. 2012. Flexible and compact amc based antenna for telemedicine applications. *IEEE Transactions on Antennas and Propagation,* 61**,** 524-531.

Rantala, J., Hännikäinen, J. & Vanhala, J. 2011. Fiber optic sensors for wearable applications. *Personal and Ubiquitous Computing,* 15**,** 85-96.

Ray, S., Berger, D., Czornyj, G., Kumar, A. & Tummala, R. Dual-level metal (dlm) method for fabricating thin film wiring structures. Proceedings of IEEE 43rd Electronic Components and Technology Conference (ECTC'93), 1993. IEEE, 538-543.

Rea, S., Linton, D., Orr, E. & Mcconnell, J. 2006. Broadband high-impedance surface design for aircraft hirf protection. *IEE Proceedings-Microwaves, Antennas and Propagation,* 153**,** 307-313.

Regan, M., Tostmann, H., Pershan, P. S., Magnussen, O., Dimasi, E., Ocko, B. & Deutsch, M. 1997. X-ray study of the oxidation of liquid-gallium surfaces. *Physical Review B,* 55**,** 10786.

Rosenberger, M., Hessler, S., Belle, S., Schmauss, B. & Hellmann, R. 2014. Compressive and tensile strain sensing using a polymer planar bragg grating. *Optics Express,* 22**,** 5483-5490.

Saed, M. A. & Yadla, R. 2006. Microstrip-fed low profile and compact dielectric resonator antennas. *Progress In Electromagnetics Research,* 56**,** 151-162.

Saggiomo, V. & Velders, A. H. 2015. Simple 3d printed scaffold ‐ removal method for the fabrication of intricate microfluidic devices. *Advanced Science,* 2**,** 1500125.

Sahatiya, P. & Badhulika, S. 2017. Eraser-based eco-friendly fabrication of a skin-like large-area matrix of flexible carbon nanotube strain and pressure sensors. *Nanotechnology,* 28**,** 095501.

Sakthipriya, N. 2014. An effective method for crop monitoring using wireless sensor network. *Middle-East Journal of Scientific Research,* 20**,** 1127-1132.

Sallam, M. O., Kandil, S. M., Volski, V., Vandenbosch, G. A. & Soliman, E. A. 2017. Wideband cpw-fed flexible bow-tie slot antenna for wlan/wimax systems. *IEEE Transactions on Antennas and Propagation,* 65**,** 4274-4277.

Salonen, P., Keskilammi, M. & Sydanheimo, L. 2001. A low-cost 2.45 ghz photonic band-gap patch antenna for wearable systems.

Salonen, P., Yang, F., Rahmat-Samii, Y. & Kivikoski, M. Webga-wearable electromagnetic band-gap antenna. IEEE Antennas and Propagation Society Symposium, 2004., 2004. IEEE, 451-454.

Samal, P. B., Soh, P. J. & Vandenbosch, G. A. 2013. Uwb all-textile antenna with full ground plane for off-body wban communications. *IEEE Transactions on Antennas and Propagation,* 62**,** 102-108.

Sanusi, O. M., Ghaffar, F. A., Shamim, A., Vaseem, M., Wang, Y. & Roy, L. 2019. Development of a 2.45 ghz antenna for flexible compact radiation dosimeter tags. *IEEE Transactions on Antennas and Propagation,* 67**,** 5063-5072.

Scharmann, F., Cherkashinin, G., Breternitz, V., Knedlik, C., Hartung, G., Weber, T. & Schaefer, J. 2004. Viscosity effect on gainsn studied by xps. *Surface and Interface Analysis: An International Journal devoted to the development and application of techniques for the analysis of surfaces, interfaces and thin films,* 36**,** 981-985.

Schneider, F., Fellner, T., Wilde, J. & Wallrabe, U. 2008. Mechanical properties of silicones for mems. *Journal of Micromechanics and Microengineering,* 18**,** 065008.

Sekitani, T., Noguchi, Y., Hata, K., Fukushima, T., Aida, T. & Someya, T. 2008. A rubberlike stretchable active matrix using elastic conductors. *Science,* 321**,** 1468-1472.

Shakhirul, M., Jusoh, M., Sahadah, A., Nor, C. & Rahim, H. A. 2014. Embroidered wearable textile antenna on bending and wet performances for uwb reception. *Microwave and Optical Technology Letters,* 56**,** 2158-2163.

Shengbo, S., Lihua, L., Aoqun, J., Qianqian, D., Jianlong, J., Qiang, Z. & Wendong, Z. 2018. Highly sensitive wearable strain sensor based on silver nanowires and nanoparticles. *Nanotechnology,* 29**,** 255202.

Shintake, J., Piskarev, E., Jeong, S. H. & Floreano, D. 2018. Ultrastretchable strain sensors using carbon black‐filled elastomer composites and comparison of capacitive versus resistive sensors. *Advanced Materials Technologies,* 3**,** 1700284.

Shu, L., Hua, T., Wang, Y., Li, Q., Feng, D. D. & Tao, X. 2010. In-shoe plantar pressure measurement and analysis system based on fabric pressure sensing array. *IEEE transactions on information technology in biomedicine,* 14**,** 767-775.

Shum, S.-M. & Luk, K.-M. 1998. Fdtd analysis of probe-fed cylindrical dielectric resonator antenna. *IEEE Transactions on Antennas and Propagation,* 46**,** 325-333.

Sievenpiper, D., Zhang, L., Broas, R. F., Alexopolous, N. G. & Yablonovitch, E. 1999. High-impedance electromagnetic surfaces with a forbidden frequency band. *IEEE Transactions on Microwave Theory and Techniques,* 47**,** 2059-2074.

Simeoni, M., Cicchetti, R., Yarovoy, A. & Caratelli, D. Supershaped dielectric resonator antennas. 2009 IEEE Antennas and Propagation Society International Symposium, 2009. IEEE, 1-4.

Simeoni, M., Cicchetti, R., Yarovoy, A. & Caratelli, D. 2011. Plastic-based supershaped dielectric resonator antennas for wide-band applications. *IEEE Transactions on Antennas and Propagation,* 59**,** 4820-4825.

Simorangkir, R. B., Yang, Y., Hashmi, R. M., Björninen, T., Esselle, K. P. & Ukkonen, L. 2018. Polydimethylsiloxane-embedded conductive fabric: Characterization and application for realization of robust passive and active flexible wearable antennas. *IEEE Access,* 6**,** 48102-48112.

Simorangkir, R. B., Yang, Y., Matekovits, L. & Esselle, K. P. 2016. Dual-band dual-mode textile antenna on pdms substrate for body-centric communications. *IEEE Antennas and Wireless Propagation Letters,* 16**,** 677-680.

Smooth-On. 2021. *Ecoflex^{tm} 00-50* [Online]. Available: https://www.smooth-on.com/products/ecoflex-00-50/ [Accessed 25 October 2021].

So, J. H., Thelen, J., Qusba, A., Hayes, G. J., Lazzi, G. & Dickey, M. D. 2009. Reversibly deformable and mechanically tunable fluidic antennas. *Advanced Functional Materials,* 19**,** 3632-3637.

Song, C., Bennett, E. L., Xiao, J., Alieldin, A., Luk, K.-M. & Huang, Y. 2019. Metasurfaced, broadband and circularly polarized liquid antennas using a simple structure. *IEEE Transactions on Antennas and Propagation*.

Song, J., Huang, Y., Xiao, J., Wang, S., Hwang, K.-C., Ko, H., Kim, D.-H., Stoykovich, M. & Rogers, J. A. 2009. Mechanics of noncoplanar mesh design for stretchable electronic circuits. *Journal of Applied Physics,* 105**,** 123516.

St Clair, A., St Clair, T., Slemp, W., Weber, W. & Gupta, M. 1987. Proceeding of the 2nd international conference on polyimides.

Sugihara, T., Ohura, T., Homma, K. & Igawa, H. 1991. The extensibility in human skin: Variation according to age and site. *British Journal of Plastic Surgery,* 44**,** 418-422.

Sun, G.-H., Wong, S.-W., Zhu, L. & Chu, Q.-X. 2015. A compact printed filtering antenna with good suppression of upper harmonic band. *IEEE Antennas and Wireless Propagation Letters,* 15**,** 1349-1352.

Sun, Y., Lacour, S., Brooks, R., Rushton, N., Fawcett, J. & Cameron, R. 2009. Assessment of the biocompatibility of photosensitive polyimide for implantable medical device use. *Journal of Biomedical Materials Research Part A: An Official Journal of The Society for Biomaterials, The Japanese Society for Biomaterials, and The Australian Society for Biomaterials and the Korean Society for Biomaterials,* 90**,** 648-655.

Suzuki, K., Yataka, K., Okumiya, Y., Sakakibara, S., Sako, K., Mimura, H. & Inoue, Y. 2016. Rapid-response, widely stretchable sensor of aligned mwcnt/elastomer composites for human motion detection. *Acs Sensors,* 1**,** 817-825.

Tagarielli, V. L., Hildick-Smith, R. & Huber, J. 2012. Electro-mechanical properties and electrostriction response of a rubbery polymer for eap applications. *International Journal of Solids and Structures,* 49**,** 3409-3415.

Tao, W., Liu, T., Zheng, R. & Feng, H. 2012. Gait analysis using wearable sensors. *Sensors,* 12**,** 2255-2283.

Wallach, M. 1968. Structure‐property relations of polyimide films. *Journal of Polymer Science Part A‐2: Polymer Physics,* 6**,** 953-960.

Wang, M. & Chu, Q.-X. 2019. A wideband polarization-reconfigurable water dielectric resonator antenna. *IEEE Antennas and Wireless Propagation Letters,* 18**,** 402-406.

Wang, M., Trlica, C., Khan, M., Dickey, M. & Adams, J. 2015. A reconfigurable liquid metal antenna driven by electrochemically controlled capillarity. *Journal of Applied Physics,* 117**,** 194901.

Wang, S., Xu, J., Wang, W., Wang, G.-J. N., Rastak, R., Molina-Lopez, F., Chung, J. W., Niu, S., Feig, V. R. & Lopez, J. 2018a. Skin electronics from scalable fabrication of an intrinsically stretchable transistor array. *Nature,* 555**,** 83-88.

Wang, X., Guo, R., Yuan, B., Yao, Y., Wang, F. & Liu, J. Ni-doped liquid metal printed highly stretchable and conformable strain sensor for multifunctional human-motion monitoring. 2018 40th Annual International Conference of the IEEE Engineering in Medicine and Biology Society (EMBC), 2018b. IEEE, 3276-3279.

Wang, X., Hu, Y., Song, L., Yang, H., Xing, W. & Lu, H. 2011. In situ polymerization of graphene nanosheets and polyurethane with enhanced mechanical and thermal properties. *Journal of Materials Chemistry,* 21**,** 4222-4227.

Wang, Y., Li, Z. & Xiao, J. 2016a. Stretchable thin film materials: Fabrication, application, and mechanics. *Journal of Electronic Packaging,* 138.

Wang, Z., Huang, Y., Sun, J., Huang, Y., Hu, H., Jiang, R., Gai, W., Li, G. & Zhi, C. 2016b. Polyurethane/cotton/carbon nanotubes core-spun yarn as high reliability stretchable strain sensor for human motion detection. *ACS applied materials & interfaces,* 8**,** 24837-24843.

Whittle, M. W. 2014. *Gait analysis: An introduction*, Butterworth-Heinemann.

Wu, Z., Hjort, K. & Jeong, S. H. 2015. Microfluidic stretchable radio-frequency devices. *Proceedings of the IEEE,* 103**,** 1211-1225.

Xia, Y. & Whitesides, G. M. 1998. Soft lithography. *Annual Review of Materials Science,* 28**,** 153-184.

Xiaomu, H., Yan, S. & Vandenbosch, G. A. 2017. Wearable button antenna for dual-band wlan applications with combined on and off-body radiation patterns. *IEEE Transactions on Antennas and Propagation,* 65**,** 1384-1387.

Xing, L., Huang, Y., Xu, Q. & Alja'afreh, S. 2015. A wideband hybrid water antenna with an f-shaped monopole. *IEEE Access,* 3**,** 1179-1187.

Xue-Fen, W., Yi, Y. & Jian, C. Wireless sensor node with lightning and atmospheric pressure detection for severe convective weather warning networks. 2018 International Symposium in Sensing and Instrumentation in IoT Era (ISSI), 2018. IEEE, 1-6.

Yamada, T., Hayamizu, Y., Yamamoto, Y., Yomogida, Y., Izadi-Najafabadi, A., Futaba, D. N. & Hata, K. 2011. A stretchable carbon nanotube strain sensor for human-motion detection. *Nature nanotechnology,* 6**,** 296.

Yan, S., Soh, P. J. & Vandenbosch, G. A. 2014. Low-profile dual-band textile antenna with artificial magnetic conductor plane. *IEEE Transactions on Antennas and Propagation,* 62**,** 6487-6490.

Yan, S., Soh, P. J. & Vandenbosch, G. A. 2018. Wearable ultrawideband technology—a review of ultrawideband antennas, propagation channels, and applications in wireless body area networks. *IEEE Access,* 6**,** 42177-42185.

Yang, F. & Rahmat-Samii, Y. 2003. Reflection phase characterizations of the ebg ground plane for low profile wire antenna applications. *IEEE Transactions on Antennas and Propagation,* 51**,** 2691-2703.

Yang, F. & Rahmat-Samii, Y. 2009. *Electromagnetic band gap structures in antenna engineering,* Cambridge university press Cambridge, UK.

Yeo, J. C., Yap, H. K., Xi, W., Wang, Z., Yeow, C. H. & Lim, C. T. 2016. Flexible and stretchable strain sensing actuator for wearable soft robotic applications. *Advanced Materials Technologies,* 1**,** 1600018.

Zhang, X. Y., Duan, W. & Pan, Y.-M. 2015. High-gain filtering patch antenna without extra circuit. *IEEE Transactions on Antennas and Propagation,* 63**,** 5883-5888.

Zhou, R., Zhang, H. & Xin, H. 2014. Liquid-based dielectric resonator antenna and its application for measuring liquid real permittivities. *IET microwaves, antennas & propagation,* 8**,** 255-262.

Zhou, Y., Wu, Y., Asghar, W., Ding, J., Su, X., Li, S., Li, F., Yu, Z., Shang, J. & Liu, Y. 2019. Asymmetric structure based flexible strain sensor for simultaneous detection of various human joint motions. *ACS Applied Electronic Materials,* 1**,** 1866-1872.

Zhu, G.-J., Ren, P.-G., Guo, H., Jin, Y.-L., Yan, D.-X. & Li, Z.-M. 2019. Highly sensitive and stretchable polyurethane fiber strain sensors with embedded silver nanowires. *ACS applied materials & interfaces,* 11**,** 23649-23658.

Zhu, J., Zhang, S., Yi, N., Song, C., Qiu, D., Hu, Z., Li, B., Xing, C., Yang, H. & Wang, Q. 2021. Strain-insensitive hierarchically structured stretchable microstrip antennas for robust wireless communication. *Nano-Micro Letters,* 13**,** 1-12.

Zhu, S. 2008. *Wearable antennas for personal wireless.* Ph. D. dissertation, Dept. Electron. Elect. Eng., Univ. Sheffield, Sheffield, UK.

Zrnic, D. & Swatik, D. 1969. On the resistivity and surface tension of the eutectic alloy of gallium and indium. *Journal of the less common metals,* 18**,** 67-68.

PUBLICATIONS

a) Low, J.H., Chee, P.S. and Lim, E.H., 2019, July. Development of A Microfluidic Based Stretchable Sensor. In *2019 IEEE International Conference on Sensors and Nanotechnology* (pp. 1-4). IEEE.

b) Low, J.H., Chee, P.S. and Lim, E.H., 2019. Deformable liquid metal patch antenna for air pressure detection. *IEEE Sensors Journal*, *20*(8), pp.3963-3970.

c) Low, J.H., Chee, P.S., Lim, E.H. and Ganesan, V., 2020. Design of a wireless smart insole using stretchable microfluidic sensor for gait monitoring. *Smart Materials and Structures*, *29*(6), p.065003.

d) Low, J.H., Chee, P.S., Lim, E.H. and Lee, K.Y., 2020. Compact organic liquid dielectric resonator antenna for air pressure sensing using soft material. *Scientific reports*, *10*(1), pp.1-10.

e) Low, J.H., Chee, P.S., Lim, E.H. and Ganesan, V., 2021, January. Kirigami-Structured and Self-Powered Pressure Sensor Using Electroactive Polymer. In *2021 IEEE 34th International Conference on Micro Electro Mechanical Systems (MEMS)* (pp. 748-751). IEEE.

APPENDICES

APPENDIX A: Ethical Approval for Research Project

Page 1 of Ethical Approval Letter

UNIVERSITI TUNKU ABDUL RAHMAN
Wholly Owned by UTAR Education Foundation (Company No. 578227-M)

Re: U/SERC/216/2021

28 September 2021

Dr Chee Pei Song
Department of Mechatronics and BioMedical Engineering
Lee Kong Chian Faculty of Engineering and Science
Universiti Tunku Abdul Rahman
Jalan Sungai Long
Bandar Sungai Long
43000 Kajang, Selangor

Dear Dr Chee,

Ethical Approval For Research Project/Protocol

We refer to your application for ethical approval for your research project (PhD student's project) and are pleased to inform you that your application has been approved under Expedited Review.

The details of your research project are as follows:

Research Title	Development of Stretchable Sensors for wearable application
Investigator(s)	Dr Chee Pei Song Low Jen Hahn (UTAR Postgraduate Student)
Research Area	Science
Research Location	UTAR
No of Participants	1 participant
Research Costs	UTAR Research Fund (UTARRF)
Approval Validity	28 September 2021 - 27 September 2022

The conduct of this research is subject to the following:

(1) The participants' informed consent be obtained prior to the commencement of the research;

(2) Confidentiality of participants' personal data must be maintained; and

(3) Compliance with procedures set out in related policies of UTAR such as the UTAR Research Ethics and Code of Conduct, Code of Practice for Research Involving Humans and other related policies/guidelines.

(4) Written consent be obtained from the institution(s)/company(ies) in which the physical or/and online survey will be carried out, prior to the commencement of the research.

Kampar Campus : Jalan Universiti, Bandar Barat, 31900 Kampar, Perak Darul Ridzuan, Malaysia
Tel: (605) 468 8888 **Fax:** (605) 466 1313
Sungai Long Campus : Jalan Sungai Long, Bandar Sungai Long, Cheras, 43000 Kajang, Selangor Darul Ehsan, Malaysia
Tel: (603) 9086 0288 **Fax:** (603) 9019 8868
Website: www.utar.edu.my

Page 2 of Ethical Approval Letter

Should you collect personal data of participants in your study, please have the participants sign the attached Personal Data Protection Statement for your records.

The University wishes you all the best in your research.

Thank you.

Yours sincerely,

Professor Ts Dr Faidz bin Abd Rahman
Chairman
UTAR Scientific and Ethical Review Committee

c.c Dean, Lee Kong Chian Faculty of Engineering and Science
Director, Institute of Postgraduate Studies and Research

Kampar Campus : Jalan Universiti, Bandar Barat, 31900 Kampar, Perak Darul Ridzuan, Malaysia
Tel: (605) 468 8888 **Fax:** (605) 466 1313
Sungai Long Campus : Jalan Sungai Long, Bandar Sungai Long, Cheras, 43000 Kajang, Selangor Darul Ehsan, Malaysia
Tel: (603) 9086 0288 **Fax:** (603) 9019 8868
Website: www.utar.edu.my